

**OPTICAL COHERENCE TOMOGRAPHY DISTAL SENSOR BASED  
HANDHELD MICROSURGICAL TOOLS**

by

Gyeong Woo Cheon

A dissertation submitted to the Johns Hopkins University in conformity with the  
requirements for the degree of Doctor of Philosophy

Baltimore, Maryland

October 2016

© 2016 Gyeong Woo Cheon

All Rights Reserved

## **ABSTRACT**

Microsurgery is typically differentiated from a general surgery in that it requires a precise sub-millimeter manipulation that could only be achievable under optical magnification. For instance, microsurgeons use surgical microscopes to view surgical sites and train themselves several years to acquire surgical skills to perform the delicate procedures. However, such microsurgical approach imposes considerable physical stress and mental fatigue on the surgeons and these could be sources for surgical risks and complications.

For these reasons, a variety of robotic based surgical guidance methods have been developed and studied with the hope of providing safer and more precise microsurgery. These robotic arm based systems have been developed to provide precise tool movement and to remove physiological hand tremor, which is one of the main limiting factors that prevents precise tool manipulation. In another approaches use simpler system that adds robotic functions to existing handheld surgical tools. It is a hybrid system that incorporates the advantages of conventional manual system and robot-assist system. The advantages of such hybrid handheld systems include portability, disposability, and elimination of the large robotic-assist systems in complex surgical environment. The most critical benefit of the hybrid handheld system is its ease of use since it allows surgeons to manipulate tools mostly using their hand. However due to the imprecise nature of tool control using hands, tool tracking is more critical in handheld microsurgical tool systems than that of robotic arm systems. In general, the accuracy of the tool control is largely determined by the resolution of the sensors and the actuators. Therefore, it is

essential to develop a real-time high resolution sensor in order to develop a practical microsurgical tools.

For this reason, a novel intuitive targeting and tracking scheme that utilizes a common-path swept source optical coherence tomography (CP-SSOCT) distal sensor was developed integrated with handheld microsurgical tools. To achieve micron-order precision control, a reliable and accurate OCT distal sensing method was developed. The method uses a prediction algorithm is necessary to compensate for the system delay associated with the computational, mechanical and electronic latencies. Due to the multi-layered structure of retina, it was also necessary to develop effective surface detection methods rather than simple peak detection.

The OCT distal sensor was integrated into handheld motion-guided micro-forceps system for highly accurate depth controlled epiretinal membranectomy. A touch sensor and two motors were used in the forceps design to minimize the motion artifact induced by squeezing, and to independently control the depth guidance of the tool-tip and the grasping action. We also built a depth guided micro-injector system that enables micro-injection with precise injection depth control. For these applications, a smart motion monitoring and a guiding algorithm were developed to provide precise and intuitive freehand control.

Finally, phantom and *ex-vivo* bovine eye experiments were performed to evaluate the performance of the proposed OCT distal sensor and validate the effectiveness of the depth-guided micro-forceps and micro-injector over the freehand performance.

**Dissertation Committee:**

Prof. Dr. Jin U. Kang, ECE (Thesis Advisor, Dissertation Reader)

Prof. Dr. Amy C. Foster, ECE (Dissertation Reader)

Prof. Dr. Muyinatu Bell, ECE

Prof. Dr. Peter L. Gehlbach, Wilmer Eye Institute, ECE



## ACKNOWLEDGEMENTS

On the way to the completion of my dissertation at Johns Hopkins University, I have been received countless advices and support from a wonderful group of people. Without their help and encouragement, it would be totally impossible to finish my dissertation work. Now, I am very happy to have a chance to express my deepest gratitude to them.

Above all, I would like to gratefully and sincerely thank my thesis advisor, Dr. Jin U. Kang, for his not only academic but also social advice, guidance and leadership during my graduate studies. Under his mentorship, I was able to cultivate my abilities to be an independent researcher. For the past 4 years, I was surprised of his steady passion for the research and his passion always evoked me not to fall into mannerism but become more creative at every moment.

I would also like to thank my co-advisor, Dr. Peter L. Gehlbach, for his advice and help during our collaboration. Peter has given me a great opportunity and insight for interdisciplinary research. Through the discussion with him, I could have deeper understanding of the actual requirements for our developing microsurgical tools.

I would like to express my earnest appreciation to the members of my dissertation committee and graduate board oral (GBO) exam committee, Dr. Peter L. Gehlbach, Dr. Trac D. Tran, Dr. Iulian Iordachita, Dr. Sung Hoon Kang, Dr. Amy C. Foster, Dr. Jin Seob Kim and Dr. Muyinatu Bell for their constructive review of my dissertation research.

I also deeply appreciate the help and contribution from former and current group members of Dr. Kang's Photonics and Optoelectronics Lab, my colleagues and friends in

and outside Hopkins. Special thanks are to Dr. Chang-Seok Kim, Dr. Jae-Ho Han, Dr. Do-Hyun Kim, Dr. Kang Zhang, Dr. Xuan Liu, Dr. Daguang Xu, Dr. Yong Huang, Dr. Jaepyeong Cha, Hanh Le, Soohyun Lee, Dr. Mingtao Zhao, Dr. Cheol Song, Dr. Hyun Woo Jeong, Dr. Phillip Lee, Dr. Chang Ho Lee, Rebecca Pak, Dohee Kim, Saumya Gurbani, Berk Gonenc, Dr. Jemin Chae, Dr. Yi Yang, Dr. Sewon Kang, Sherry Leung, Dr. Chang Kyu Yoon, Dr. Hye Rin Kwag, Dr. Chloe Kim, Dr. Junghoon Lee, Dr. Min Yang Jung, Dr. Jeeun Kang, Dr. Sungmin Kim, Nathan Cho, and Younsu Kim.

Finally, I want to dedicate this work to the most valuable people in my life. My wife (Sojin) and daughter (Shua) have given me endless love. Without them, all these achievements are meaningless. I also thank my parents, my parents-in-law, my sister, my brother-in-law and his family for their never-ending encouragement and support.

## TABLE OF CONTENTS

ABSTRACT.....	ii
ACKNOWLEDGEMENTS.....	v
TABLE OF CONTENTS.....	vii
LIST OF FIGURES .....	ix
CHAPTER 1 : INTRODUCTION .....	1
1.1 Motivation.....	1
1.2 Research Objectives.....	3
1.3 Dissertation Overview .....	4
CHAPTER 2 : PRINCIPLES OF OPTICAL COHERENCE TOMOGRAPHY FOR DISTAL SENSOR.....	5
2.1 Optical Fibers.....	5
2.1.1 Numerical aperture and V parameter.....	6
2.1.2 Fiber types.....	7
2.1.3 Dispersion in Fiber.....	8
2.2 Principles of OCT .....	9
2.2.1 Michelson Interferometry .....	9
2.2.2 Time Domain OCT .....	12
2.2.3 Fourier Domain OCT .....	14
2.2.3.1 Spectral-Domain OCT (SD-OCT) and Swept-Source OCT (SS-OCT) ....	16
2.2.3.2 Balanced detector.....	18
2.3 Common-path OCT .....	21
2.3.1 Fabry–Pérot interferometer.....	21
2.3.1.1 CP-OCT with lossless medium.....	22
2.3.1.2 CP-OCT with lossy medium.....	27
2.3.2 Ball lens .....	32
2.3.3 Ghost image .....	34
2.3.3.1 Deconvolution method to remove the ghost image .....	35
2.3.3.2 Single-reflector sample .....	38
2.3.3.3 Complex-reflector sample.....	40
CHAPTER 3 : ACCURATE REAL-TIME DEPTH CONTROL FOR CP-SSOCT DISTAL SENSOR BASED HANDHELD MICROSURGERY TOOLS .....	43
3.1 Introduction.....	43
3.2 Background Theory .....	47
3.2.1 Spatially shifted cross-correlation.....	47
3.2.2 Kalman filter .....	48
3.3 Materials and Methods.....	51
3.3.1 System configuration .....	52
3.3.2 The control algorithm .....	54
3.3.3 Data flow in CPU and GPU .....	59
3.4 Experimental results and discussion .....	60
3.4.1 Phantom experiment .....	60
3.4.2 Bovine retina experiment.....	62
3.5 Conclusion .....	65

CHAPTER 4 : HANDHELD MOTION-GUIDED MICRO-FORCEPS FOR EPIRETINAL MEMBRANECTOMY BASED ON CP-SSOCT .....	66
4.1 Introduction.....	66
4.2 Materials and Methods.....	70
4.2.1 Fiber-Optic OCT Module .....	70
4.2.2 Micro-Forceps Module .....	71
4.2.3 PCB design.....	73
4.2.4 System Software Module.....	77
4.3 Experiments .....	79
4.4 Results and Discussion .....	80
4.4.1 Evaluation of Motion Artifact during Grasping.....	80
4.4.2 Grasp and Pick up Experiments.....	83
4.5 Conclusion .....	86
CHAPTER 5 : SMART MICRO-INJECTOR BASED ON HANDHELD CP-SSOCT GUIDED MICROSURGICAL TOOL .....	87
5.1 Introduction.....	87
5.2 Materials and Methods.....	90
5.2.1 Limitation of Freehand manipulation .....	90
5.2.2 Micro-injector system configuration.....	90
5.2.3 Gelatin phantom injection test .....	94
5.2.4 Mechanics of dynamic needle insertion.....	97
5.2.5 Modified Needle guidance method.....	102
5.3 Results and Discussion .....	103
5.3.1 Dynamic insertion test .....	103
5.3.2 Multiple injection, Gelatin test .....	104
5.3.3 Ex-vivo bovine eye injection test.....	105
5.4 Conclusion .....	107
CHAPTER 6 : Random transverse motion-induced spatial compounding for fiber bundle imaging .....	109
6.1 Introduction.....	109
6.2 Materials and Methods.....	111
6.2.1 System configuration .....	111
6.2.2 Basic concept of the compounding method .....	112
6.2.3 Compounding process.....	113
6.3 Results and Discussion .....	118
6.3.1 USAF target test.....	118
6.3.2 Biological sample imaging (Pyramidal cell).....	124
6.4 Conclusion .....	125
CHAPTER 7 : CONCLUSIONS .....	126
7.1 Summary of Contributions.....	126
7.2 Future Work .....	128
BIBLIOGRAPHY.....	129
CURRICULUM VITAE.....	143

## LIST OF FIGURES

Figure 2.1. Inner structure of optical fiber.....	5
Figure 2.2. Rays within the acceptance cone specified by acceptance angle, $\theta_a$ , are guided total internal reflection in fiber. ....	6
Figure 2.3. Fiber types having step-index configuration and modal distortion: a) single- mode fiber and b) multi-mode fiber.....	7
Figure 2.4. Fiber-optic based Michelson Interferometer .....	9
Figure 2.5. Illustration of the three discrete reflectors having delta function of field reflectivity in sample (top) and the A-scan acquired by TD-OCT. ....	13
Figure 2.6. Illustration of the three discrete reflectors having delta function of field reflectivity in sample (top) and the A-scan acquired by FD-OCT.....	15
Figure 2.7. Schematics of (a) SD-OCT and (b) SS-OCT configurations. ....	16
Figure 2.8. Schematic of balanced detection circuit consists of voltage follower to transform the input current to output voltage and differential amplifier to reject the common-mode of the inputs: reference and sample currents.....	18
Figure 2.9. Norton equivalent circuit to analyze the voltage follower circuit, which transform the sampled photo-electric current generated by the interference signal into measurable voltage signal. ....	19

Figure 2.10. Schematic of common-path OCT (CP-OCT) setup (top) and magnified image of the probe-tip (bottom). .....	21
Figure 2.11. Ray-tracing of the Fabry–Pérot interferometer with lossless medium between the mirrors. ....	22
Figure 2.12. Light source intensity graph having Gaussian shape in a) wavelength domain and b) wavenumber domain. ....	25
Figure 2.13. Fabry–Pérot interferometer simulation results including system transfer function, interferogram, and A-scan with lossless medium. Left side is the result of $d = 50$ micrometer and right side is of $d = 100$ micrometer. ....	26
Figure 2.14. Ray-tracing of the Fabry–Pérot interferometer with lossy medium between the mirrors. ....	27
Figure 2.15. Fabry–Pérot interferometer simulation results including system transfer function, interferogram, and A-scan with lossy medium. Attenuation coefficient is $\alpha$ . Left side is the result of $d = 50$ micrometer and right side is of $d = 200$ micrometer. ....	29
Figure 2.16. Fabry–Pérot interferometer simulation results including system transfer function, interferogram, and A-scan with lossy medium. Attenuation coefficient is $25\alpha$ . Left side is the result of $d = 50$ micrometer and right side is of $d = 200$ micrometer. ....	30
Figure 2.17. Fabry–Pérot interferometer simulation results including system transfer function, interferogram, and A-scan with lossy medium. Attenuation	

coefficient is $50\alpha$ . Left side is the result of $d = 50$ micrometer and right side is of $d = 200$ micrometer.....	31
Figure 2.18. Ray-tracing in ball lens and SMF.....	32
Figure 2.19. Schematic of the system; (a) fiber probe with sapphire ball lens having 500um diameter, (b) system overview, and (c) photo image of the probe. ...	34
Figure 2.20. Simulation result; (a) ground truth signal synthesized with the combination of ten reflectors, (b) simulated raw A-scan with random noise, (c) background (fixed) noise subtracted A-scan signal, and (d) the reconstructed signal graph. ....	35
Figure 2.21. Mirror experiment result; (a) raw A-scan graph and (b) background subtracted A-scan graph (blue) and distortion corrected A-scan graph (red).	39
Figure 2.22. Cellophane tape experiment result; (a) raw A-scan graph and (b) background subtracted A-scan graph (blue) and ghost corrected A-scan graph (red).....	41
Figure 2.23. Cellophane tape B-scan images; (a) raw, (b) background subtracted, and (c) ghost corrected B-scan images.....	42
Figure 3.1. Three consecutive A-scan data of 20-stacked layers of adherent cellophane tape near the DC line (multi-layered phantom sample); the upper right inserted graph is a partial magnified graph of area in dotted red square in lower entire graph. ....	46
Figure 3.2. The basic concept of Sensorized Micromanipulation Aided Robotic-surgery Tool (SMART) system based on closed loop feedback system .....	51

Figure 3.3. a) Active depth targeting and locking microsurgery system, b) CAD cross-sectional image of handheld tool (NTC: needle-to-tube connector, PM: piezo-motor, OF: optical fiber) .....	52
Figure 3.4. System connection for the synchronization among the core components: OCT engine, workstation, and motor driver. ....	53
Figure 3.5. a) A-scan data of <i>ex-vivo</i> open bovine retina, b) three consecutive A-scan data of stacked layers of adherent cellophane tape, c) data processing flowchart consisting of 1) OCT data process, 2) Surface detection, and 3) Motor control. ....	55
Figure 3.6. Example A-scans to show the difference between the samples having a) simple one dominant reflector and b) complex multiple reflectors typically shown in bio-sample. ....	57
Figure 3.7. Data flow between CPU and GPU. ....	59
Figure 3.8. Dry phantom experiment: a) evaluation test for the surface detection algorithm with the auxiliary shifted cross-correlation in non-depth-locking freehand, b) evaluation test for the depth-locking with the predictor based on Kalman filter: the upper inserted graph is a magnified graph of area in dotted yellow trapezoid in the entire graph.....	61
Figure 3.9. Bovine retina experiment: a) bovine retina after removing cornea, lens, and vitreous humor, b) snapshot of the experiment, c) depth targeting and locking experiment result with six different jumping distance from 10 $\mu\text{m}$ to 60 $\mu\text{m}$	63



Figure 3.10. Averages of RMSE with standard deviation error bar of the bovine retina experiment. The x-axis labels mean jumping distance and the y-axis indicates the means and standard deviations of the measurement specified in Table 1.	64
Figure 4.1. (a) Epiretinal membranectomy: after grasping the membrane edge with a micro-forceps the membrane is pulled away from the retina surface slowly; (b) The standard 23 Gauge disposable micro-forceps (Alcon, USA); Our motorized active motion-guided micro-forceps: (b) fabricated prototype, (c) inner structure with two motors (M1 and M2) and the fiber-optic sensor (SSOCT) attached to the straightened arm of the jaws.	69
Figure 4.2. (a) CP-SSOCT fiber-optic setup: the reflected beam (RB), fiber-air interface (FAI), and the sample reflected beam (SB). Overview of our CP-SSOCT depth-guided micro-forceps system: (b) earlier "SMART: microforceps prototype using one actuator for depth guidance and the squeeze mechanism for grasping [21], (c) current design using a touch sensor and two independently actuated motors for the control of grasping (green) and depth guidance (red) actions.	70
Figure 4.3. Calibration curve for the touch sensor. The curve is divided into three zones: (1) dead zone where the tool-tip manipulating motor does not react to the touch sensor, (2) active zone that is responsible for motor control, and (3) saturation zone where the motor has reached its maximum position.	71
Figure 4.4. Schematic of the circuit design for MCU (STM32F405) part.	74

Figure 4.5. Schematic of the circuit design for a) USB communication, b) Squiggle motor connection (SPI), c) amplifying the output of touch sensor and sampling (ADC), d) power supply for MCU, and e) power supply for motor. ....	75
Figure 4.6. Layout of the designed control board circuit.....	76
Figure 4.7. Image of the Implemented control board based on the circuit design. All the components are mounted on the PCB. The upper image shows the top layer of the board and the lower image shows the bottom layer of the board. ....	76
Figure 4.8. Data processing flowchart consisting of 1) OCT signal processing, 2) Surface detection signal processing, and 3) Motion control processing. Each step is implemented in independent software module; especially, the OCT signal processing module uses parallel processing technique based on GPU programming.....	78
Figure 4.9. Measured distance variation as the surgeon opens and closes the forceps while trying to maintain the tool tip fixed above a thin film layer (a) using a conventional 23 gauge micro-forceps, using our micro-forceps (actuated via the touch sensor) (b) without and (c) with the motion guidance feature. 10 grasps were performed for each case. Vertical bars show the opening and closure of the forceps jaws. The motion artifact was significantly reduced by the using the touch sensor based actuation on our tool rather than the squeezing mechanism on the conventional micro-forceps. ....	81

Figure 4.10. Frequency analysis of the distance variation during the grasping actions: (a) using standard manual micro-forceps, using our motorized micro-forceps (b) without and (c) with the motion guidance feature. ....	82
Figure 4.11. (a) Grasp and pick-up experiments: small fiber pieces ( $\varnothing$ 125 $\mu$ m) were picked up from a soft polymer surface using MGMF. (b) A 2D scanning OCT imaging system was used to analyze the damage created on the polymer surface after each grasp. (c) A snapshot of the developed software displaying real-time A-scan data, video view of the operation site, and the touch sensor output (red bar graph). ....	84
Figure 4.12. Results of the grasp and pick-up experiment: Statistically significant reduction in (a) elapsed time, (b) number of grasping attempts, and (c) the maximum depth of damage on the substrate with the use of our OCT-based motion guidance feature. The solid bars show the mean, and the error bars represent the maximum and minimum values. ....	85
Figure 4.13. The maximum depth of damage vs. elapsed time during the grasp and pick-up experiments. The trials without the motion guidance have a significantly wider distribution than the guided trials, which have are grouped around much smaller damage and elapsed time levels. ....	85
Figure 5.1. Free hand insertion test performed by retinal surgeon under the microscope: a) needle-tip position tracking data during the insertion trials, b) a partial magnified graph of area in red ellipse in the above graph. The two red dotted	

lines show the boundary of variation while the surgeon maintained the needle-tip position.....	89
Figure 5.2. (a) System overview of the CP-SSOCT depth-guided micro-injector and (b) internal structure of the micro-injector and CP-SSOCT fiber-optic sensor: RB (Reflected beam), FAI (Fiber-Air Interface), SB (Sample reflected beam) ..	91
Figure 5.3. a) Diverse types of needle-tip (Hamilton®), b) custom-built pump module consisting needle, needle and tube coupler, flexible tube, micro-syringe, and linear servo-motor. ....	93
Figure 5.4. Flow chart of OCT data processing for distal sensing and motion control. The processing consists of three main parts: 1) OCT data transformation from measured spectral data, 2) distal information extraction from the OCT data, and 3) motion control based on the distal information. ....	95
Figure 5.5. Preliminary 10% gelatin phantom injection test: a) distance tracking data which has blind area caused by surface deformation, b) five consecutive injection trials on a gelatin sample. The preset penetration depth was 1.34 mm. ....	96
Figure 5.6. Needle-tip position tracking graph to demonstrate how the system intervenes and guide the needle-tip: a) the tracking data without pre-poking stage and there is blind area due to surface deformation of the sample, b) the tracking data with pre-poking stage and the system achieves maximum speed during this stage to reduce the surface deformation. ....	98
Figure 5.7. A Kelvin model for the needle inserting into a soft tissue. ....	99

Figure 5.8. a) Dynamic insertion test under the condition that has interaction between needle-tip and sample material. The upper inserted graph is a partial magnified graph of area in red square in lower entire graph, b) the average deviation error of 100 injections with error bar consisting a positive and negative RMSE. ....	104
Figure 5.9. The ex-vivo bovine eye injection experiment: a) and c) are snap shots displaying the multiple fluorescein injections. Fluorescein was excited by blue light for fluorescence emission, b) tracking data of the needle-tip. Each graph has RMSE below it during the depth-locking.....	106
Figure 6.1. a) Fiber bundle inner structure. ....	110
Figure 6.2. Fiber bundle fluorescence imaging system: (a) system schematic (CL: Condenser lens, EF: Emission filter, DM: Dichroic mirror, OL: Objective lens, FB: Fiber bundle, mOL: miniature-objective lens) and (b) compounding process: transverse-motion-induced images are arranged and compounded to eliminate blank region (pixelation artifact).....	112
Figure 6.3. Process for extracting available pixels: (a) background image after thresholding, (b) original fiber bundle image, (c) available pixels extracted by applying (a) to (b), and (d)–(f) magnified images of the square area in (a)–(c). Scale bar represents 50 $\mu$ m. ....	115
Figure 6.4. Obtained USAF target images: (a) original image, (b)–(f) compounded images using different numbers of sample images. ....	117

Figure 6.5. Resolution test: (a) group 7, original image, (b) group 7, compounded image ( $N=20$ ), and (c) intensity variation graphs of pixels along the arrows.....	120
Figure 6.6. Relative CNR improvement graph by increasing the number of compounding. The first image only consisting of effective pixels (not compounded) was used for reference image to calculate the relative CNR. ....	121
Figure 6.7. Microscope images of pyramidal cell. Scale bar represent 50 $\mu\text{m}$ . ....	122
Figure 6.8. Pyramidal cell imaging results: (a) original fiber bundle image, (b) Gaussian-filtered image, (c) compounded image using 20 sample images, (d)–(f) magnified image of area in dotted white circle in (a)–(c). Scale bar represents 50 $\mu\text{m}$ . ....	123

## CHAPTER 1 : INTRODUCTION

### 1.1 Motivation

Microsurgery is a surgery that requires a surgical microscope to perform delicate surgical procedure at the limits of human dexterity. Naturally, accurate and precise tool tip manipulation is imperative for successful surgical outcomes. There are diverse medical areas that require microsurgical techniques and is the focus of this work is in ophthalmology. Human eye is a sensory organ that processes the largest amount of information in human life. In particular, retina, which is the main part that receives and processes the visual information, has a very sophisticated thin layered structure. As a result, retinal surgery requires extremely high level of surgical skill sets. Retinal microsurgery is performed by passing microsurgical tools through trocars that provide access through the eye wall (sclera). The trocar not only provides safe access into the eye but it also guides and stabilizes the surgical tools and acts as a remote center of motion (RCM). As a result, the lateral motion of the surgical tool is relatively well stabilized. However, in the case of axial motion, it is the surgeon that currently provides all of the guidance and control. It is known that one of the main barriers in microsurgery is physiological hand tremor that occurs predominating in the 6-12 Hz frequency domain with the amplitude in the order of several hundred-micron-order amplitude[1], [2]. To overcome these human factors, surgeons requires several years of training to acquire stable and dexterous manipulation skills. Additionally, considerate should be noted that the freehand tool movements are guided predominantly by visual information acquired through the use of a surgical microscope. Tool tip visualization through the use of surgical microscope is limited particularly in the axial direction since it does not provide

the ability to resolve small changes in position as well as by the obstruction of the retinal surface by the tool shaft and tip.

A variety of robot-assisted systems have been developed to overcome such limitations and to minimize surgical risks[3]–[9]. Early in the evolution of this technology, our aim was to develop a robot-assisted system with high accuracy and user-friendly operating manipulation[3]–[7]. Recently, diverse active tool-tips and sensors have been developed and integrated into the system to enhance its functionality[8], [9]. In parallel, Riviere, *et al.* has been developing a handheld microsurgical system that has differentiated itself from traditional robotic arm based systems[10]–[16]. The handheld system operates independently without the assistance of external equipment such as a robotic arm by using its own embedded sensors and actuators. The advantages and disadvantages of the two assistance systems are numerous and are still being elucidated. However, advantages of the handheld systems include but are not limited to: lower cost, potential disposability, greater portability, ease of packaging, lower production costs, ease of use, adaptability, and ease of customization that can be easily integrated into standard clinical settings. A fundamental challenge to any handheld microsurgical tool is of the hand tremor compensation. A variety of motion sensors including accelerometer, magnetometer, position-sensitive detectors with infrared LED, etc. and small size of actuators such as piezo-electric motors and voice coils have been introduced. Moreover, a frequency analysis based tremor model has been previously built in accordance with the roughly sinusoidal nature of tremor[10].

Optical coherence tomography (OCT) has recently emerged as an effective imaging modality to support microsurgery due to its micron-order resolution and



subsurface imaging capability[17]–[23]. Microscope mounted OCT systems now play significant roles in intraoperative visualization for forward viewing during actual surgical procedures. Unlike the above conventional imaging approaches, OCT can also play a role as a high resolution distal sensor and a real-time intraoperative guidance system that provides axial motion sensing of handheld tools[24]–[35]. The motion compensation achieved using the feedback from the OCT distal sensor can effectively suppresses undesired axial motion; as a result, the frequency region related to hand tremor can be significantly decreased[34]. Common-path OCT (CP-OCT) is strategically chosen to incorporate with handheld microsurgery tools due to its comparatively simple in design, relatively affordable price and the potential to be used as disposable surgical products. This research presents the development of OCT distal sensor and its integration to conventional microsurgical tools, and assess its performance to show whether this technology can improve the performance of microsurgery.

## **1.2 Research Objectives**

In this research, my contribution has been to design, develop and implement a real-time micron resolution OCT distal sensor incorporated with a piezo-electric linear actuator for compensating physiological hand tremor and to provide accurate depth guidance for vitreoretinal surgery. The system performance was optimized through implementing real-time feedback system, developing accurate retina detection, distal sensing and motion control algorithms. Applying these techniques into conventional surgical tools and finally validating them through phantom and *ex vivo* animal studies. The above-mentioned objectives are specified in the following aims:

1. Develop a real-time common-path swept source OCT system integrated with a piezo-electric linear actuator for closed loop feedback system in order to compensate physiological hand tremor and supply accurate depth guidance.
2. Develop a reliable and robust distal sensing algorithm from the time limited OCT data and a motion predictor for better motion control by compensating the time delay due to the computation time.
3. Evaluate the effectiveness of the distal sensing and motion guidance system by applying this technique into practical ocular surgical tools and performing phantom and ex-vivo bovine experiments.

### **1.3 Dissertation Overview**

This dissertation presents the development of real-time OCT distal sensor and intraoperative motion guidance technologies and their applications in micro-ocular surgeries. Chapter 2 reviews the fundamental principles of Optical Coherence Tomography. Chapter 3 presents a system design and main algorithms for OCT distal sensing and motion guidance. Chapter 4 describes how to apply the technique to micro-forceps that is one of the most frequently used micro-surgical tools and evaluate the effectiveness of the depth-guided micro-forceps system. Chapter 5 presents a depth-guided micro-injector incorporating with our distal sensor for micron-order precision injection. Chapter 6 illustrates a spatial compounding study using a fiber bundle imaging platform for the extension of fiber-optic sensor. Chapter 7 summarizes the dissertation and proposes future directions of research.

## CHAPTER 2 : PRINCIPLES OF OPTICAL COHERENCE TOMOGRAPHY FOR DISTAL SENSOR

### 2.1 Optical Fibers

An optical fiber is a flexible circular dielectric waveguide made by glass or plastic and used to transmit light with extremely low loss. Optical fibers typically consist of a high-index core surrounded by a concentric cladding material with lower index of refraction. This configuration is designed to achieve total internal reflection which is responsible for the long transmission with a low loss. The core and cladding are surrounded with a protective polymer coating that protects them from external stress and forces. Additional protective covering is provided by a “jacket” as shown in Figure 2.1.

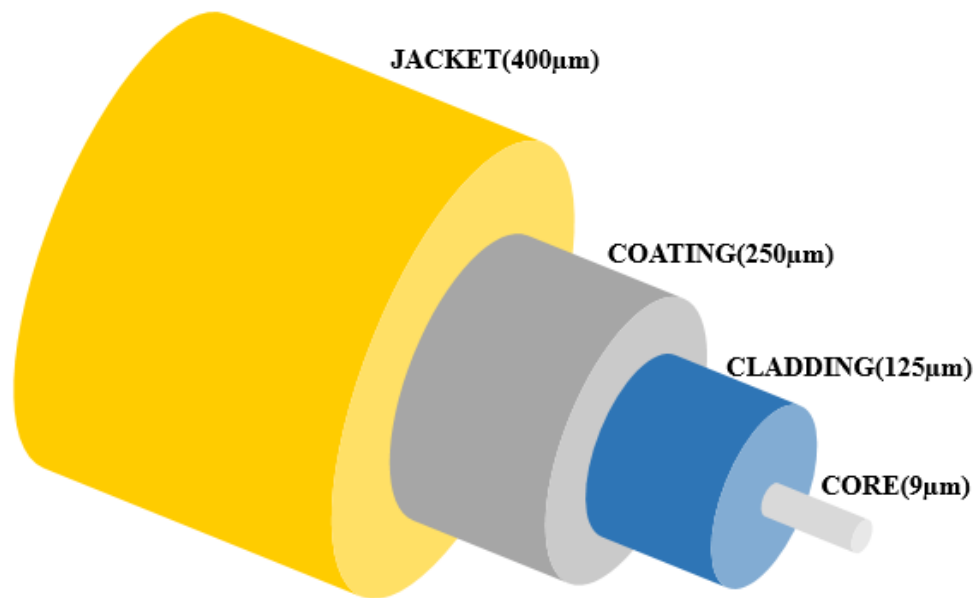


**Figure 2.1. Inner structure of optical fiber**

### 2.1.1 Numerical aperture and V parameter

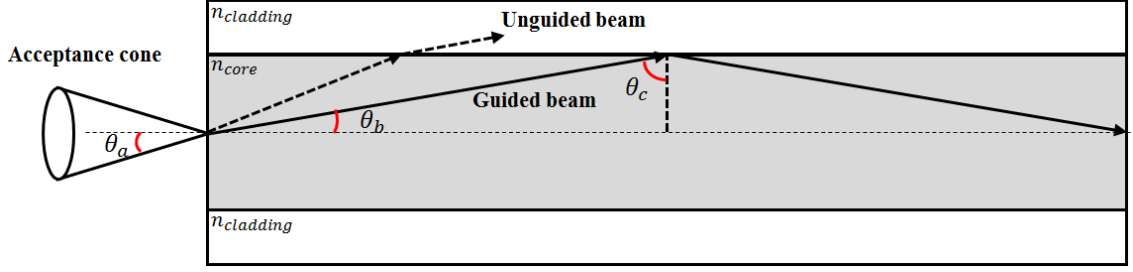


**Figure 2.2.** Rays within the acceptance cone specified by acceptance angle,  $\theta_a$ , are guided total internal reflection in fiber.

A ray incident from air into the fiber can be guided if the ray locates within the acceptance cone as shown in Figure 2.2. Acceptance angle,  $\theta_a$ , determines the shape of the acceptance cone and numerical aperture, NA, which describes the range of angles over which the fiber can accept or emit light. Applying Snell's law at the air-core interface, the angle  $\theta_a$  in air corresponding to  $\theta_b$  in the core is given by the relation,

$$NA := n_{air} \sin \theta_a = n_{core} \sin \theta_b \quad (1)$$

where  $n_{air}$  and  $n_{core}$  are refractive indices of air and fiber core, respectively. From the geometry of the Figure 2.2 we have:

$$\theta_b + \theta_c = \frac{\pi}{2} \rightarrow \sin \theta_b = \sin \left( \frac{\pi}{2} - \theta_c \right) = \cos \theta_c \quad (2)$$

where  $\theta_c$  is the critical angle for total internal reflection. We also have the following equation to satisfy the total internal reflection:

$$n_{core} \sin \theta_c = n_{cladding} \sin \frac{\pi}{2} \rightarrow \sin \theta_c = \frac{n_{cladding}}{n_{core}} \quad (3)$$

where  $n_{cladding}$  is the reflective index of the cladding. Solving the above three equations, then, we can get this formula to describe the numerical aperture, NA.

$$NA = \sqrt{n_{core}^2 - n_{cladding}^2} \quad (4)$$

In fact, the relationship between the NA and the acceptance angle of the fiber is not absolute because the acceptance angle for SMF cannot be solely determined by the refractive indices alone. There is another parameter to describe the number of bound modes and the mode volume, normalized frequency or V parameter:

$$V = \frac{2\pi a}{\lambda} NA \quad (5)$$

where  $a$  is the core radius and  $\lambda$  is the wavelength in vacuum of the ray. It is dimensionless parameter, which is very useful to define the relationship between applying wavelength and core radius and numerical aperture  $NA$ .

### 2.1.2 Fiber types

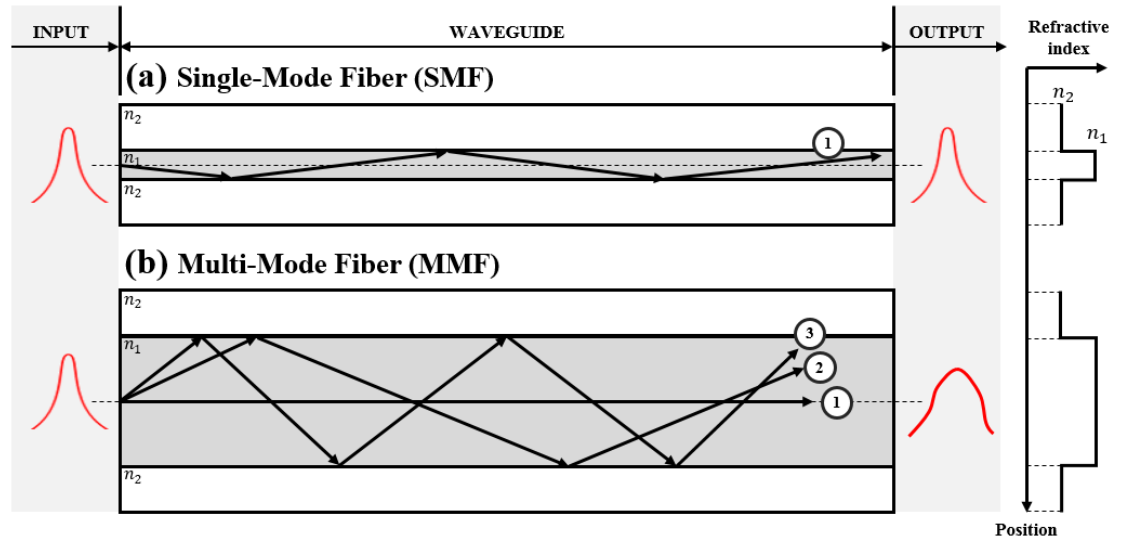


**Figure 2.3. Fiber types having step-index configuration and modal distortion: a) single-mode fiber and b) multi-mode fiber.**

Generally, optical fibers can be classified into two types: single-mode fibers (SMF) and multi-mode fibers (MMF) as shown in Figure 2.3. The core size of SMF is typically less

than 10 micrometers and it allows only the fundamental or lowest order mode with one group velocity to propagate in the fiber, i.e., no modal dispersion, so that a short pulse of light can pass the SMF with a minimal distortion mainly caused by the second-order chromatic dispersion. To satisfy the requirement for the single mode fiber, V-parameter should be less than or equal to 2.405. When V parameter is smaller than 2.05, only fundamental mode is guided while the other higher modes become leaky waves. Other dispersion effects that cause pulse spreading in SMF are typically considerably smaller than modal dispersion. On the other hand, MMF has large core diameters, which is typically larger than 50 micrometers and allows multiple modes to propagate. Thus, MMF is appropriate for delivering high energy than SMF. However, one of the difficulties related to light propagation in MMF is caused by the differences among the group velocities of the modes. This causes a rapid dispersion of the light pulse as it propagates through the fiber, and this effect is called modal dispersion[36].

### 2.1.3 Dispersion in Fiber

As mentioned in previous section, the largest contributor of the dispersion is modal dispersion and this dispersion can be minimized by using SMFs. However, there are still other factors that contribute to dispersion: material dispersion, waveguide dispersion, and nonlinear dispersion. All these dispersion factors can be expressed in terms of Group Velocity Dispersion (GVD). GVD indicates how different frequency components of the light propagate. As a result, a short pulse in the medium will broaden if the medium has a non-zero GVD. If  $\tau$  is the propagation delay at a particular value of  $\omega$ :

$$\tau = \frac{L}{v_g}, \quad \frac{\partial \tau}{\partial \omega} = L \frac{\partial}{\partial \omega} \left( \frac{1}{v_g} \right) = L \ddot{\beta} \quad (6)$$

where  $L$  is the length of the fiber and  $v_g$  is the group velocity. If a signal has a frequency range of  $\Delta\omega$ , the time range in propagation will be

$$\Delta\tau = \left| \frac{\partial\tau}{\partial\omega} \right| \Delta\omega = |\ddot{\beta}| \cdot L \cdot \Delta\omega \quad (7)$$

As a result, the pulse spread is proportional to  $\beta''$ ,  $L$  and the frequency bandwidth  $\Delta\omega$ .

The pulse spread is typically specified in terms of the pulse bandwidth,  $\Delta\lambda$ , in wavelength and the GVD coefficient,  $D$ :

$$\Delta\tau = |D| \cdot L \cdot \Delta\lambda \quad (8)$$

$$D = \frac{1}{L} \frac{\partial\tau}{\partial\lambda} = \frac{1}{L} \frac{\partial\tau}{\partial\omega} \frac{\partial\omega}{\partial\lambda} = -\frac{2\pi c}{\lambda^2} \ddot{\beta} \quad (9)$$

## 2.2 Principles of OCT

### 2.2.1 Michelson Interferometry

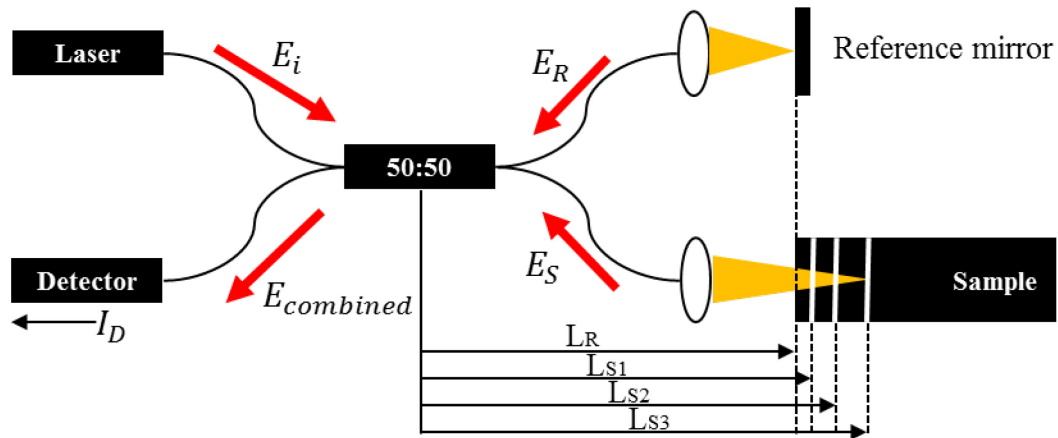


**Figure 2.4. Fiber-optic based Michelson Interferometer**

The Michelson interferometer is one of the most commonly used configuration optical interferometer configurations and Figure 2.4 shows a fiber-optic based Michelson interferometer. A coherent light source is split into two arms of a fiber-coupler (instead of

beam splitter): 1) reference arm and 2) sample arm. Subsequently, the split beams propagate to the end of the arms and reflected back from the reference and the sample. Then, the reflected beams combine again at the fiber-coupler and create interference patterns corresponding to the optical path length (OPL) differences. Mostly, Optical Coherence Tomography (OCT) is based on such Michelson interferometer configuration.

Now, let's derive several equations to describe the components in the interferometry. The polychromatic plain wave from a low coherent light source has an electric field expressed in a complex form,

$$E_i = s(k, \omega) e^{kL - \omega t} \quad (10)$$

where  $s(k, \omega)$  is the electric field amplitude as a function of wave-number and angular frequency, which are respectively the spatial and temporal frequencies of each spectral component. Then, the electric fields of the reflected beams from reference and sample arms:

$$E_R = \frac{E_i}{\sqrt{2}} r_R e^{j2kL_R} \quad (11)$$

$$E_S = \sum_i \frac{E_i}{\sqrt{2}} \left[ r_{S_i} * e^{j2kL_{S_i}} \right] \quad (12)$$

where  $r_R$  and  $r_{S_i}$  are reflectivities of reference mirror and each reflecting layer of a sample. Here, we assume that the sample consists of a series of multiple discrete layers having real delta function reflections. In sample electric field, (\*) means convolution and the factor of 2 in the exponential kernel describes the round-trip path length. The final output of the interferometer is detected by a photo-detector, which measure a photocurrent generated proportionally to the square of the sum of the field incident, given by



$$I_D(k, \omega) = \frac{\rho}{2} \langle |E_R + E_S|^2 \rangle = \frac{\rho}{2} \langle (E_R + E_S)(E_R + E_S)^* \rangle \quad (13)$$

where  $\rho$  is the responsivity of the photo-detector (Amperes/Watt), the factor of 2 describes the second pass of each field through the fiber-coupler, and the angular brackets denote integration over the response time of the detector. If we plug in the reflected electric fields into the above equation and expand it,

$$I_D(k, \omega) = \frac{\rho}{2} \left\langle \left| \frac{s(k, \omega)}{\sqrt{2}} r_R e^{j(2kL_R - \omega t)} + \frac{s(k, \omega)}{\sqrt{2}} \sum_i r_{S_i} e^{j(2kL_{S_i} - \omega t)} \right|^2 \right\rangle \quad (14)$$

Then, we can eliminate the temporal terms because  $\omega$  oscillates much faster than the response time of the detector. Then, we can finally get the following equation.

$$\begin{aligned} I_D(k) = & \frac{\rho}{4} [S(k)(R_R + R_{S_1} + R_{S_2} + \dots)] \text{ “DC term”} \\ & + \frac{\rho}{2} \left[ S(k) \sum_i \sqrt{R_R R_{S_i}} \cos[2k(L_R - L_{S_i})] \right] \text{ “Cross-correlation term”} \\ & + \frac{\rho}{2} \left[ S(k) \sum_{i \neq j} \sqrt{R_{S_i} R_{S_j}} \cos[2k(L_{S_i} - L_{S_j})] \right] \text{ “Auto-correlation term”} \end{aligned} \quad (15)$$

where  $S(k) = \langle |s(k, \omega)|^2 \rangle$  that encodes the power spectral dependent of the light source. The above equation has three distinct components. First, “DC terms” is the total summation of the power reflectivity or the reference mirror and sample layers. This is the largest component of the detector current. Next, “Cross-correlation terms” is the desired component for OCT imaging. This term is proportional to the square root of the product of mirror and sample reflections. Considering that the reflection of sample is typically smaller than the reflection of mirror, this term has smaller value than DC term. Finally, “Auto-correlation term” is the interference between the layers in sample. It typically has small intensity and locates near DC in frequency domain.

A light source having a Gaussian-shaped spectrum is convenient to numerically analyze OCT performances since many of actual light sources have quasi-Gaussian shape and the Fourier transform of a Gaussian function is also Gaussian function.

$$g(x) = \frac{1}{\sigma\sqrt{2\pi}} e^{-\frac{x^2}{2\sigma^2}} \xleftrightarrow{F} G(\omega) = e^{-\frac{\omega^2\sigma^2}{2}} \quad (16)$$

where  $g(x)$  is normalized. At the same time, the inverse Fourier transform of the source spectrum, also called “coherence function”, is used to determine the axial point-spread function (PSF) in the OCT imaging system. The PSF is typically decided by its full width at half the maximum (FWHM) value. Additionally, this value is the round-trip coherence length of the light source,  $l_c$ :

$$l_c = \frac{2\sqrt{\ln(2)}}{\Delta k} = \frac{2\ln(2)}{\pi} \frac{\lambda_0^2}{\Delta\lambda} \quad (17)$$

### 2.2.2 Time Domain OCT

In time-domain OCT (TD-OCT), the output current,  $I_D(k)$  in previous section is measure on the detector while the reference delay  $L_R$  is scanned to reconstruct the internal sample reflectivity profile  $\sqrt{R_S(L_S)}$ . If we ignore the auto-correlation term and assume the light source has Gaussian shape in wave-number,  $I_D(k)$  can be rewritten as,

$$I_D(k) = \frac{\rho}{4} [S(k)(R_R + R_{S1} + R_{S2} + \dots)] + \frac{\rho}{2} \left[ S(k) \sum_i \sqrt{R_R R_{S_i}} \cos[2k(L_R - L_{S_i})] \right] \quad (18)$$

$$S(k) = \frac{1}{\Delta k \sqrt{\pi}} e^{-\left(\frac{k-k_0}{\Delta k}\right)^2} \quad (19)$$

where  $k_0$  and  $\Delta k$  are the FWHM and the central wavenumber of the light source, respectively. If we plug  $S(k)$  in the  $I_D(k)$  and integrate over all  $k$ ,

$$I_D(L_R) = \frac{\rho}{4} \left[ S_0 [R_R + R_{S_1} + R_{S_2} + \dots] \right] \text{ “DC Component”} \quad (20)$$

$$+ \frac{\rho}{2} \left[ S_0 \sum_i \sqrt{R_R R_{S_i}} e^{-\Delta L_i^2 \Delta k^2} \cos[2k_0 \Delta L_i] \right] \text{ “Fringe Bursts”}$$

where  $S_0$  is the spectrally integrated power emitted by the light source and  $\Delta L_i$  is the OPL difference between reference and sample.

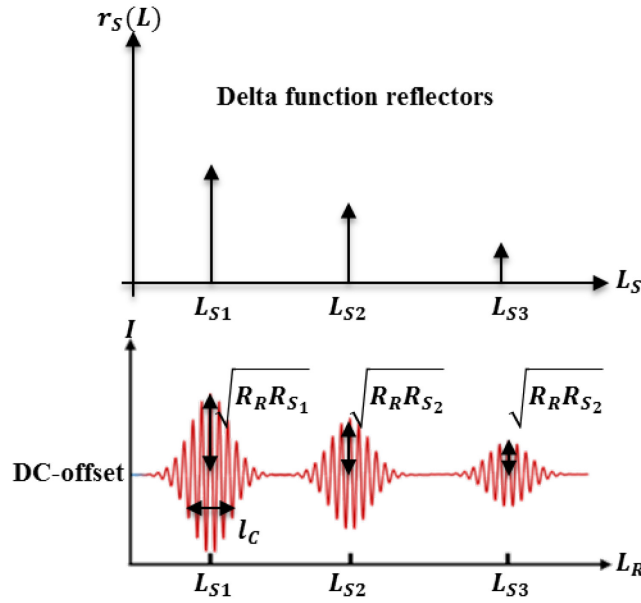


**Figure 2.5. Illustration of the three discrete reflectors having delta function of field reflectivity in sample (top) and the A-scan acquired by TD-OCT.**

As shown in Figure. 2.5, the A-scan or sample reflectivity profile convolved with the source coherence (Gaussian) function has a DC offset proportional to the sum of the reference and sample power reflectivity. In particular, the A-scan signal is modulated by a sinusoidal carrier wave at a frequency proportional to the source center wavenumber  $k_0$  and the OPL difference between reference and sample arm,  $\Delta L_i$ . The carrier wave supplies supportive frequency information for envelope detection and DC removal because the reference arm length  $L_R$  is typically a function of time in TD-OCT.

### 2.2.3 Fourier Domain OCT

In Fourier domain OCT (FD-OCT), the output current  $I_D(K)$  sampled and processed using Fourier analysis to reconstruct the sample reflectivity profile  $\sqrt{R_s(L_s)}$ . The process for sampling  $I_D(K)$  depends on the properties of the detection devices and we will give more information in the next section. The sample reflectivity profile  $r_s(L_s)$  is calculated from the inverse Fourier transform of  $I_D(K)$ . Applying the tricks of the Fourier transform,  $\frac{1}{2}[\delta(L+L_0)+\delta(L-L_0)] \xrightarrow{F} \cos(kL_0)$  to the inverse Fourier transform of equation (15),

$$\begin{aligned} i_D(L) = & \frac{\rho}{8} \left[ \gamma(L) [R_R + R_{S_1} + R_{S_2} + \dots] \right] \\ & + \frac{\rho}{4} \left[ \gamma(L) \otimes \sum_i \sqrt{R_R R_{S_i}} \left( \delta(z \pm 2(L_R - L_{S_i})) \right) \right] \\ & + \frac{\rho}{4} \left[ \gamma(L) \otimes \sum_{i \neq j} \sqrt{R_{S_i} R_{S_j}} \left( \delta(z \pm 2(L_{S_i} - L_{S_j})) \right) \right] \end{aligned} \quad (21)$$

where  $\gamma(L)$  is the inverse Fourier transform of  $S(k)$ . Carrying out the convolution property of Fourier transforms  $x(z) \otimes y(z) \xleftrightarrow{F} X(k) Y(k)$  and taking advantage of the shifting property of the delta function, we obtain the result of the interferometric measurement, referred to as the ‘‘A-scan’’:

$$\begin{aligned} i_D(L) = & \frac{\rho}{8} \left[ \gamma(L) (R_R + R_{S_1} + R_{S_2} + \dots) \right] \\ & + \frac{\rho}{4} \left[ \sum_i \sqrt{R_R R_{S_i}} \gamma \left[ L \pm 2(L_R - L_{S_i}) \right] \right] \\ & + \frac{\rho}{4} \left[ \sum_{i \neq j} \sqrt{R_{S_i} R_{S_j}} \gamma \left[ L \pm 2(L_{S_i} - L_{S_j}) \right] \right] \end{aligned} \quad (22)$$

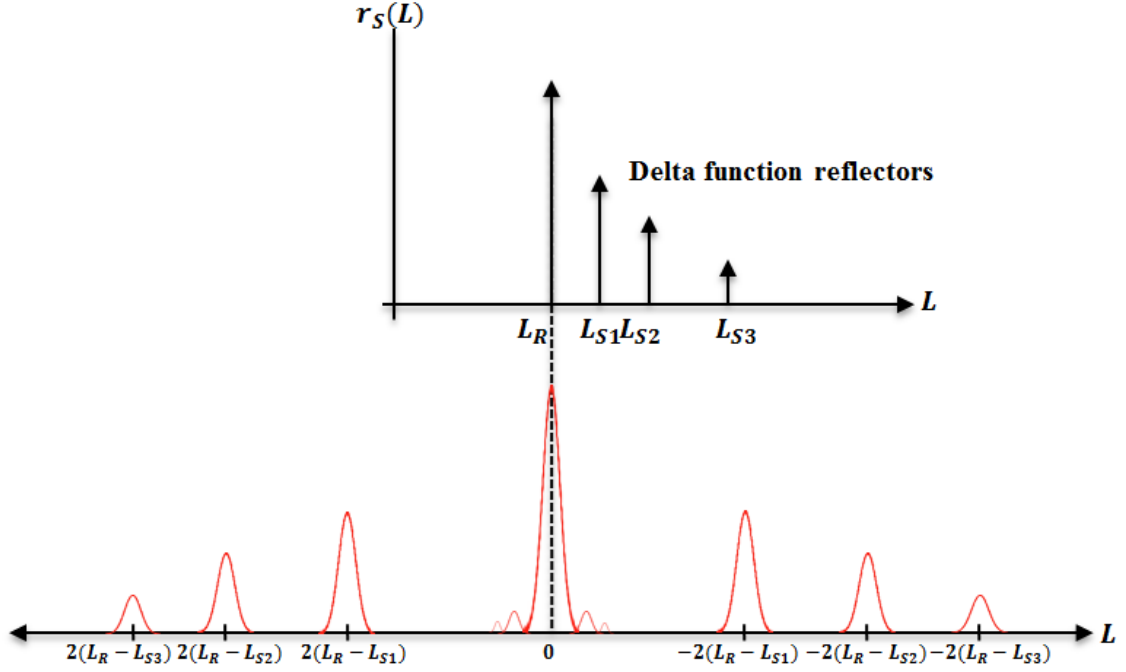


**Figure 2.6. Illustration of the three discrete reflectors having delta function of field reflectivity in sample (top) and the A-scan acquired by FD-OCT.**

Based on equation (22) and Figure 2.6, “A-scan” data has huge DC term because the reflectance of the reference typically dominates the other reflectors in the sample. In the cross-correlation components and the main A-scan signals, each position of the signal is proportional to the relative distance of the reflectors from the reference. The factor of 2 can be explained as round-trip distance to each reflector. Additionally, the reflector signals having delta function are broadened or blurred to the width of coherence length of the light source. According to the equation (17), the coherence length of the system is proportional to the square of center wavelength and inversely proportional to the bandwidth of the light source. That means OCT imaging system can achieve higher resolution when it uses a light source having shorter center wavelength and broad bandwidth. The auto-correlation components typically have low intensity and locate near

DC because the distance between each reflector in sample is very close. Due to the property of Fourier transform, there are mirror images. These mirror images are not serious so long as the sample can be kept entirely to one side of the zero path length.

### 2.2.3.1 Spectral-Domain OCT (SD-OCT) and Swept-Source OCT (SS-OCT)

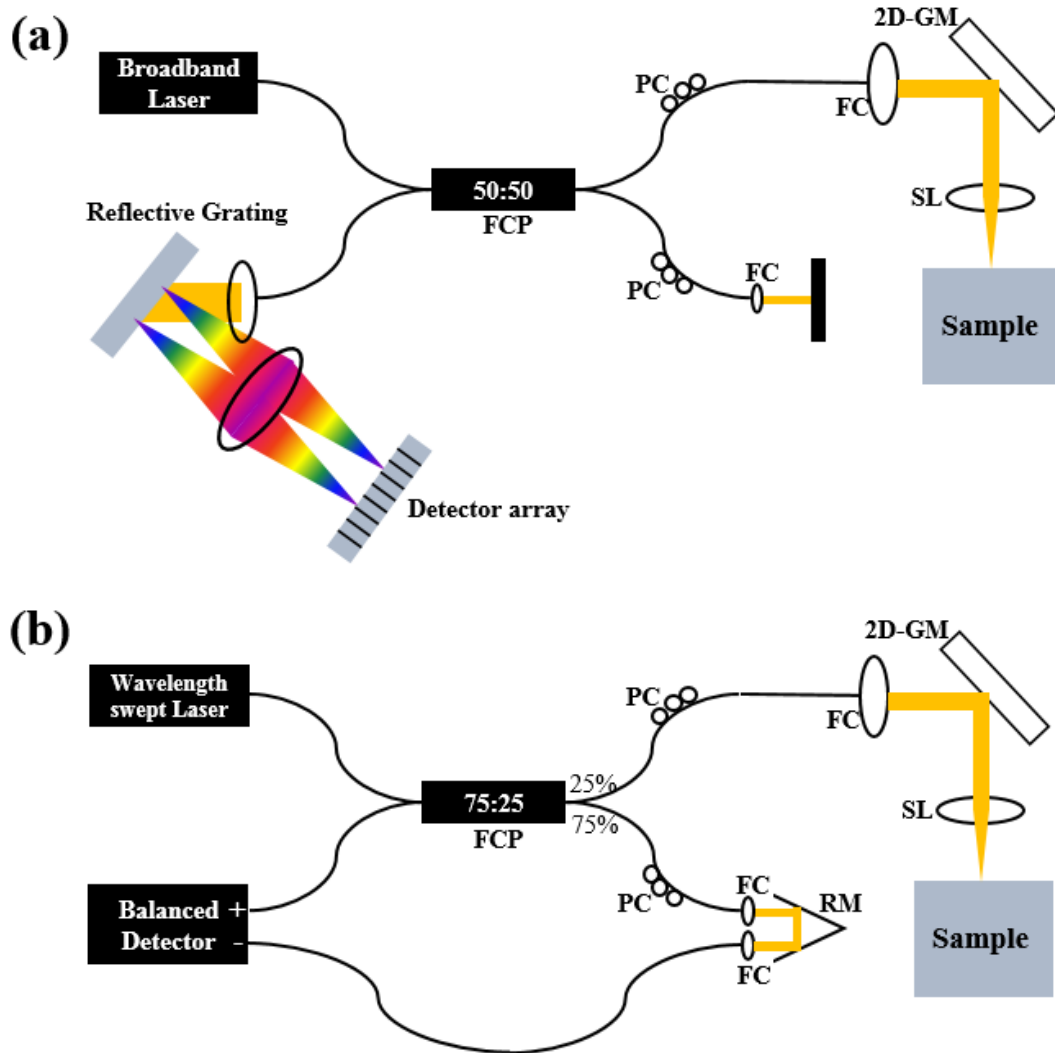


**Figure 2.7. Schematics of (a) SD-OCT and (b) SS-OCT configurations. Fix (b)-wavelength swept laser**

FD-OCT can be subsequently divided into two categories: 1) spectrometer-based (SD) and 2) swept-source (SS) OCT depending on the types of light sources and detectors used

in the actual implementation of the system. There is a physical limitation in instrumentation for sampling the spectral interferogram, which limits spectral resolution, denoted by  $\delta_k$ . In SD-OCT,  $\delta_k$  is specified by the spectral resolution of the spectrometer as shown in Figure 2.7(a). The specific value of  $\delta_k$  is determined by the finite spacing of the detector array (CCD or CMOS) pixels and the optical setup among grating, focusing lens, and detector array. Additionally, the detector array measures the linearly spacing wavelength instead of wavenumber,  $k$ . As a result, the interferogram in wavelength should be transformed and interpolated to wavenumber domain[37]. The interpolation process is highly critical to the quality of the resultant OCT images. At the same time, it is very time consuming process, which is one of the large barrier for achieving real-time imaging. Whereas SD-OCT record the spectrally resolved intensity at the interferometer exit by a spectrometer detector array simultaneously in a parallel mode, more recently introduced SS-OCT time-encodes wavenumber by rapidly tuning a narrowband source over a broad optical bandwidth[38] and  $\delta_k$  is limited by the instantaneous line shape of the sweeping laser source. Then, the instantaneous light frequency is  $\omega(t) = \omega_0 + \frac{d\omega}{dt} \cdot t$  and the phase delay between sample and reference beam is,

$$\delta_{SR}(\Delta L) = \frac{\Delta L}{c} \frac{d\omega}{dt} t \quad (23)$$

Hence, the interferogram shows the depth-related chirp frequency. In contrast to the FD-OCT, SS-OCT delivers k-clock signal for external devices such as digitizer in order to sample the interferogram by equally spacing wavenumber; as a result, interpolation process is unnecessary. SS-OCT system acquires signal at  $M$  evenly spaced wavenumbers, such that  $M \times \delta_k = \Delta k$  and  $\Delta k$  is the total optical bandwidth. In this setup, the system has a depth scan range,

$$L_{\max} = \frac{\pi M}{2\Delta k} = \frac{\pi}{2\delta k} = \frac{M}{2} l_c \quad (24)$$

To sum up, SS-OCT has three main attributes compared with SD-OCT: a longer imaging depth, less sensitivity roll-off with the imaging depth, and faster scanning speeds.

### 2.2.3.2 Balanced detector

In the case of SS-OCT, the system requires a single photo-detector to detect the interference signal. However, the system often uses a dual balanced detector set-up instead of a single detector as shown in Figure 2.7 in order to achieve better SNR[39], [40]. First, balanced-detection (BD) can suppress background noise and autocorrelation artifacts. Next, it is efficient in eliminating random intensity noise and shot noise. This method is fundamentally based on a differential amplifier configuration as shown in Figure 2.8.

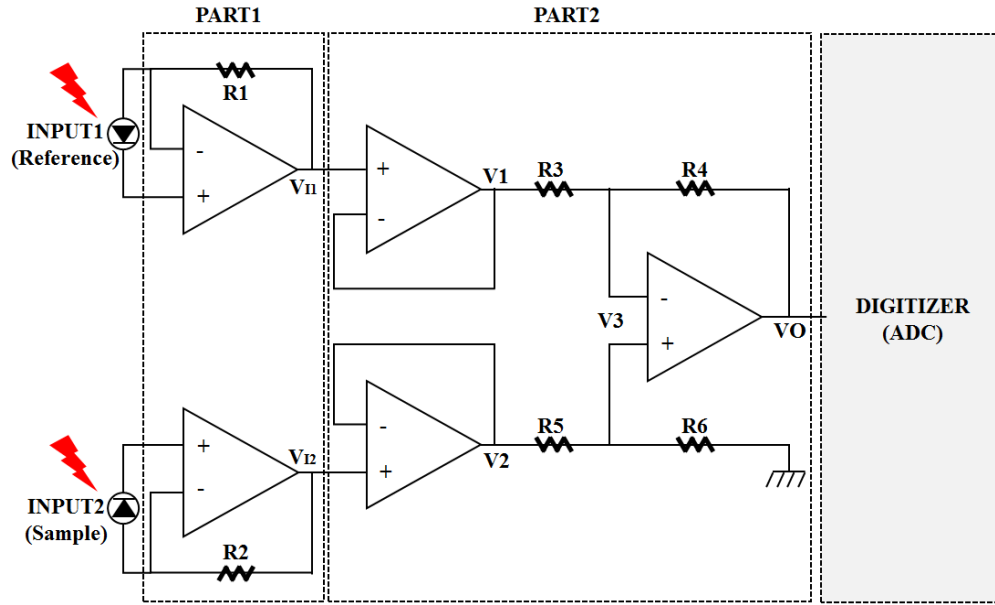


**Figure 2.8.** Schematic of balanced detection circuit consists of voltage follower to transform the input current to output voltage and differential amplifier to reject the common-mode of the inputs: reference and sample currents.



First, the system is divided into two parts to analyze the BD system. The first part is voltage follower circuit to transform the sampled photo-electric current to a measurable voltage signal output. Figure 2.9 shows in details how to convert the current signal into voltage signal. First, the voltage follower circuit can be simply redrawn as a resistive circuit as shown in Figure 2.9(b). Here, we assume that the input resistance of the operational amplifier (OP-AMP) is infinite. We can simply ignore the infinite resistance when we calculate the resistance of the parallel connection with the infinite resistance. Finally, based on Norton equivalent circuit, the circuit can be converted to the circuit as shown in Figure 2.9(d). Thus, the input voltages in part two in Figure 2.9 are

$$V_{I1} = R1 \times i_R \quad (25)$$

$$V_{I2} = R2 \times i_S \quad (26)$$

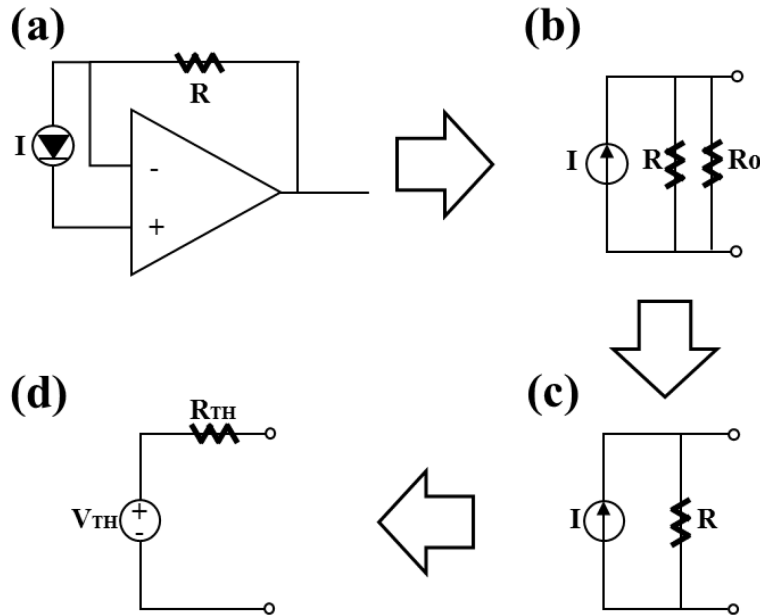


**Figure 2.9. Norton equivalent circuit to analyze the voltage follower circuit, which transform the sampled photo-electric current generated by the interference signal into measurable voltage signal.**

Now, we are ready to calculate the output voltage of the differential amplifier. Applying simple circuit theories and properties of the OP-AMP, we can derive the output voltage of the circuit:

$$V1 = V_{I1}$$

$$V2 = V_{I2}$$

$$\frac{V3 - V1}{R3} + \frac{V3 - VO}{R4} = 0$$

$$\frac{V3 - V2}{R5} + \frac{V3}{R6} = 0$$

$$V3 = \frac{R6}{R5 + R6} V2$$

$$VO = \frac{R6(R3 + R4)}{R3(R5 + R6)} V2 - \frac{R4}{R3} V1 \quad (27)$$

If the resistance values of R3 to R6 are same then, the output voltage value is,

$$VO = V2 - V1 \quad (28)$$

Further, we plug in the equation (25) and (26) into (28), then we finally have

$$VO = R_i(i_S - i_R) \quad (29)$$

This property of the differential amplifier is known as common-mode rejection ratio (CMRR). An ideal differential amplifier would have infinite CMRR. Thus, only the differential signal from the sample and reference arms should be amplified in the presence of the large common-mode input in BD system.

## 2.3 Common-path OCT

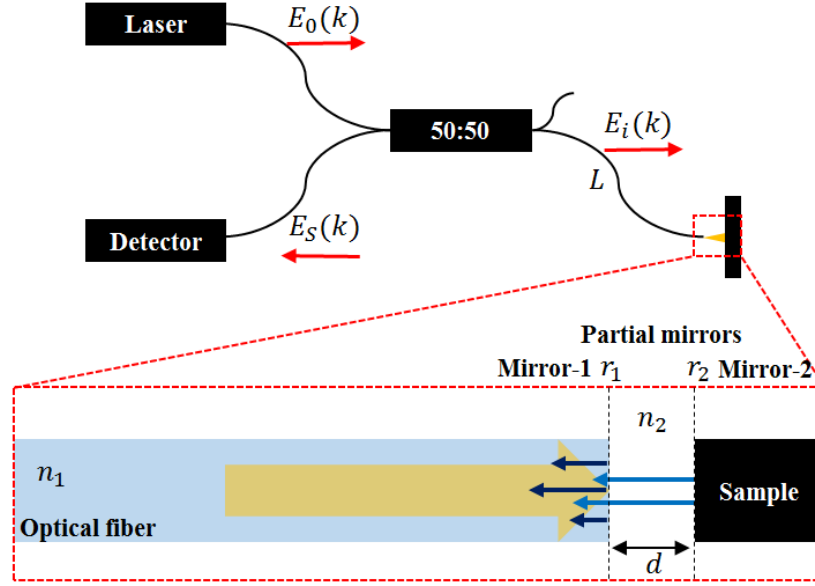


**Figure 2.10. Schematic of common-path OCT (CP-OCT) setup (top) and magnified image of the probe-tip (bottom).**

For distal sensing and axial surgical tool guidance, we have developed and incorporated common-path OCT (CP-OCT) designed specifically for handheld microsurgical tools. In a common-path OCT (CP-OCT) system, the reference signal is obtained by the reflection at the fiber-tip, which occurs at an interface surface between the optical fiber and the outside medium (typically air) so that the reference light and the sample light travel in the same optical path or common-path. For this reason, CP-OCT allows a simple design, dispersion free properties, relatively low cost and the potential for disposability[30] as shown in Figure 2.10.

### 2.3.1 Fabry–Pérot interferometer

CP-OCT can be interpreted as Fabry–Pérot interferometer, which consists of a transparent plate with two reflecting surfaces. In CP-OCT configuration, the first reflecting surface is the fiber-tip and the second surface is the sample surface.

### 2.3.1.1 CP-OCT with lossless medium

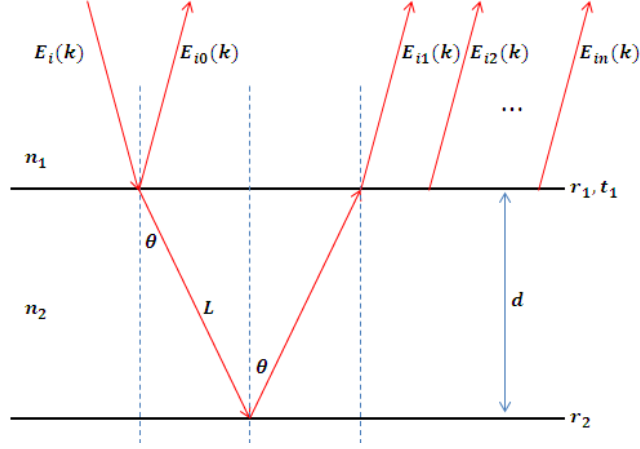


**Figure 2.11. Ray-tracing of the Fabry–Pérot interferometer with lossless medium between the mirrors.**

For simplicity, let's assume that  $n_1$ ,  $n_2$ ,  $r_1$ ,  $r_2$  are real values and the direction of the incident beam to the partial mirror-1 is perpendicular to the surface of the mirror. Similar to equation (10),

$$E_0(k) = s(k)e^{jkz} \quad (30)$$

Here, we omit the angular term for simplicity. The broadband light source has Gaussian shape with a center wavelength of  $\lambda_0$  and bandwidth of  $\lambda_B$ . The bandwidth of the light source is decided by the full width at the half maximum (FWHM) of the peak,

$$FWHM = 2\sqrt{-2\ln 0.5}c \approx 2.35482c \quad (31)$$

where  $c$  is related to the full width at half maximum of the peak. After passing through the 50:50 coupler, the electrical field of the light is

$$E_i(k) = \frac{E_0(k)}{\sqrt{2}} \quad (32)$$

Now, we need to focus on the fundamental theory of the Fabry–Pérot interferometer. The incident beam to the Fabry–Pérot interferometer is defined as  $E_i(k)$ . Then, the incident

beam experience interference due to the two partial mirrors. First, we need to define the basic parameters to describe the interferometer setup.

$$L = \frac{d}{\cos(\theta)} \quad (33)$$

$$t_1 = \sqrt{1 - r_1^2} \quad (34)$$

where  $d$  and  $L$  are the distance and OPL between the mirrors, respectively and  $\theta$  is the refracted angle after passing the first mirror and it has  $\pi/2$  in this setup. Transmission coefficient,  $t_1$ , can be calculated from the fact that the total sum of transmittance and reflectance is equal to one. There are multiple reflections between the mirrors and this effect creates multiple coherent lights having different OPL:

$$\begin{aligned} E_{i0}(k) &= E_i(k)r_1 \\ E_{i1}(k) &= E_i(k)t_1 \cdot \left[ e^{jn_2kL} r_2 e^{jn_2kL} \right] \cdot t_1 \\ E_{i2}(k) &= E_i(k)t_1 \cdot \left[ e^{jn_2kL} r_2 e^{jn_2kL} \right] \cdot r_1 \cdot \left[ e^{jn_2kL} r_2 e^{jn_2kL} \right] \cdot t_1 \\ &\dots \\ E_{in}(k) &= E_i(k)t_1^2 \cdot r_1^{n-1} \left[ r_2 e^{jn_2kL} \right]^n \end{aligned} \quad (35)$$

The total sum of the reflective waves and the electric field coming to the detector are,

$$\begin{aligned} E_r(k) &= E_i(k) \left\{ r_1 + t_1^2 \sum_{n=1}^{\infty} r_1^{n-1} \left( r_2 e^{j2n_2kL} \right)^n \right\} = E_i(k) \left\{ r_1 + \frac{t_1^2}{r_1} \sum_{n=1}^{\infty} \left( r_1 r_2 e^{j2n_2kL} \right)^n \right\} \\ E_r(k) &= E_i(k) \left\{ r_1 + \frac{t_1^2}{r_1} \cdot \frac{r_1 r_2 e^{j2n_2kL}}{1 - r_1 r_2 e^{j2n_2kL}} \right\} \end{aligned} \quad (36)$$

$$E_s(k) = \frac{E_r(k)}{\sqrt{2}} = \frac{E_0(k)}{2} \left\{ r_1 + \frac{t_1^2}{r_1} \cdot \frac{r_1 r_2 e^{\frac{j2n_2 kd}{\cos \theta}}}{1 - r_1 r_2 e^{\frac{j2n_2 kd}{\cos \theta}}} \right\} \quad (37)$$

Here the factor of 2 comes from the double pass through the 50:50 coupler. As mentioned eariler, we assume the  $\theta$  is zero that means the incident beam is perpendicular to the surface of the mirror-1. The output current of the detector is proportional to the square of the electrical field.

$$I_s(k) \propto |E_s(k)|^2 = E_s(k) E_s(k)^* \quad (38)$$

$$I_s(k) = \frac{A|E_0(k)|^2}{4} \left\{ r_1 + \frac{t_1^2}{r_1} \cdot \frac{r_1 r_2 e^{j2n_2 kd}}{1 - r_1 r_2 e^{j2n_2 kd}} \right\} \left\{ r_1 + \frac{t_1^2}{r_1} \cdot \frac{r_1 r_2 e^{-j2n_2 kd}}{1 - r_1 r_2 e^{-j2n_2 kd}} \right\} \quad (39)$$

where A is constant coefficient. To more simplify the the Equation (39),

$$\begin{aligned} I_s(k) &= \frac{A|E_0(k)|^2}{4} \left\{ r_1^2 + t_1^2 (P + P^*) + \frac{t_1^4}{r_1^2} PP^* \right\} \\ P &= \frac{r_1 r_2 e^{j2n_2 kd}}{1 - r_1 r_2 e^{j2n_2 kd}}, \quad P^* = \frac{r_1 r_2 e^{-j2n_2 kd}}{1 - r_1 r_2 e^{-j2n_2 kd}}, \\ P + P^* &= \frac{r_1 r_2 e^{j2n_2 kd}}{1 - r_1 r_2 e^{j2n_2 kd}} + \frac{r_1 r_2 e^{-j2n_2 kd}}{1 - r_1 r_2 e^{-j2n_2 kd}} = \frac{2r_1 r_2 (\cos(\beta k) - r_1 r_2)}{1 + (r_1 r_2)^2 - 2r_1 r_2 \cos(\beta k)} \\ PP^* &= \frac{r_1 r_2 e^{j2n_2 kd}}{1 - r_1 r_2 e^{j2n_2 kd}} \cdot \frac{r_1 r_2 e^{-j2n_2 kd}}{1 - r_1 r_2 e^{-j2n_2 kd}} = \frac{(r_1 r_2)^2}{1 + (r_1 r_2)^2 - 2r_1 r_2 \cos(\beta k)} \end{aligned}$$

where  $\beta = 2n_2 d$ . Finally, we can get the equation to show the relationship between the photo-electric current and wavenumber of the light source.

$$I_s(k) = \frac{A|E_0(k)|^2}{4} \left\{ r_1^2 + \frac{r_2^2 t_1^4 - 2r_1^2 r_2^2 t_1^2 + 2r_1 r_2 t_1^2 \cos(2n_2 d \cdot k)}{1 + (r_1 r_2)^2 - 2r_1 r_2 \cos(2n_2 d \cdot k)} \right\} \quad (40)$$

Now, we need to set the parameter values for more realistic simulation. In this simulation, we will use that  $\lambda_0$ ,  $\lambda_B$ ,  $r_l$ , and  $r_2$  are 1000nm, 50nm, 0.2, and 0.15, respectively. The distances between the two mirrors are used two values: 50 and 100 micrometers. First, the equation of the broadband light source which has Gaussian shape is

$$|E_0(\lambda)|^2 = e^{\frac{-(\lambda-\lambda_0)^2}{2\left(\frac{\lambda_B}{2.355}\right)^2}} = e^{\frac{(\lambda-10^{-6})^2}{9.02 \times 10^{-16}}} \quad (41)$$

$$|E_0(k)|^2 = e^{\frac{\left(\frac{2\pi}{k}-10^{-6}\right)^2}{9.02 \times 10^{-16}}} \quad (42)$$

where  $|E_0(\lambda)|^2$  and  $|E_0(k)|^2$  are the intensity equations of the same light source based on wavelength and wavenumber, respectively. The graphs of the above two equations are shown in Figure 2.12. The graph of  $|E_0(k)|^2$  has a shape similar to Gaussian graph. If we plug in the equation (42) into (40), we can draw the interferogram of the system and subsequently get the A-scan data after applying inverse Fourier transform. Additionally, we also calculate the system transfer function when we only eliminate the light source term in equation (40). The simulated CP-OCT results in both cases including d are 50 and 100 micrometer are shown in Figure 2.13.

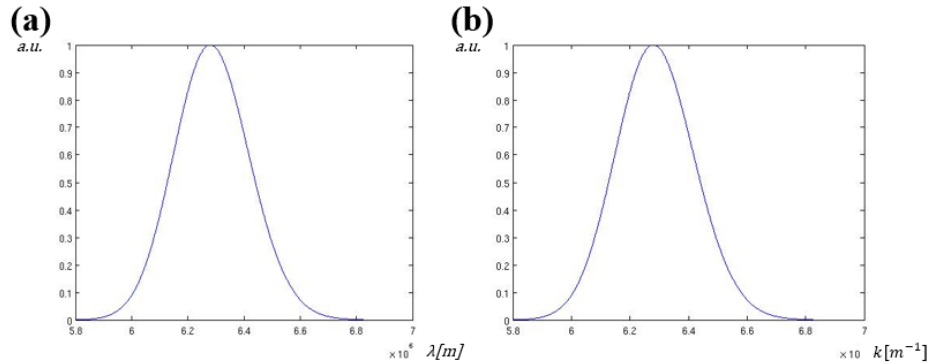


**Figure 2.12. Light source intensity graph having Gaussian shape in a) wavelength domain and b) wavenumber domain.**

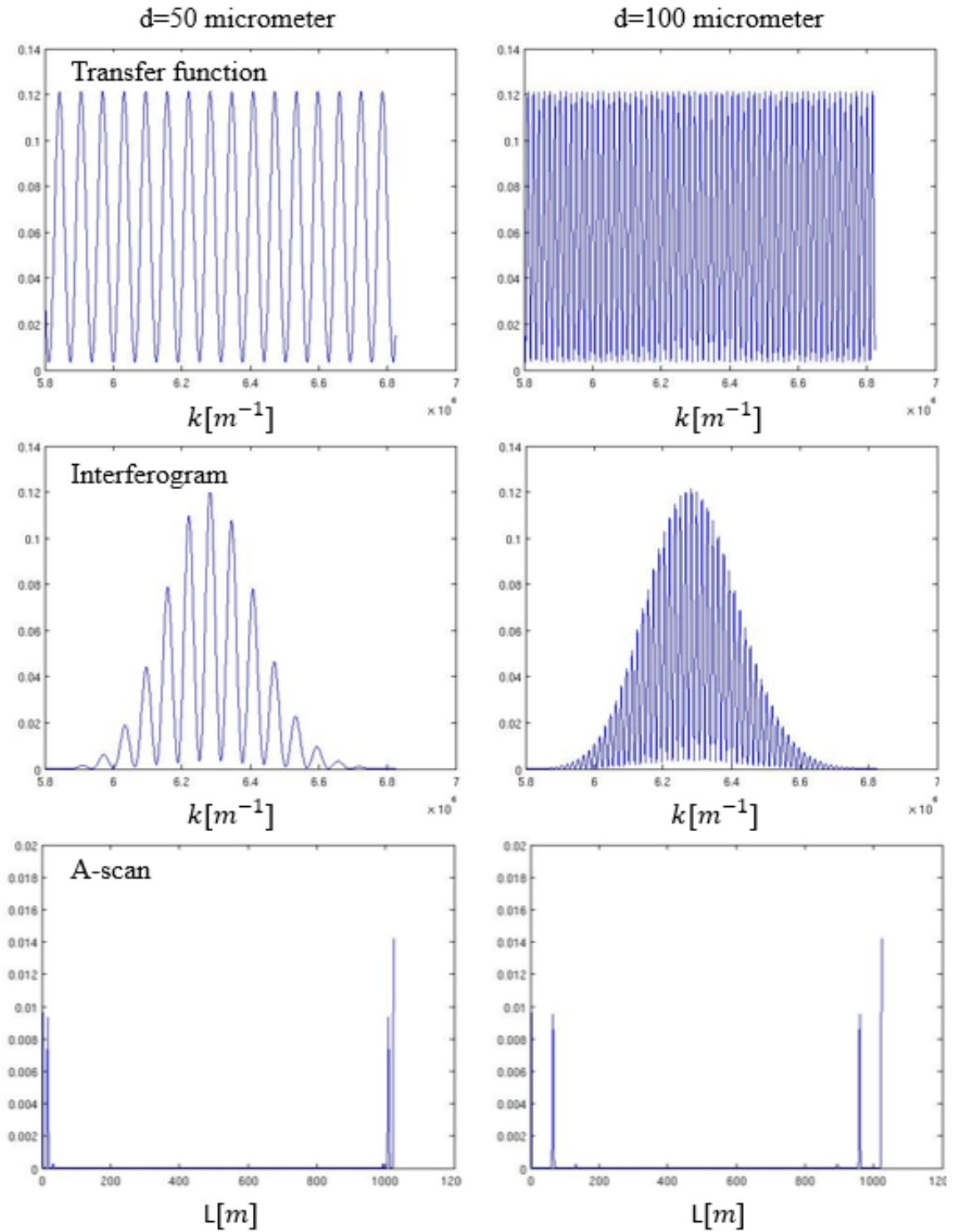


**Figure 2.13.** Fabry-Pérot interferometer simulation results including system transfer function, interferogram, and A-scan with lossless medium. Left side is the result of  $d = 50$  micrometer and right side is of  $d = 100$  micrometer.



### 2.3.1.2 CP-OCT with lossy medium

Now, we assume that the light is travelling in lossy medium. Specifically, the loss is dependent on a wavelength,  $\alpha = 1 * (\lambda / \lambda_0)$ . Then, the previous equations should be modified to include the loss term.

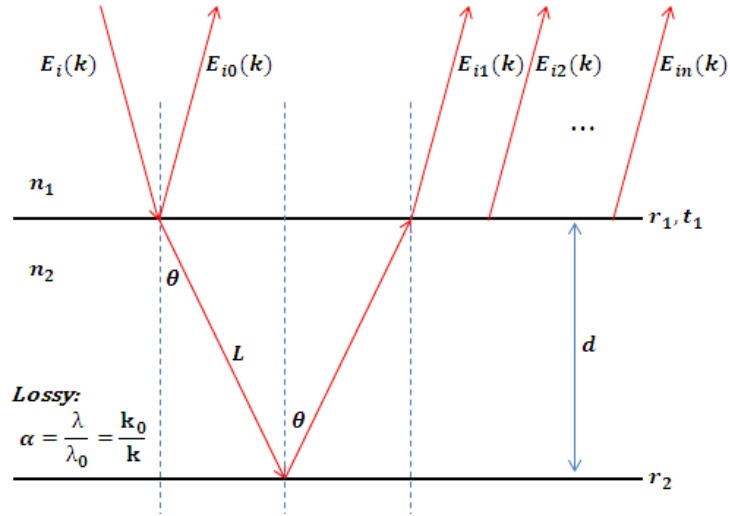


**Figure 2.14. Ray-tracing of the Fabry-Pérot interferometer with lossy medium between the mirrors.**

$$\alpha = \frac{\lambda}{\lambda_0} = \frac{k_0}{k} \quad (43)$$

where alpha is the attenuation coefficient. The derivation process is similar to the previous one except the attenuation term.

$$E_{i0}(k) = E_i(k)r_1$$

$$E_{i1}(k) = E_i(k)t_1 \cdot \left\{ e^{-\alpha L} e^{jn_2 k L} \cdot r_2 \cdot e^{-\alpha L} e^{jn_2 k L} \cdot t_1 \right\}$$

$$E_{i2}(k) = E_i(k)t_1 \cdot \left\{ r_2 \cdot e^{-2\alpha L} e^{j2n_2 k L} \right\} \cdot r_1 \cdot \left\{ r_2 \cdot e^{-2\alpha L} e^{j2n_2 k L} \cdot t_1 \right\} \cdot t_1$$

...

$$E_{in}(k) = E_i(k)t_1^2 \cdot r_1^{n-1} \left\{ r_2 \cdot e^{-2\alpha L} e^{j2n_2 k L} \right\}^n$$

$$E_r(k) = E_i(k) \left\{ r_1 + t_1^2 \sum_{n=1}^{\infty} r_1^{n-1} \cdot \left\{ r_2 e^{-2\alpha L} e^{j2n_2 k L} \right\}^n \right\} = E_i(k) \left\{ r_1 + \frac{t_1^2}{r_1} \sum_{n=1}^{\infty} \left\{ r_1 r_2 e^{-2\alpha L} e^{j2n_2 k L} \right\}^n \right\}$$

$$E_r(k) = E_i(k) \left\{ r_1 + \frac{t_1^2}{r_1} \cdot \frac{r_1 r_2 e^{-2\alpha L} e^{j2n_2 k L}}{1 - r_1 r_2 e^{-2\alpha L} e^{j2n_2 k L}} \right\} \quad (44)$$

$$E_s(k) = \frac{E_r(k)}{\sqrt{2}} = \frac{E_0(k)}{2} \left\{ r_1 + \frac{t_1^2}{r_1} \cdot \frac{r_1 r_2 e^{-\frac{2k_0 d}{k}} e^{j2n_2 k d}}{1 - r_1 r_2 e^{-\frac{2k_0 d}{k}} e^{j2n_2 k d}} \right\} \quad (45)$$

Based on the above electric field equation of the interferogram, we can calculate the output current of the photo-detector.

$$I_s(k) \propto |E_s(k)|^2 = E_s(k) E_s(k)^*$$

$$I_s(k) = \frac{A|E_0(k)|^2}{4} \left\{ r_1 + \frac{t_1^2}{r_1} \cdot \frac{r_1 r_2 e^{-\frac{2k_0 d}{k}} e^{j2n_2 k d}}{1 - r_1 r_2 e^{-\frac{2k_0 d}{k}} e^{j2n_2 k d}} \right\} \left\{ r_1 + \frac{t_1^2}{r_1} \cdot \frac{r_1 r_2 e^{-\frac{2k_0 d}{k}} e^{-j2n_2 k d}}{1 - r_1 r_2 e^{-\frac{2k_0 d}{k}} e^{-j2n_2 k d}} \right\}$$

$$I_s(k) = \frac{A|E_0(k)|^2}{4} \left\{ r_1^2 + t_1^2 (P + P^*) + \frac{t_1^4}{r_1^2} P P^* \right\}$$

$$P = \frac{r_1 r_2 e^{-\frac{2k_0 d}{k}} e^{j2n_2 k d}}{1 - r_1 r_2 e^{-\frac{2k_0 d}{k}} e^{j2n_2 k d}}, \quad P^* = \frac{r_1 r_2 e^{-\frac{2k_0 d}{k}} e^{-j2n_2 k d}}{1 - r_1 r_2 e^{-\frac{2k_0 d}{k}} e^{-j2n_2 k d}}$$

$$I_s(k) = \frac{A|E_0(k)|^2}{4} \left\{ r_1 + \frac{(r_1^2 t_1^4 - 2r_1^2 r_2^2 t_1^2) e^{-\frac{4k_0 d}{k}} + 2r_1 r_2 t_1^2 e^{-\frac{2k_0 d}{k}} \cos(2n_2 d \cdot k)}{1 + (r_1 r_2)^2 e^{-\frac{4k_0 d}{k}} - 2r_1 r_2 e^{-\frac{2k_0 d}{k}} \cos(2n_2 k d)} \right\} \quad (46)$$

The simulated CP-OCT interferograms with different attenuation coefficients are shown in Figure 2.14 ~ 2.16 in the same manner as Figure 2.13. Specifically, we used three different attenuation coefficients:  $\alpha$ ,  $25\alpha$ , and  $50\alpha$  to show the attenuation effect on the signal more clearly.

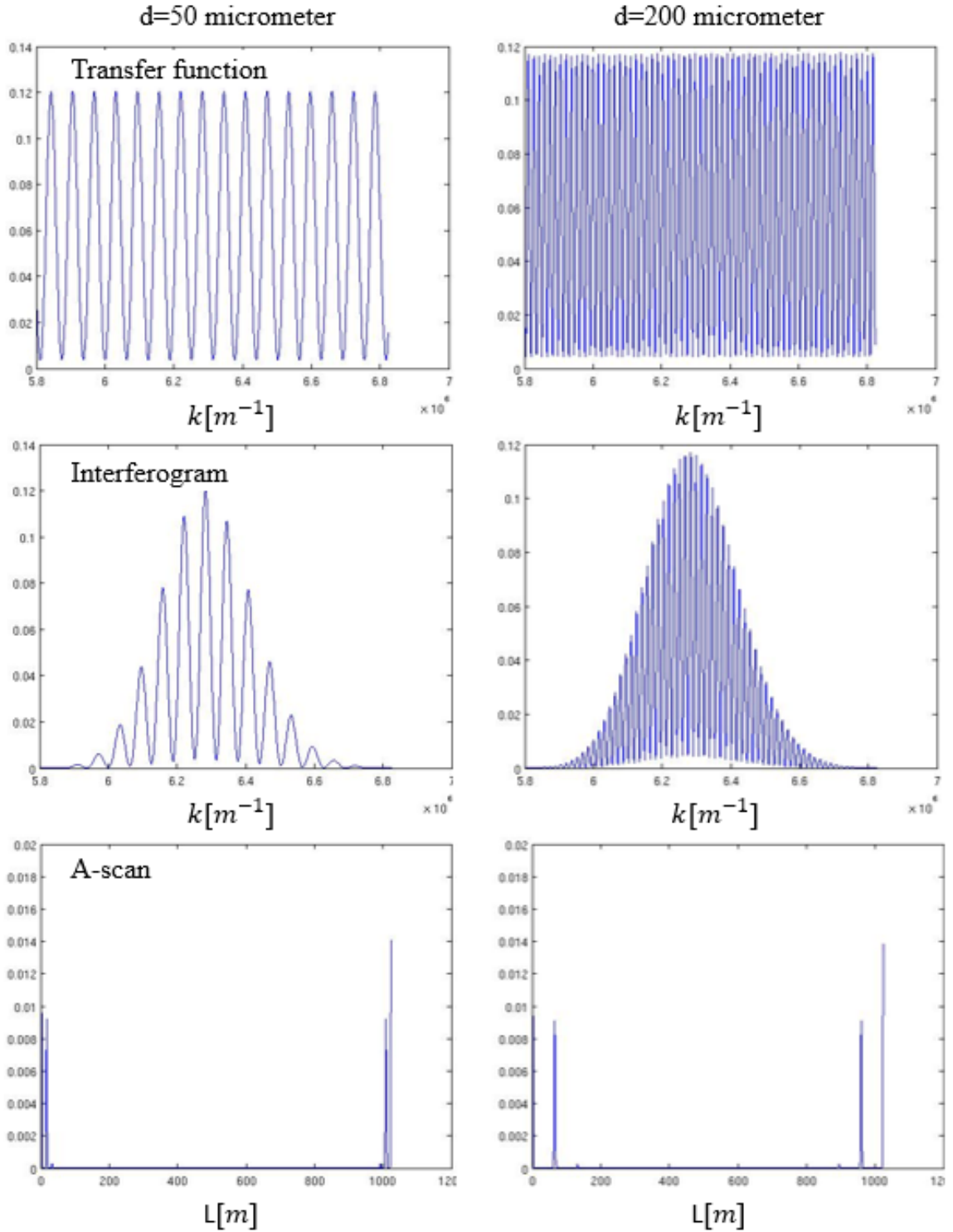


**Figure 2.15.** Fabry-Pérot interferometer simulation results including system transfer function, interferogram, and A-scan with lossy medium. Attenuation coefficient is  $\alpha$ . Left side is the result of  $d = 50$  micrometer and right side is of  $d = 200$  micrometer.

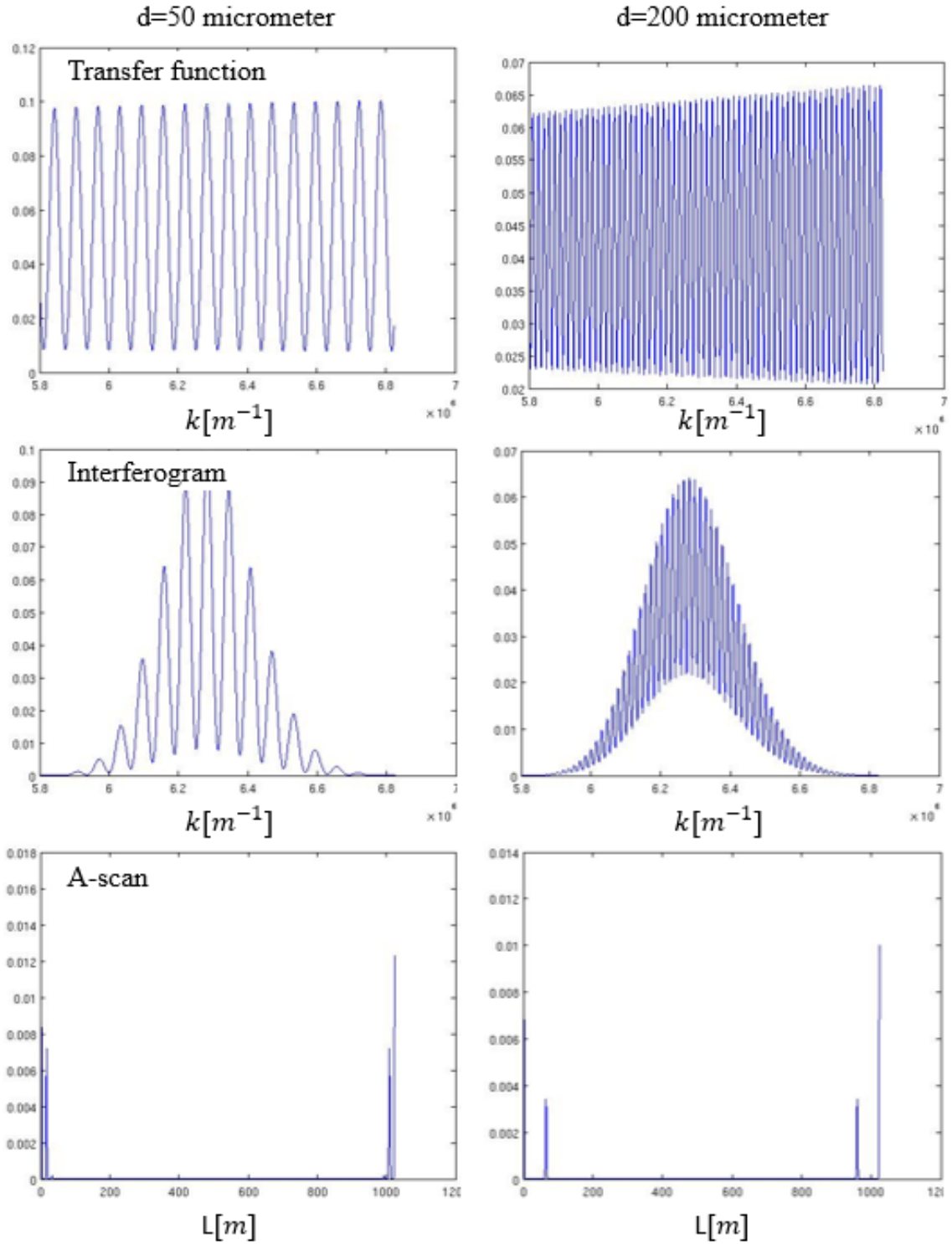


**Figure 2.16.** Fabry-Pérot interferometer simulation results including system transfer function, interferogram, and A-scan with lossy medium. Attenuation coefficient is  $25a$ . Left side is the result of  $d = 50$  micrometer and right side is of  $d = 200$  micrometer.

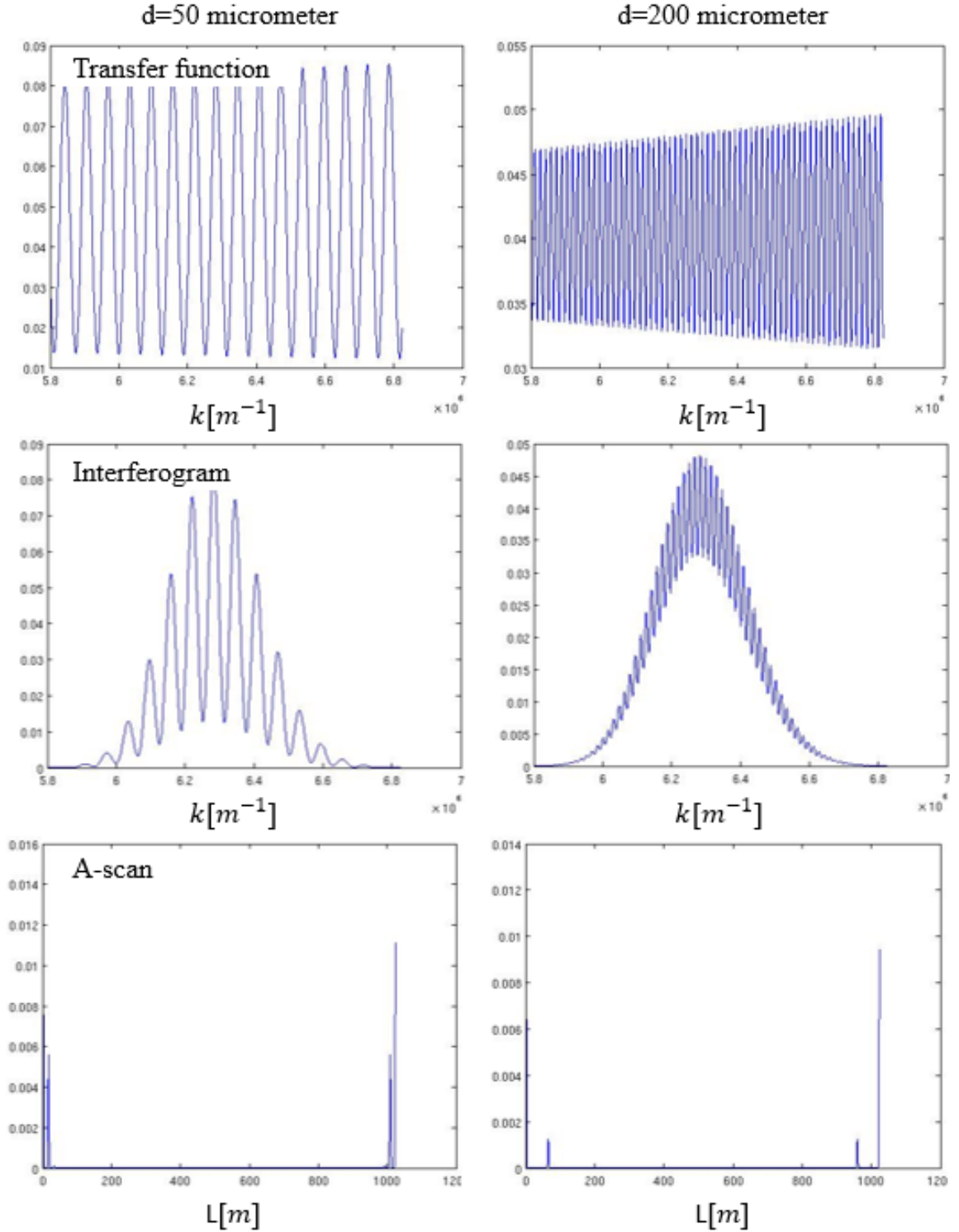


**Figure 2.17.** Fabry-Pérot interferometer simulation results including system transfer function, interferogram, and A-scan with lossy medium. Attenuation coefficient is  $50\alpha$ . Left side is the result of  $d = 50$  micrometer and right side is of  $d = 200$  micrometer.

### 2.3.2 Ball lens

There are limitations when the system uses a bare fiber as a sensor probe. One of the main drawbacks is that the laser output from the single mode fiber probe diverges rapidly and the output power decreases exponentially with the depth. To prevent this rapid power fall-off, lensed fiber probes have been developed and applied[41]–[43]. A CP-OCT probe based on a built-in conical micro-lens showed a significant improvement in signal-to-noise ratio (SNR)[42]. However, such lensed fiber probes exhibit limited performance in aqueous environments due to the fact that it uses the reflected beam at the fiber-tip as a reference beam. Thus, the intensity of the reference beam decreases when the fiber ( $n=1.5$ ) is moved from air ( $n=1.0$ ) into an aqueous environment such as saline ( $n=1.33$ ) or vitreous. To overcome this limitation, a sapphire ball lens having high reflective index ( $n=1.77$ ) was used at the tip of the glass fiber to attain SNR improvement. There are a number of advantages to this approach which includes a high focusing power, protecting the fragile fiber-tip, and creation of a stable reference[44].

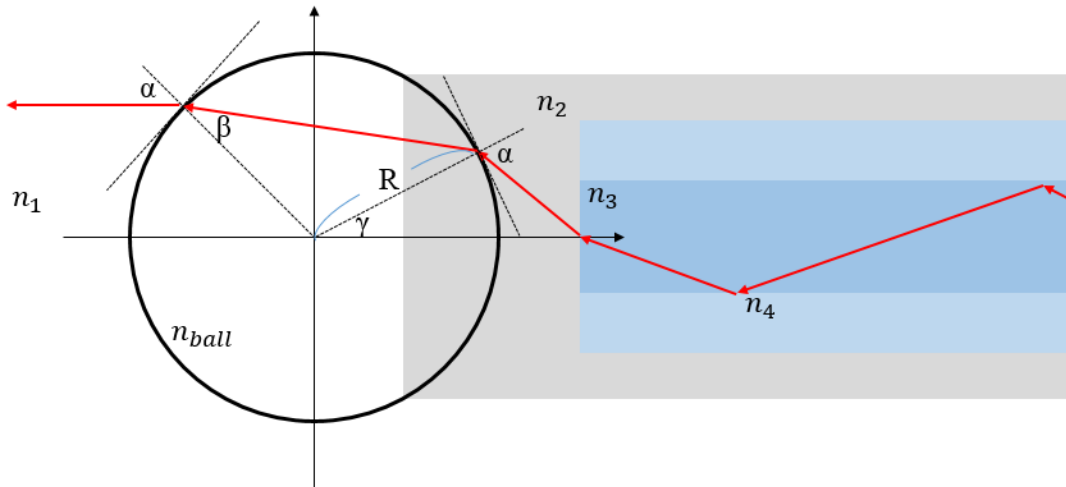


**Figure 2.18. Ray-tracing in ball lens and SMF.**

Ray-tracing of a system consists of a ball-lens and SMF is shown in Figure 2.18. The exit angle from the SMF to air is decided by  $NA$  specified in equation (4). Red arrow lines represent the ray path and the dotted lines are for measurement. The angle  $\beta$  is found from Snell's Law. The angle  $\gamma$  in the figure is,

$$\gamma = \pi - [\alpha + (\pi - 2\beta)] = 2\beta - \alpha, \quad (47)$$

Then, we can find the  $x$  and  $y$  in order to calculate the distance between ball lens and fiber,

$$d = x + y - R \quad (48)$$

where  $x$  is  $R\cos(\gamma)$  or  $R\cos(2\beta - \alpha)$ . To find length  $y$ , we need to use the fact that the exit angle of the incident beam is the same as entrance angle. Then, we can find the length  $z$  and  $y$  sequentially.

$$z = R \sin(2\beta - \alpha)$$

$$\frac{z}{y} = \tan(\alpha - \gamma) = \tan(2\alpha - 2\beta)$$

$$y = R \cos(2\alpha - 2\beta) \frac{\sin(2\beta - \alpha)}{\sin(2\alpha - 2\beta)}$$

Thus,  $d$  between ball lens and SMF can be calculated as follows:

$$d = x + y - R = R[\cos(2\beta - \alpha) + \frac{\sin(2\beta - \alpha)}{\sin(2\alpha - 2\beta)} \cos(2\alpha - 2\beta) - 1] \quad (49)$$

Here, the angles,  $\alpha$ ,  $\beta$ , and  $\theta_a$  are functions of refractive indices:  $n_1$  to  $n_4$ ; therefore, the distance between ball lens and SMF to achieve collimated beam is also decided by the refractive indices of SMF, ball lens, and surround media.

### 2.3.3 Ghost image

The introduction of a high index sapphire ball lens causes severe noises that result from the two highly reflective sapphire ball lens surfaces which in turn produce two additional references. One of the noises comes from autocorrelation noise. This type of noise has been extensively studied in prior works[45]–[48]. Among the methods, minimum variance mean line subtraction can effectively reduce this fixed-pattern noise[46]. However, the other mixed noise induced by correlation between sample-reflected light and multiple reference-reflected lights create multiple ghost images and cannot be easily eliminated due to its variability in shape and position. There were some studies to actively utilize multiple references in order to expand imaging domain size and remove dc term as well as mirror noise using electro-optic phase modulator or piezoelectric fiber stretcher[48], [49]. These methods use electro or mechanical actuators to achieve multiple references but they still incorporate one reference at a time. In the present work, we utilize a Fourier domain image processing approach known images from the multiple fixed references are shifted and summed appropriately to diminish distortion in the OCT images.

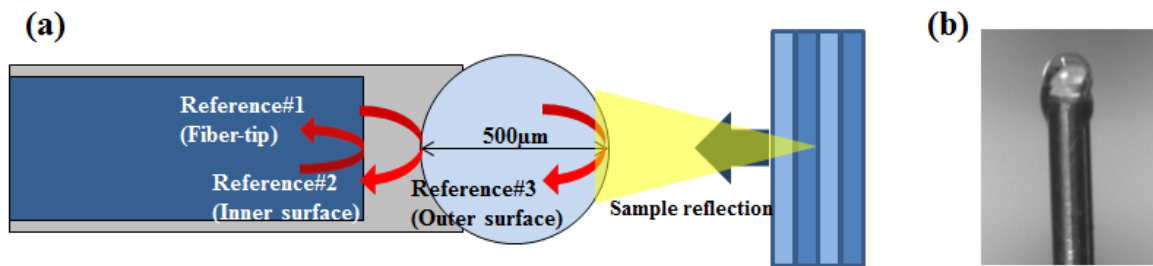


**Figure 2.19. Schematic of the system; (a) fiber probe with sapphire ball lens having 500μm diameter, (b) system overview, and (c) photo image of the probe.**



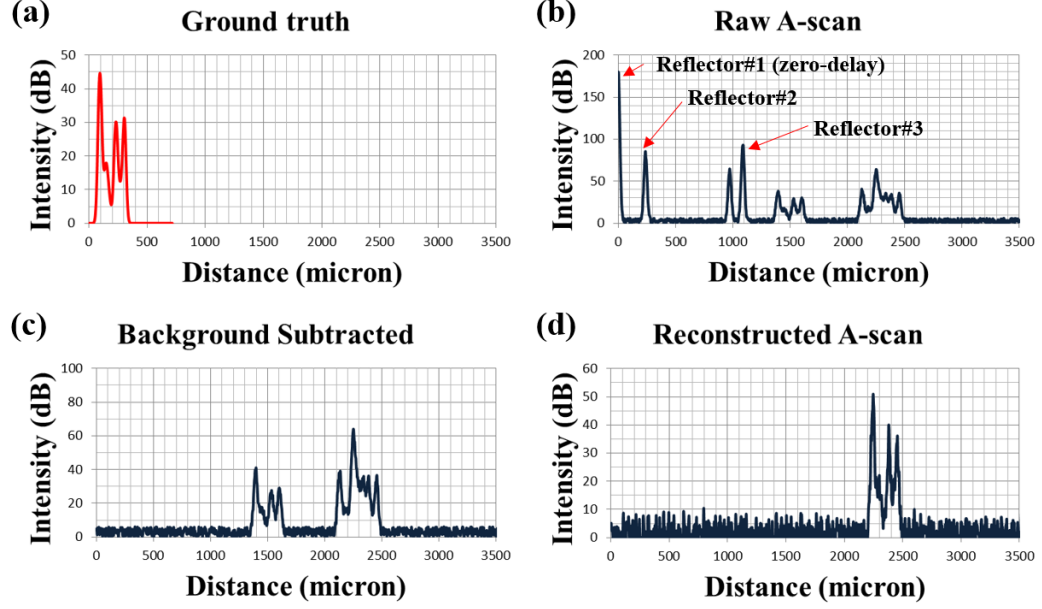


**Figure 2.20. Simulation result; (a) ground truth signal synthesized with the combination of ten reflectors, (b) simulated raw A-scan with random noise, (c) background (fixed) noise subtracted A-scan signal, and (d) the reconstructed signal graph.**

### 2.3.3.1 Deconvolution method to remove the ghost image

The output current  $I_D$  of the detector in interferometer with multiple references can be described as the following equation:

$$I_D(k, \omega) = \rho \left\langle \left| E_{R_1} + E_{R_2} + \dots + E_{R_m} + E_{S_1} + E_{S_2} + \dots + E_{S_n} \right|^2 \right\rangle \quad (50)$$

where  $k$ ,  $\omega$ , and  $\rho$  are wave number and angular frequency, and responsivity of the detector, respectively. Additionally,  $E_{R_m}$  and  $E_{S_n}$  are the reflected signals from multiple layers of reference and sample. The angular brackets denote integration over the response time of the detector and this time averaging eliminates the terms related to temporal frequency. We can rewrite the Equation (50) as shown in Equation (51),

$$I_D(k) = \rho \left| s(k) \sum_m^M t_{R_{m-1}} r_{R_m} e^{i2kz_{R_m}} + s(k) \prod_m^M t_{R_m} \sum_n^N r_{S_n} e^{i2kz_{S_n}} \right|^2 \quad (51)$$

where  $t$  ( $t_0 = 1$ ) and  $r$  are transitive and reflective coefficients of the reference and sample;  $s(k)$  is source spectrum. Then, we can get Equation (52) after expanding Equation (51) and then applying inverse Fourier transform,

$$\begin{aligned} i_D(z) = & \alpha_1 \left[ \gamma(z)(R_{R_1} + \dots + R_{R_M} + R_{S_1} + \dots + R_{S_N}) \right] \\ & + \alpha_2 \sum_m^M \sum_n^N \sqrt{R_{R_m} R_{S_n}} \left[ \gamma[2(z_{R_m} - z_{S_n})] + \gamma[-2(z_{R_m} - z_{S_n})] \right] \\ & + \alpha_3 \sum_{n \neq m=1}^M \sqrt{R_{R_n} R_{R_m}} \left[ \gamma[2(z_{R_m} - z_{R_n})] + \gamma[-2(z_{R_m} - z_{R_n})] \right] \\ & + \alpha_4 \sum_{n \neq m=1}^N \sqrt{R_{S_n} R_{S_m}} \left[ \gamma[2(z_{S_m} - z_{S_n})] + \gamma[-2(z_{S_m} - z_{S_n})] \right] \end{aligned} \quad (52)$$

where  $\gamma$  is coherence function and  $\alpha_n$  is the coefficient of each term including DC, cross-correlation, auto-correlation in reference, and auto-correlation in sample in turn. Based on Equation (52), we can deduce the shape of an A-scan having multiple references. First, we have a huge DC value at the zero position. Then, we have multiple sample signals having the same shape and the duplicate number is the same as the number of references. The A-scan also has large signals due to auto-correlation between references at fixed positions and we can typically ignore the auto-correlation within sample.

The A-scan with a sapphire ball lens has several additional peaks in contrast to the typical A-scan data which only has a single zero-delay peak. Among the additional peaks, the three fixed peaks are caused by auto-correlation between the references including fiber surface and highly reflective inner and outer surfaces of the ball lens. The distance between the two main peaks caused by the inner and outer surface has a larger value than the diameter of the ball lens (500 $\mu$ m) because the refractive index of the sapphire ball

lens is 1.77; thus, the distance looks like 885 $\mu\text{m}$ . Although these auto-correlated peaks have an undesirably high intensity, they can be removed by background subtraction. This is in part because their position and intensity are nearly constant. A greater issue is there are multiple sample signals in the A-scan due to the multiple references. Further complicating this is that multiple signals can overlap due to the close proximity of the two reference lines used to create the sample image. The distance between these two reference lines including fiber-tip and inner surface of the ball lens is determined by the lens equation to attain focusing and this was around 150 $\mu\text{m}$ . Thus, any sample which is thicker than this distance can induce an overlapping sample signal in the A-scan data. This problem can be critically problematic in a distal sensing application and it can also degrade the image quality of manually scanned OCT images.

According to Equation (52), the multiple and overlapped A-scans share common features. The signal can reasonably be decomposed into one basic signal with differing amplitudes and delays. We can then write the measured discrete signal by the sum of three template signals with different amplitudes, delays and noise. We can then describe this assumption as the following discrete equation:

$$y[n] = x[n] + a_1x[n - n_1] + a_2x[n - n_2] + s[n] \quad (53)$$

where  $x[n]$ ,  $y[n]$ , and  $s[n]$  are the desired original data, the measured A-scan data, and the noise data respectively. Additionally,  $n_1$  and  $n_2$  are the delay terms. Based on the above Equation (53), we can correct the distorted signal by converting it into a frequency domain[50].

$$Y[k] = X[k] + a_1X[k]e^{-\frac{j2\pi n_1k}{N}} + a_2X[k]e^{-\frac{j2\pi n_2k}{N}} + S[k] \quad (54)$$

$$x[n] = IFFT \left( \frac{Y[k] - S[k]}{(1 + a_1 e^{-\frac{j2\pi n_1 k}{N}} + a_2 e^{-\frac{j2\pi n_2 k}{N}})} \right) \quad (55)$$

where  $X[k]$ ,  $Y[k]$ ,  $S[k]$  are the results of discrete Fourier transform of  $x[n]$ ,  $y[n]$  and  $s[n]$ . The delay term in time domain is extracted into exponential term in frequency domain. Then, we can get  $x[n]$  by applying inverse Fourier transform. This Fourier-domain shift and sum (FSS) is easy to implement and only requires an initial reference measurement without sample to deduce the amplitude and delay of the multiple reference planes. Note that, if the noise term,  $S[k]$  is large, it has to be known to properly solve the equation. However, the noise terms can be also made small enough through A-scan averaging and background subtraction before applying the proposed methods which was demonstrated in this work. Also note that the coefficients  $a_1$  and  $a_2$  are normalized to the maximum A-scan peak and range between 0 and 1. To test this method, we simulate the setup shown in Figure 2.19(a) based on Equation (52). We used Gaussian function for coherence function,  $\gamma$  and assume that there are three reflectors in reference and ten reflectors in sample. The reflectance values for reference were determined based on the preliminary experiment result and the reflectance values for sample were chosen arbitrarily. The ground truth sample signal is shown in Figure 2.20(a) and random noise is added to the simulated signal as shown Figure 2.20(b). The dc component and auto-correlated signal between references can be removed by background subtraction as shown in Figure 2.20(c). Figure 2.20(d) shows the corrected signal after applying FSS method.

### 2.3.3.2 Single-reflector sample

The raw A-scan shown in Figure 2.21(a) is contaminated by multiple peaks coming from the highly reflective sapphire ball lens surfaces and their auto-correlation. This fixed

noise can be removed by background subtraction method as mentioned earlier and the result is shown in the blue graph, Figure 2.21(b). The noise inside of the sapphire ball lens is not completely removed due to the variability in local intensity caused by fiber polarization changes which are dependent on the motion of the optical fiber. However, this is not a critical problem as we know the position of the outer surface of ball lens in the A-scan and the noise within the outer surface can be removed. The three mirror signals are created by interfering with the reference beams coming from (1) outer ball lens surface, (2) inner ball lens surface and (3) fiber tip in order of position. After applying the proposed method, we can drive the corrected signal (red graph)

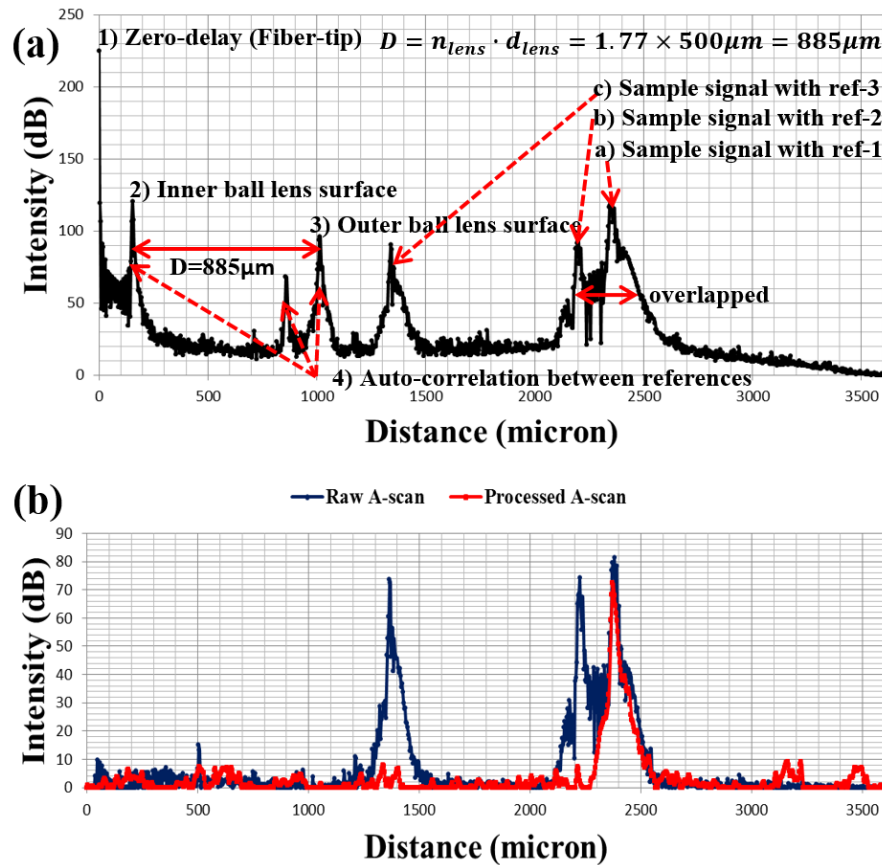


Figure 2.21. Mirror experiment result; (a) raw A-scan graph and (b) background subtracted A-scan graph (blue) and distortion corrected A-scan graph (red).

shown in Figure 2.21(b). It has the same shape as the first mirror signal, the blue graph. Signal correction works well here because the signal coming from the mirror is easily identified against the background noise.

#### *2.3.3.3 Complex-reflector sample*

As expected, in contrast to the mirror experiment, the cellophane tape experiment had more obstacles to overcome in that the signal was weaker and its shape was more complex. A particular difficulty was that the sample signal created by the reference beam, coming from the outer surface of the ball lens, was not strong enough to image the deeper structure in the sample. This was not the case with the other two signals; as a direct result, the first sample signal has different shape from the other sample signals. This is a critical violation of our assumption and it can induce substantial side effect when we deal with the signal in the frequency domain. Therefore, we need an alternative way to solve this issue.

As we know the relative distances between each sample in the A-scan data set, we can separate the A-scan into two regions once we locate the starting point of the first sample signal as shown in Figure 2.22(b). We used the same method to detect the sample surface that is described in our previous work[51]. Then, we added the modified sapphire ball lens diameter (885  $\mu\text{m}$ ) to the starting point of the sample signal in order to determine the first region. The second region is therefore in the remaining area. This process requires more processing time and computing power compared to the simple mirror case. In mirror case, we do not need to find the sample position. Then, we deal with these two regions separately. For example, when dealing with the first region, we set zero on the points in second region and vice versa. This alternative method improved the

SNR in the corrected data while decreasing the undesirable side effect due to the lossy signal in the first area. In the second region, our method decomposed the overlapped signal. Finally, we can get the corrected signal shown in red graph in Figure 2.22(b).

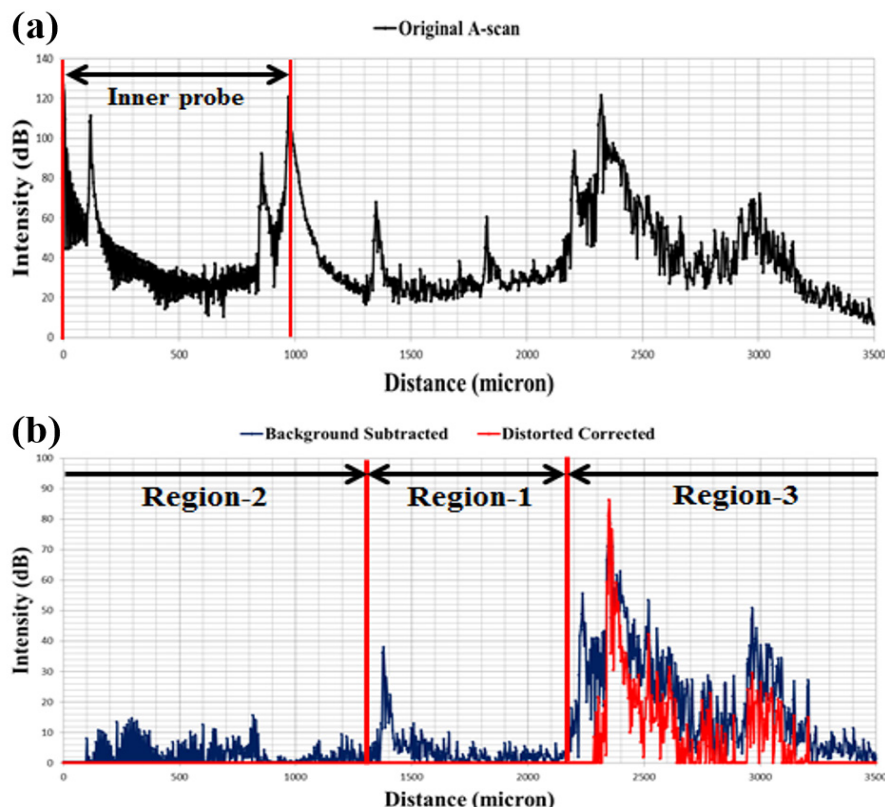


**Figure 2.22. Cellophane tape experiment result; (a) raw A-scan graph and (b) background subtracted A-scan graph (blue) and ghost corrected A-scan graph (red).**

A one-dimensional A-scan graph is not enough to verify whether the proposed method restores the features of the sample because it is hard to deduce the sample shape only observing 1D signal. As shown in Figure 2.23, we conducted manual scanning to get B-mode images of the cellophane tapes using the same method as reported in our prior work[33]. The raw B-mode image shown in Figure 2.23(a) has several bright horizontal lines induced by the sapphire ball lens. After background subtraction, the

image quality is improved by removing the fixed structural noise and lowering the DC-base line. The final restored image shows each individual layer of the cellophane tape that is similar to prior work.

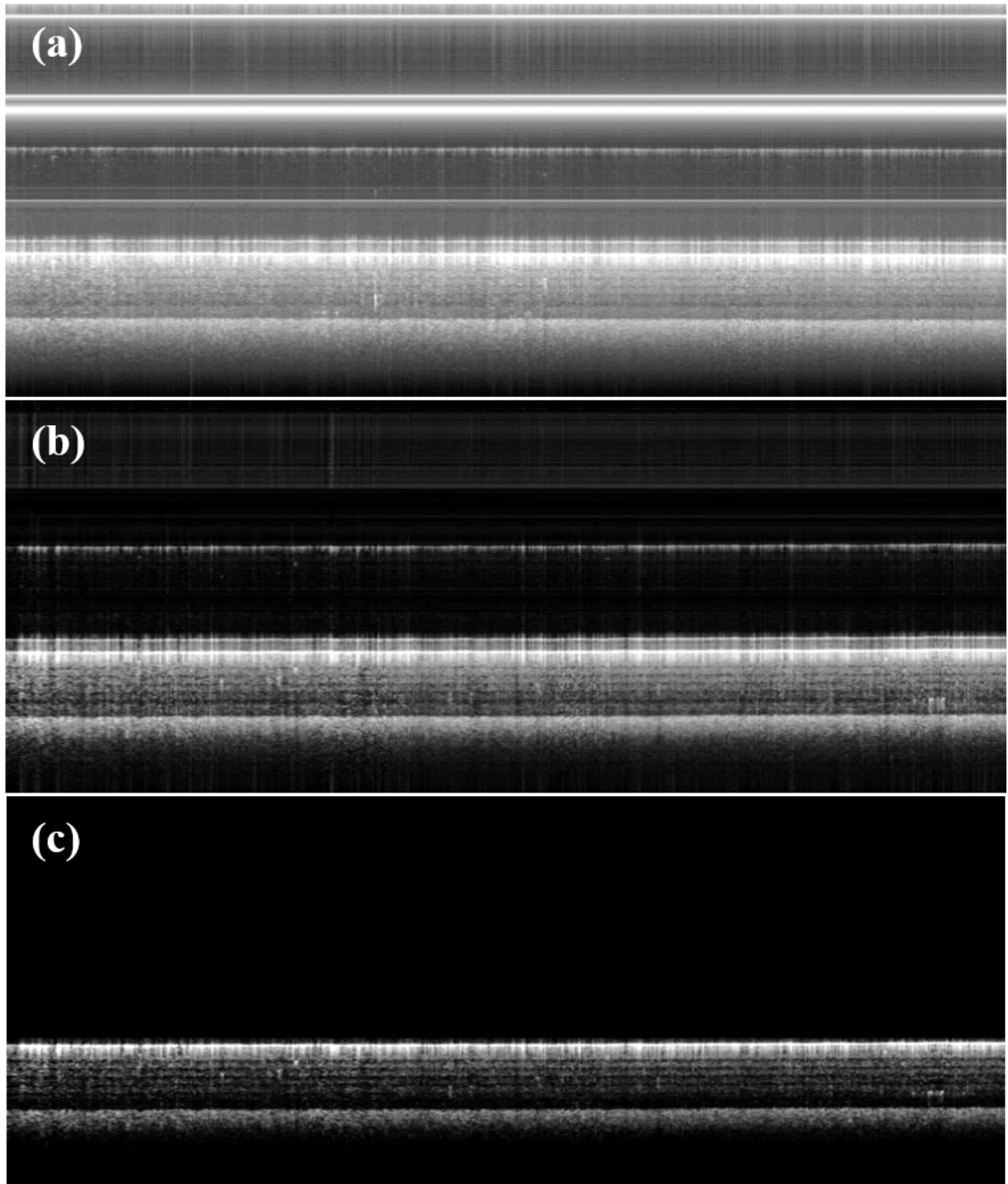


**Figure 2.23. Cellophane tape B-scan images; (a) raw, (b) background subtracted, and (c) ghost corrected B-scan images.**



## **CHAPTER 3 : ACCURATE REAL-TIME DEPTH CONTROL FOR CP-SSOCT DISTAL SENSOR BASED HANDHELD MICROSURGERY TOOLS**

### **3.1 Introduction**

Accurate and precise tool tip manipulation is imperative when performing microsurgery. A well-known barrier to precision in microsurgery is, physiological hand tremor, occurring predominating in the 6-12 Hz frequency domain with several hundred-micron-order amplitude[1], [2]. Retinal microsurgery is performed by passing microsurgical tools through trocars that provide access through the sclera. The trocar not only provides safe access into the eye but it also guides and stabilizes the surgical tools and acts as a remote center of motion. As a result, the lateral motion of the surgical tool is relatively well stabilized. In the case of axial motion, it is the surgeon that currently provides all of the guidance and control. The freehand tool movements are guided predominantly by visual information acquired from the surgeon's view in the operating microscope. Such tool tip visualization is limited in the axial direction by the ability to resolve small changes in position as well as by obstruction of the retinal surface by the tool shaft and tip. A variety of robot-assisted systems have been developed to actively overcome such a limitation and to achieve the surgical objectives while minimizing surgical risks[3]–[9]. Early in the evolution of this technology, it was the main point to develop a robot-assisted system with high accuracy and user-friendly operating manipulation[3]–[7]. Recently, diverse active tool-tips and sensors have been applied to the system to enhance its functionality [8], [9].

In parallel, Riviere, *et al.* has been developing a handheld microsurgical system that has differentiated itself from traditional robotic arm based systems[10]–[15]. The

handheld system operates independently without the assistance of external equipment such as a robotic arm by using its own embedded sensors and actuators. The advantages and disadvantages of the two assistance systems are numerous and are still being elucidated. However, advantages of the handheld systems include but are not limited to: lower cost, potential disposability, greater portability, ease of packaging, lower production costs, ease of use, adaptability, ease of customization and elimination of the large, costly cumbersome, robotic-assist systems that must now otherwise be clumsily implemented in the human clinical setting. A fundamental challenge of any handheld microsurgical tool is cancellation of hand tremor. A variety of motion sensors including accelerometer, magnetometer, position-sensitive detectors with infrared LED, etc. and small size of actuators such as piezo-electric motors and voice coils have been introduced. Moreover, a frequency analysis based tremor model has been previously built in accordance with the roughly sinusoidal nature of tremor[10].

Optical coherence tomography (OCT) has recently emerged as an effective imaging modality to support microsurgery due to its micron-order resolution and subsurface imaging capability[17]–[23]. Microscope mounted OCT systems now play a significant role in intraoperative visualization for forward viewing during actual surgical procedures. Our research group has established a potential role for a real-time OCT intraoperative guidance system with fast computational speed using a graphic processing unit (GPU) that is forward viewing and incorporated into the actual handheld tools[24]–[35]. Unlike typical OCT imaging, this application uses OCT as a distal sensor and its potential effectiveness for ocular microsurgery has been demonstrated[29]–[35]. The motion compensation that is based on the feedback from the OCT distal sensor effectively

suppresses undesired axial motion; as a result, the frequency region related to hand tremor is significantly decreased[34]. This result was applied to microsurgical tool development and improved performance has been demonstrated[35]. We have strategically chosen to incorporate common-path OCT (CP-OCT) into handheld microsurgery tools that are comparatively simple in design, relatively affordable and have the potential to be used as disposable surgical products.

An important difference between intraoperative OCT imaging and OCT distal-sensing is that in application, OCT distal sensing information is used to measure the physical distance of the sensor from the retinal surface. Moreover, in order to utilize OCT as an effective distal sensor, additional signal processing is required to identify and track the surface of a complex target tissue in a complex environment. While surface detection can be simplified to simple peak detection for tissues having a single layer or a dominant reflective surface; the retina has a complex multi-layered anatomy with multiple optically reflecting interfaces that serve as its optical signature. As in a complex surgical environment there is no guarantee that the strongest reflected signal always comes from the retinal surface or surface pathology, the characteristic reflective signal of the retina serves as an advantage that is utilized in the present signal processing algorithms. If this were not anticipated in advance, erroneous reflective data could result in consequential false distance information. Furthermore, real-time operation increases the complexity of the analysis by introducing motion, reduced time for making decisions, and a reduced amount of information available to make real time decisions. Evaluation of multi-layered structures requires edge detection analysis rather than peak detection to correctly find the surface[29]. Edge detection further enhances the surface detection method as the A-scan

signal from retina has multi-peak complexity. Therefore, we developed and incorporated a robust distance sensing method utilizing a shifted cross-correlation algorithm. It uses all of the signature information available in the A-scan to determine distance, rather than just the first peak; thus, the system produces robust distance data regardless of whether erroneous data is encountered.

In addition to achieve accurate and stable distal sensing, the handheld system must be designed to efficiently and effectively utilize the distance information to rapidly control the mechanical actuator for accurate and precise manipulation. It is important to appreciate that the time required for the OCT signal to be implemented into tool action requires heavy computational processing including averaging, Fourier transformation, surface detection, and that there is a communication delay that results in time gap

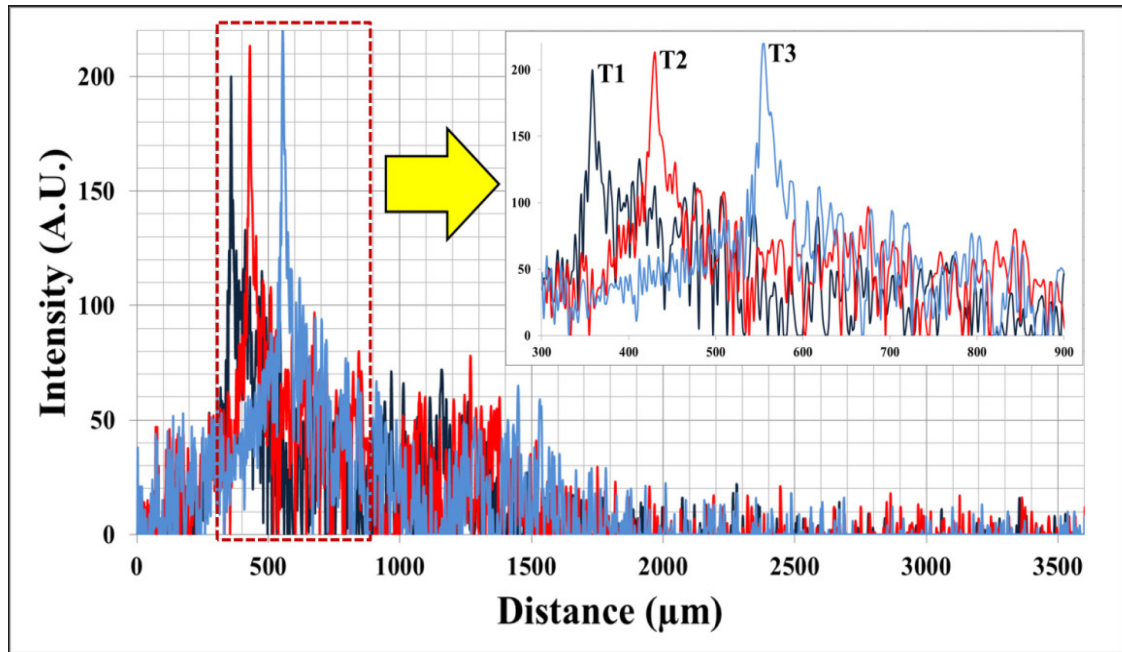


**Figure 3.1. Three consecutive A-scan data of 20-stacked layers of adherent cellophane tape near the DC line (multi-layered phantom sample); the upper right inserted graph is a partial magnified graph of area in dotted red square in lower entire graph.**

between sampling and compensating motion. Therefore, we utilized a GPU to reduce the processing time in the design of this system. Additionally, a predictor was developed to achieve more effective compensation. The predictor based on Kalman filter is used for the system latency compensation. A performance evaluation of this system is presented using a dry phantom consisting of 20 layers of cellophane tape. This is followed by an evaluation in a biologically relevant model, the ex-vivo bovine retina.

## 3.2 Background Theory

### 3.2.1 Spatially shifted cross-correlation

As shown in Figure 3.1, the series of A-scan data at T1, T2 and T3 show spatially shifted but mutually correlated waveforms. Because the A-scan data reflects the optical characteristics of the sample below the CP-OCT fiber sensor, it is natural that there is correlation between the spatially and temporally adjacent A-scan data. Thus, we can use this correlation to measure the distance variation. This method can be more effective than an edge detection algorithm to measure the distance variation when the A-scan data has a low signal-to-noise ratio and does not contain a dominant peak. Here is a brief overview of the spatially shifted cross-correlation scheme.

$$X_i * Y_{i+n} = \frac{\sum_i (X_i - m_X)(Y_{i+n} - m_Y)}{\sqrt{\sum_i (X_i - m_X)^2 \sum_i (Y_{i+n} - m_Y)^2}} = \rho_{-n} \quad (1)$$

where  $m_X$  and  $m_Y$  are the means of the sampled discrete A-scan data,  $X_i$  and  $Y_i$  and the subscript  $i$  and  $n$  are the index of A-scan data and shifted value respectively. The calculation of the cross-correlation between A-scan data generally requires a long computation time. Moreover, we need to compare the first A-scan data with every shifted

version of the next A-scan data. This is a prohibitively time consuming operation and is not practical for a real-time system; thus, we need to calculate the equation more efficiently[52]. The numerator of the equation (1) can be modified as

$$\rho_n^{num} = \sum_i X_i^1 Y_{n-i}^2 \quad (2)$$

where  $X_i^1 = X_i - m_X$ ,  $Y_i^1 = Y_i - m_Y$ , and  $Y_i^2 = Y_{-i}^1$ . Considering the numerator is the convolution of the anterior A-scan data  $X^1$  with the reversed shifting posterior A-scan data  $Y^2$ , this equation can efficiently be calculated based on the discrete correlation theorem with the fast Fourier transform  $F$ :

$$\rho_n^{num} = F^{-1}(F(X^1) * F(Y^2)) = F^{-1}(F(X^1) * F^*(Y^1)) \quad (3)$$

where we used the convolution theorem: time reversal of the signal in time domain is equivalent to the complex conjugate in the Fourier transform. Additionally, the denominator of equation (1) is constant regardless of the shifting variable  $n$ . By searching  $n$  that achieves maximum  $\rho$ , we can rapidly find the maximum matching point and distance variation between the two sequential A-scan data with two FFT (forward and inverse) instead of N-times direct cross-correlation computations.

### 3.2.2 Kalman filter

A faster system response is essential in decreasing involuntary hand tremor and to rapidly respond to target motion. The faster system response improves the accuracy of motion compensation over all frequency ranges[34]. However, there is an inevitable time delay between the distal measurement and subsequent compensation due to the processing time, and also the communication delay between heterogeneous devices such as the workstation and the motor driver. Such a time delay can produce outdated and incorrect

tool compensation signal especially in the case of a rapid target or hand movements. To avoid the potential risk of outdated compensation, a predictor is required. Here, we utilized a Kalman filter to adjust for the overall system latency. In this work, the Kalman filter was used as an algorithm that provides an efficient recursive solution to minimize the mean of the squared error[53]. Kalman filters have historically been extensively utilized in a broad area of tracking and assisted navigation systems[54]–[56]. The Kalman filter serves as an appropriate predictor in our case because it supports estimations of past, present, and future states even when the precise modeling of in our case tremor, is unknown. A portion of the unknown in this system e.g. results from potential encounters with a transiently obstructed imaging axis in the eye (such as blood); this would briefly present erroneous signal to the OCT distal sensor.

The Kalman filter consists of a set of mathematical equations. The equations can be divided into two main categories: 1) Prediction step and 2) Update step.

- Prediction step is

$$\hat{\mathbf{x}}_{t|t-1} = \mathbf{F}_t \hat{\mathbf{x}}_{t-1|t-1} + \mathbf{B}_t \mathbf{u}_t$$

$$\mathbf{P}_{t|t-1} = \mathbf{F}_t \mathbf{P}_{t-1|t-1} \mathbf{F}_t^T + \mathbf{Q}_t$$

- Update step is

$$\hat{\mathbf{x}}_{t|t} = \hat{\mathbf{x}}_{t|t-1} + \mathbf{K}_t (\mathbf{y}_t - \mathbf{H}_t \hat{\mathbf{x}}_{t|t-1})$$

$$\mathbf{K}_t = \mathbf{P}_{t|t-1} \mathbf{H}_t^T (\mathbf{H}_t \mathbf{P}_{t|t-1} \mathbf{H}_t^T + \mathbf{R}_t)^{-1}$$

$$\mathbf{P}_{t|t} = (\mathbf{I} - \mathbf{K}_t \mathbf{H}_t) \mathbf{P}_{t|t-1}$$

where  $\hat{\mathbf{x}}$  is an estimated state,  $\mathbf{y}$  is a measurement variable, and  $\mathbf{u}$  is an control variable.

The matrices  $\mathbf{F}$ ,  $\mathbf{B}$ ,  $\mathbf{P}$ ,  $\mathbf{Q}$ ,  $\mathbf{H}$ ,  $\mathbf{R}$ , and  $\mathbf{K}$  describe process equation, control variable mapping, error covariance, process noise covariance, measurement variable mapping, measurement

noise covariance, and Kalman gain, respectively. If the tool tip is assumed to move along a straight line in axial direction, 1D motion equation can be applied for the modelling of Kalman filter. Additionally, we assume that the acceleration is a random variable having Gaussian distribution with zero mean and variance  $\sigma^2$  when the tool tip gets to the target position. Then, we can derive the matrices.

$$\mathbf{x}_t = \begin{bmatrix} x_t \\ v_t \end{bmatrix} = \begin{bmatrix} 1 & \Delta t \\ 0 & 1 \end{bmatrix} \begin{bmatrix} x_{t-1} \\ v_{t-1} \end{bmatrix} + a_t \begin{bmatrix} \Delta t^2/2 \\ \Delta t \end{bmatrix} = \mathbf{F}_t \mathbf{x}_{t-1} + \mathbf{w}_t$$

$$\mathbf{y}_t = \begin{bmatrix} 1 & 0 \\ 0 & 0 \end{bmatrix} \mathbf{x}_t + \begin{bmatrix} r_t \\ 0 \end{bmatrix} = \mathbf{H}_t \mathbf{x}_t + \mathbf{b}_t$$

where  $x$ ,  $v$ ,  $a$ ,  $b$  are the position, velocity, acceleration of the tool tip, and observation noise. The process and measurement noise covariance are defined respectively as

$$\mathbf{Q}_t = \text{var}(\mathbf{w}_t) = E[\mathbf{w}_t \mathbf{w}_t^T] = \sigma^2 \begin{bmatrix} \Delta t^4/4 & \Delta t^3/2 \\ \Delta t^3/2 & \Delta t^2 \end{bmatrix}$$

$$\mathbf{R}_t = \text{var}(\mathbf{b}_t) = E[\mathbf{b}_t \mathbf{b}_t^T] = \begin{bmatrix} r_t^2 & 0 \\ 0 & 0 \end{bmatrix} \rightarrow \begin{bmatrix} r_t^2 & 0 \\ 0 & c_1 \end{bmatrix}$$

where  $c_1$  is small constant and the reason to change the form of  $\mathbf{R}_t$  is to prevent zero value determinant during Kalman gain calculation. When it comes to error covariance, we set

$$\mathbf{P}_0 = \begin{bmatrix} c_2 & 0 \\ 0 & c_2 \end{bmatrix}$$

where  $c_2$  is suitably large constant because we do not know the starting position. Because our system actively compensates the deviation distance from the target position, we can set the control variable and its mapping matrix as

$$\mathbf{B}_t \mathbf{u}_t = \begin{bmatrix} -1 & 1 \\ 0 & 0 \end{bmatrix} \begin{bmatrix} y \\ y_{tgt} \end{bmatrix}$$

where  $y$  is the measured position and  $y_{tgt}$  is the target position.



### 3.3 Materials and Methods

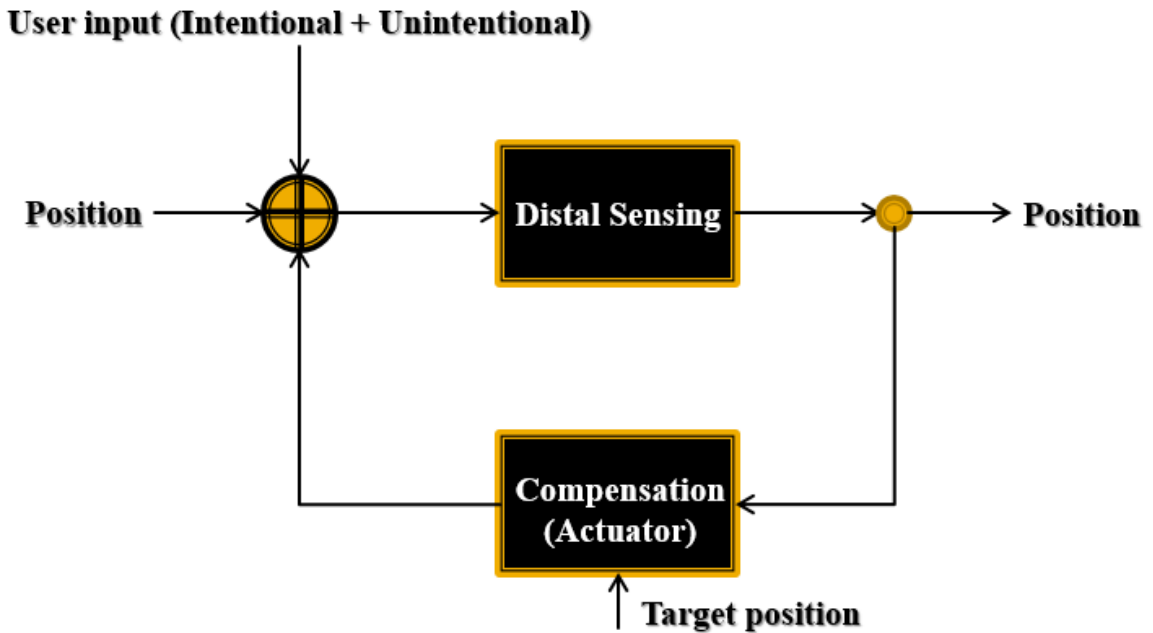


**Figure 3.2. The basic concept of Sensorized Micromanipulation Aided Robotic-surgery Tool (SMART) system based on closed loop feedback system**

The basic concept of our Sensorized Micromanipulation Aided Robotic-surgery Tool (SMART) system is depicted in Figure 3.2. The system is basically closed loop feedback system, which continuously compensates the erroneous distance deviated from the desired target position based on the position detection. For this purpose, there are two main components: 1) distal sensor and 2) linear actuator. Depending on the specification of the two components, the performance of the entire system is determined. In particular, implementing an accurate and stable distal sensor is critical not to make the system diverging.

### 3.3.1 System configuration

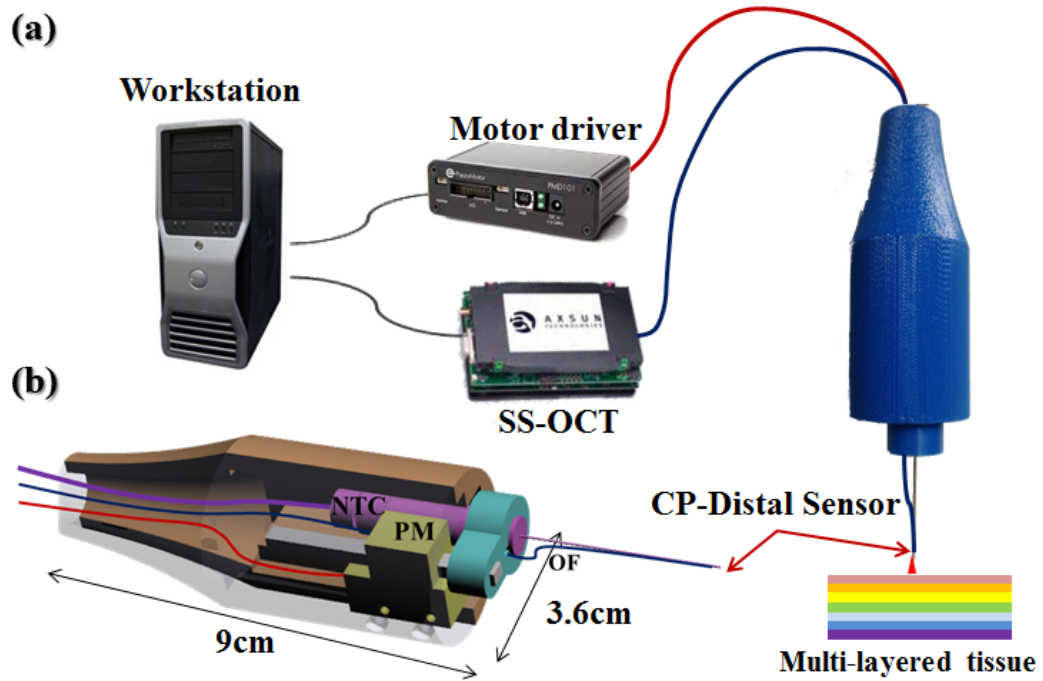


**Figure 3.3. a) Active depth targeting and locking microsurgery system, b) CAD cross-sectional image of handheld tool (NTC: needle-to-tube connector, PM: piezo-motor, OF: optical fiber)**

The handheld CP-OCT distal sensor system consists of three main modules: SS-OCT, a workstation, and a piezoelectric linear motor driven handheld tool as shown in Figure 3.3(a). Figure 3.3(b) shows the CAD design of the handheld tool. The OCT system consists of a swept source OEM engine (AXSUN, central wavelength  $\lambda_0$ : 1060nm, sweeping rate: 100kHz, scan range: 3.7mm in air), a photo-detector and a digitizer with a sampling rate of up to 500MSPS with 12-bit resolution, a Camera Link DAQ Board, and a Camera Link frame grabber (PCIe-1433, National Instruments). The workstation (Precision T7500, Dell) with general-purpose computing on graphics processing units (GPGPU, GeForce GTX590, Nvidia) processes the sampled spectral data and control the linear motor. The parallel processing (CUDA, Nvidia) of the GPGPU can reduce the

processing time considerably in FFT, background noise subtraction and averaging, which is mainly responsible for the processing delay[24], [25]. The handheld tool uses a piezoelectric linear motor (LEGS-LL1011A, PiezoMotor) which has a maximum speed of 15 mm/s, maximum stroke of 80 mm, stall force of 6.5 N, and a resolution of less than 1 nm. The communication protocol between the motor driver and the workstation is RS232 and the protocol is implemented virtually on top of USB protocol. For this reason, it is important to configure the USB settings suitable for the short and frequent message transmission to minimize the communication delay, which is another factor of the system delay. Specifically, buffer size and timeout for transmission are the parameters that need to be adjusted. The buffer size was fitted for the most frequent message size and the timeout was set at the minimum value. The housing of the handheld tool as shown in Fig

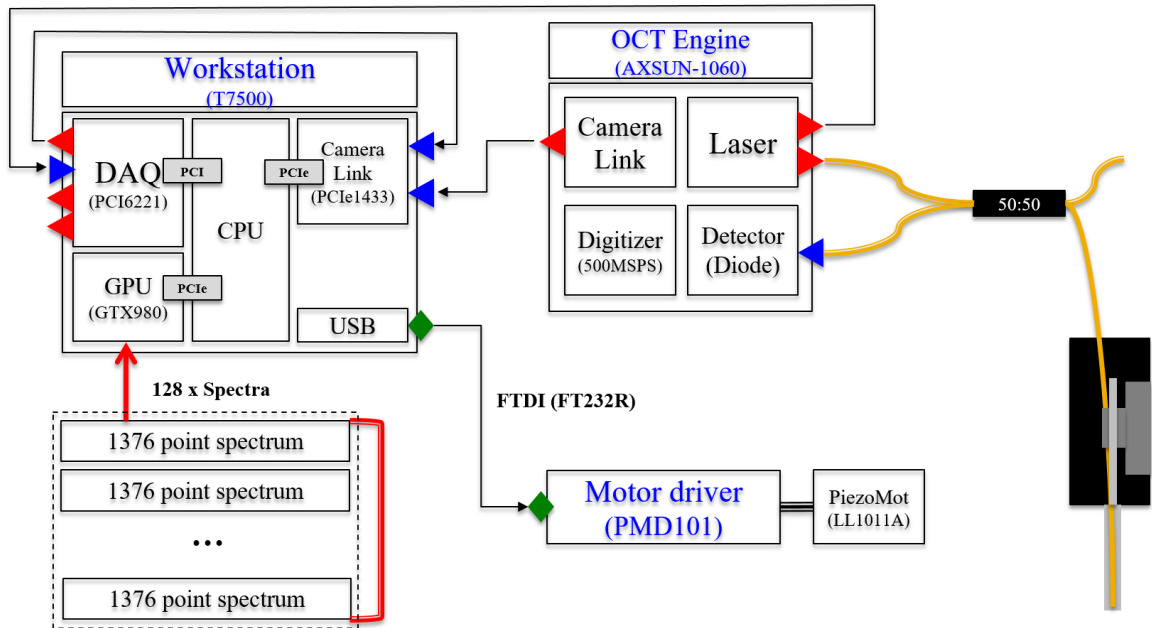


**Figure 3.4. System connection for the synchronization among the core components: OCT engine, workstation, and motor driver.**

2(b) was made by a 3D printing machine. The dimensions of the handheld tool are 3.6 cm diameter and 9 cm length. The optical fiber for distal sensing is attached to the end of the needle and the needle-to-tube connector (RN Coupler-p/n, Hamilton) is mounted into the handheld tool to give a greater load to the linear motor similar to realistic application.

In terms of the synchronization among the system components including workstation, OCT engine, and actuator, SS-OCT has stricter synchronization requirement than SD-OCT because SS-OCT uses time-encoded sweeping laser source. As mentioned in chapter 2, SS-OCT provides trigger clock signal or k-clock in order to synchronize with other devices such as digitizer and another clock-generation device like NI-DAQ card. Because AXSUN-1060 OCT engine already embeds sweeping laser, diode detector, digitizer, and camera link system, however, the synchronization between OCT engine and workstation can be simplified to the communication between the both of camera links in OCT engine and workstation as shown in Figure 3.4.

### 3.3.2 *The control algorithm*

The sampled spectral data is sequentially processed in the following three steps as shown in Figure 3.5(c). The first step is to transform the spectral data to A-scan data similar to that in typical OCT imaging. Specifically, 128 spectra each consisting of 1376 data points are transmitted from the frame grabber in every 1.28 ms. The system response or sampling rate should be determined based on the computational performance. Comparing to the previous work in our group[34], the system response can be improved from 500 Hz to 780 Hz with the help of parallel processing with GPU. The total computational and communication delay is 650  $\mu$ s on average and we reserved the other half of time (=630  $\mu$ s) for variable system performance. Four sequential spectra are averaged to increase the

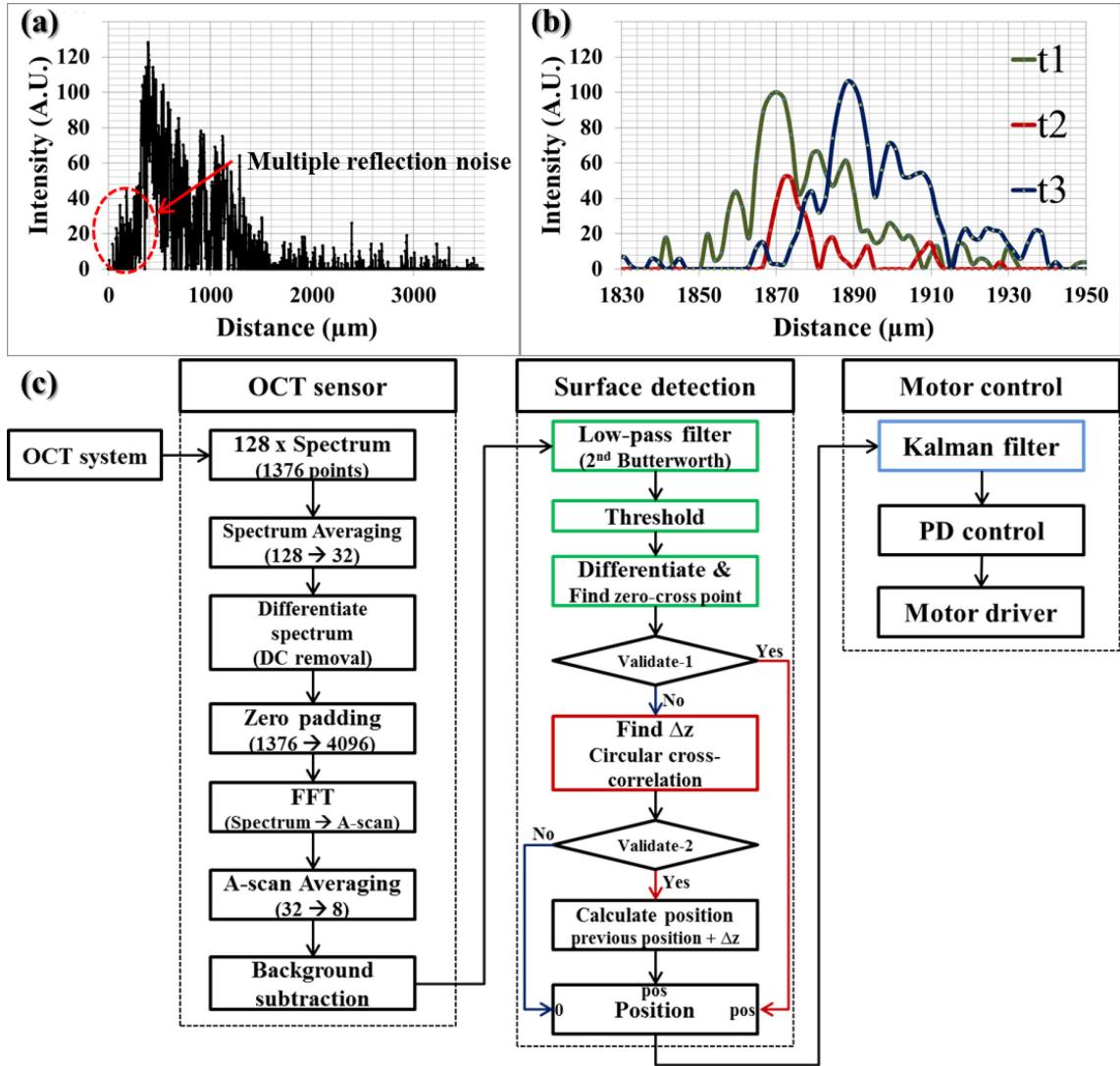


**Figure 3.5.** a) A-scan data of *ex-vivo* open bovine retina, b) three consecutive A-scan data of stacked layers of adherent cellophane tape, c) data processing flowchart consisting of 1) OCT data process, 2) Surface detection, and 3) Motor control.

signal-to-noise ratio (SNR) followed by a discrete differentiation to remove the DC component in frequency domain. Then, zero padding is applied to increase the data points of the averaged spectra from 1376 to 4096 before fast Fourier transform (FFT). After the transformation, additional averaging and background subtraction are conducted on the A-scan data. As a result, we have 8 A-scan data and each A-scan data has 2048 data points

that covers a 3686.4  $\mu\text{m}$  axial distance in the air (1.8  $\mu\text{m}$  between each data point). Note that it is important to remove the background noise in A-scan data for the subsequent A-scan matching process using shifted cross-correlation in order to find the distance variations since this process is susceptible to the stationary background noise. The final processed A-scan data are used for the next step, the surface detection.

As shown in Figure. 3.6, peak detection is not suitable for the surface detection in a sample with a complex multi-layered structure in contrast to the sample having single dominant reflector. Alternatively, an edge detection scheme can be used. For the edge detection, first, 2<sup>nd</sup> order Butterworth low-pass filtering is applied to extract the envelope shape of the A-scan data because the A-scan data contains multiple local maxima and minima that hinder the edge detection. Then, a thresholding is applied to discriminate the signal from the noise. The noise level without sample (=background noise) determines the minimum thresholding value. Whereas, the maximum value is set to be adaptive to the maximum intensity of the current signal because the noise level, as indicated by the area with red dotted circle in Figure 3.5(a) between the sample and the zero delay line, increases as the fiber sensor tip approaches the sample. This is because multiple reflections in close proximity induce stronger interference; as a result, the noise level also increases. Next, the first zero-cross point is identified to find the surface after a discrete differentiation.

Two processes validate the calculated position: checking the value itself (if the position is zero, the detection is failed) and comparing it with the previous position. According to the failure of position detection, there are two possible cases. If the intensity of A-scan data is smaller than the threshold value, the surface detection is considered to

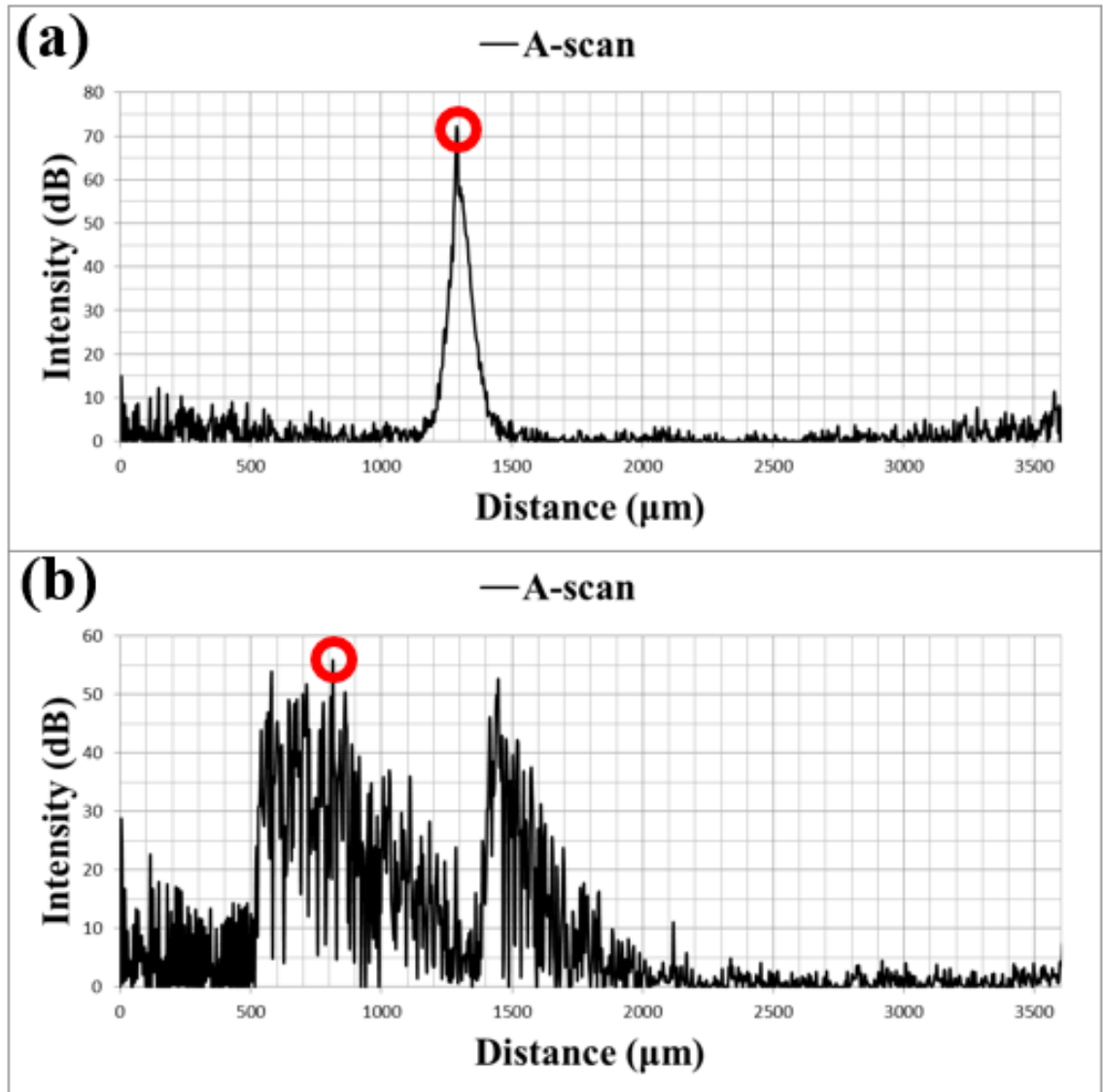


**Figure 3.6.** Two A-scan examples measured in the samples having a) simple one dominant reflector and b) complex multiple reflectors typically shown in bio-sample.

be failed even though the A-scan data still has sufficient features to find the surface as shown in Figure 3.5(b). In another case, we see that the distance variation between the two consecutive positions has an abnormally large value as compared to the presumed maximum value. This is mainly because the predominant reflective layer within a sample

makes the adaptive thresholding too high so that it erases the surface peak as well as the background noise. To make up for the limitations of simple edge detection, we used a spatially shifted cross-correlation as described in the previous section. As shown in Figure 3.5(b), the A-scan data at t2 has similar features as the A-scan data at t1 and t3 in spite of its low intensity. In this case, spatially shifted cross-correlation can find the matching point and distance variation as a result. The result is validated based on the normalized cross-correlation value, which reflects how the two A-scan data look similar. In the real implementation, we set 60% as a threshold.

Finally, the calculated position data is transmitted to the third step, motor control module. Instead of using the position data directly to control the motor, a Kalman filter is applied as a predictor for more accurate motion compensation. The predictor is needed to make up for the time delay between the distal measurement and the actuator movement due to the processing and communication delay, which is 650  $\mu$ s on average in the implemented system. The previous prediction value is alternatively used as an input data when position detection is failed in the previous step as long as the number of consecutive failure is smaller than the predetermined value. This predicted position is then used to calculate the actual compensating length through modified proportional-derivative (PD) control. Typical proportional-integral-derivative (PID) control is not appropriate because the distance between sample surface and tool tip is continuously varying. At the same time, the compensating length should be calculated in accordance with the separate length between target and tool tip and current speed of the tool. The parameters of PD control are modified adaptively based on the current trend of the process[57]. Finally, the compensating value is transmitted to the motor driver.



### 3.3.3 Data flow in CPU and GPU

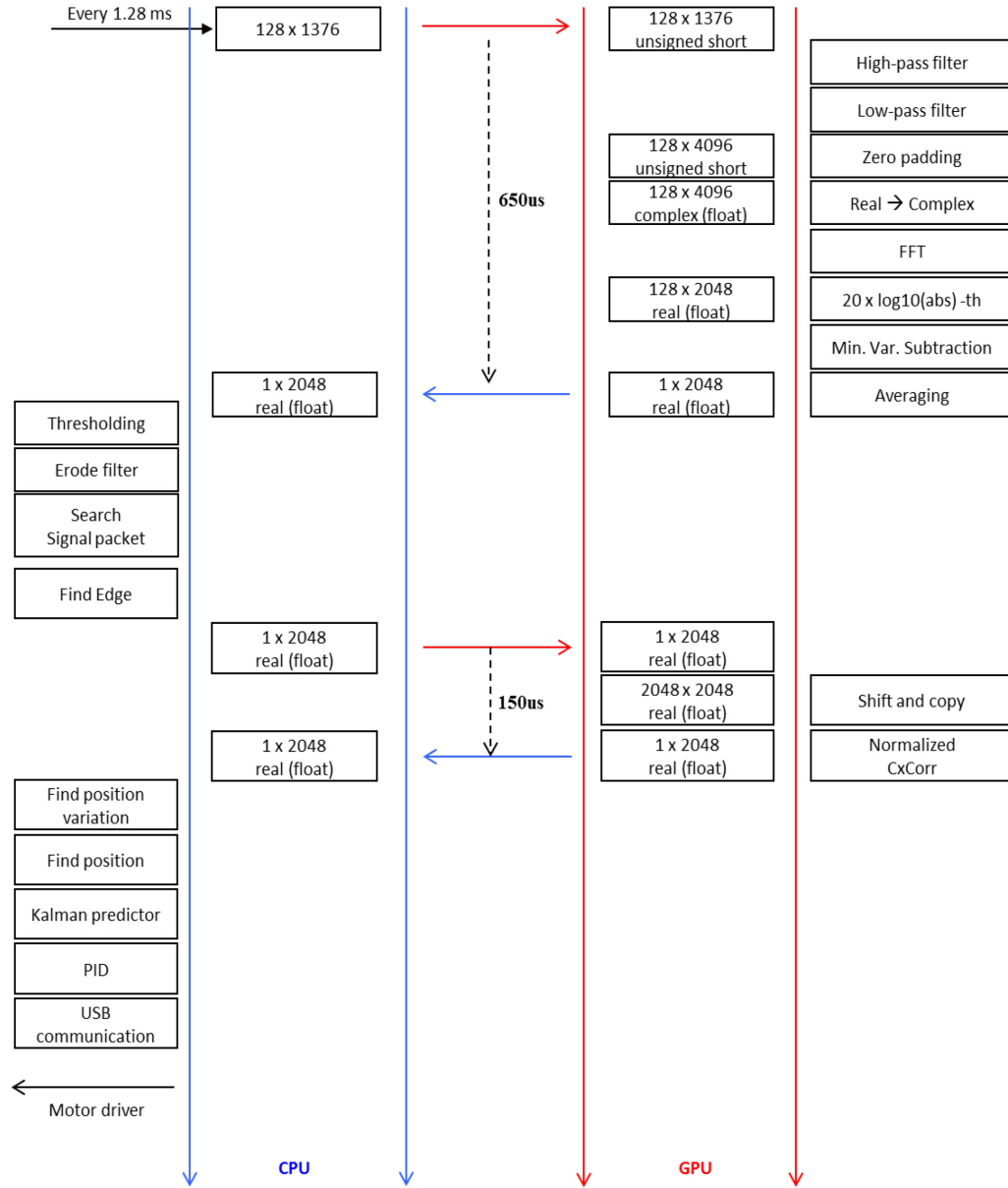


**Figure 3.7. Data flow between CPU and GPU.**

For the real-time OCT signal processing, our system incorporates GPU processor for parallel computation. As described in previous section, the OCT engine delivers 128 spectrum data consisting of 1376 data points in every 1.28 ms. The longest delay happens

during the data transfer between CPU and GPU because there is actual data transmission through PCIe connection. Thus, we need to minimize the data size of communication. At this point, we need to think about the fact that the 128 data arrays have the same data structure and they are independent from each other during a series of signal processing. This is the main point how we can decrease the computation time by applying GPU based parallel processing as shown in Figure 3.7. In the next step for the edge detection, the process is serialized that means each process is based on the result of previous process. In condition, CPU is more appropriate for the computation except the process to calculate the shifted cross-correlation. The computation for shifted cross-correlation uses one data set but all the shifted version of the data set; thus, the delay of data transfer between CPU and GPU can be ignore considering that the huge processing time reduction for calculating cross-correlation.

### **3.4 Experimental results and discussion**

#### *3.4.1 Phantom experiment*

Two different experiments were conducted to evaluate the performance of the proposed distal sensing algorithm with the dry phantom in each case consisting of 20-stacked layers of adhesive cellophane tape. The phantom was set on the table at a 10-degree tilt angle to better represent the non-perpendicular orientation of instruments in application. First, we tested the effectiveness of the edge detection with the shifted cross-correlation method by comparing it with the edge detection only. The experiment was conducted with a random delay for a blind test and the shifted cross-correlation method was repeatedly turned on and off in every 1.28s. The offset value ( $=921.6\mu\text{m}$ ) was

intentionally added to the data from the test using the edge detection with shifted cross-correlation (yellow region) to easily distinguish these two different cases as shown in Figure 3.8(a). The dark red vertical lines in Figure 3.8(a) indicates detection failure and

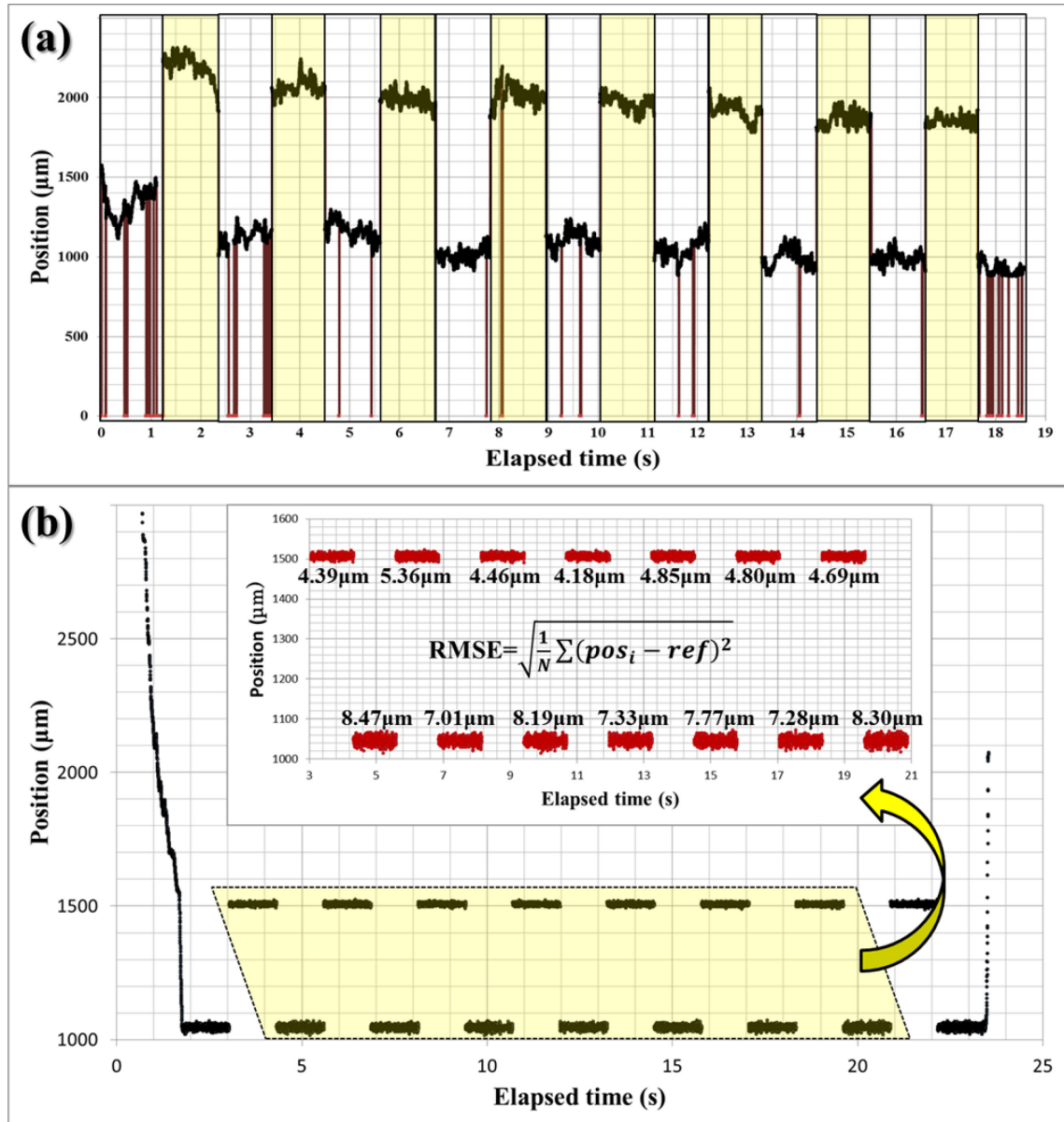


**Figure 3.8. Dry phantom experiment: a) evaluation test for the surface detection algorithm with the auxiliary shifted cross-correlation in non-depth-locking freehand, b) evaluation test for the depth-locking with the predictor based on Kalman filter: the upper inserted graph is a magnified graph of area in dotted yellow trapezoid in the entire graph.**

the number of vertical lines or the failure rate in the yellow region is much lower than in the other region (white region). In fact, only a single case of failure at around 8.1 second was observed over the 20-second observation when the shifted cross-correlation method was used. The failure rate without the shifted cross-correlation method was 28 incidents/s and 0.3 incidents/s with the shifted cross-correlation method. These results clearly indicate that the addition of the shifted cross-correlation methodology can greatly improve the stability of the OCT distal sensor.

In the second experiment, we evaluate the effectiveness of the predictor based on a Kalman filter. During the experiment, the predictor method was also repeatedly turned on and off in each 1.28s increment. The offset value ( $=460.8\mu\text{m}$ ) was added to the data with a predictor to easily differentiate the result from the data without the predictor. In fourteen consecutive trials were conducted in total to maintain a fixed position and the results are shown in Figure 3.8(b). The upper graph in Figure 3.8(b) is a magnified view of the area in the dotted yellow trapezoid. The magnified view includes the RMSE for each trial. The average RMSE without the predictor is  $7.76\mu\text{m}$  and the average RMSE with the predictor is  $4.68\mu\text{m}$ . This result shows that the predictor operated effectively to make up for the processing time delay by deducing a more probable position when the linear motor actually operated.

#### 3.4.2 Bovine retina experiment

To evaluate the performance of the overall compensation system, we used an *ex-vivo* bovine retina model. Figure 3.9(a) shows the *ex-vivo* bovine retina after removing cornea, lens, and vitreous humor. The experiment was conducted on the same day as death thereby preserving the multi-layered structure of bovine retina, which gradually degrades

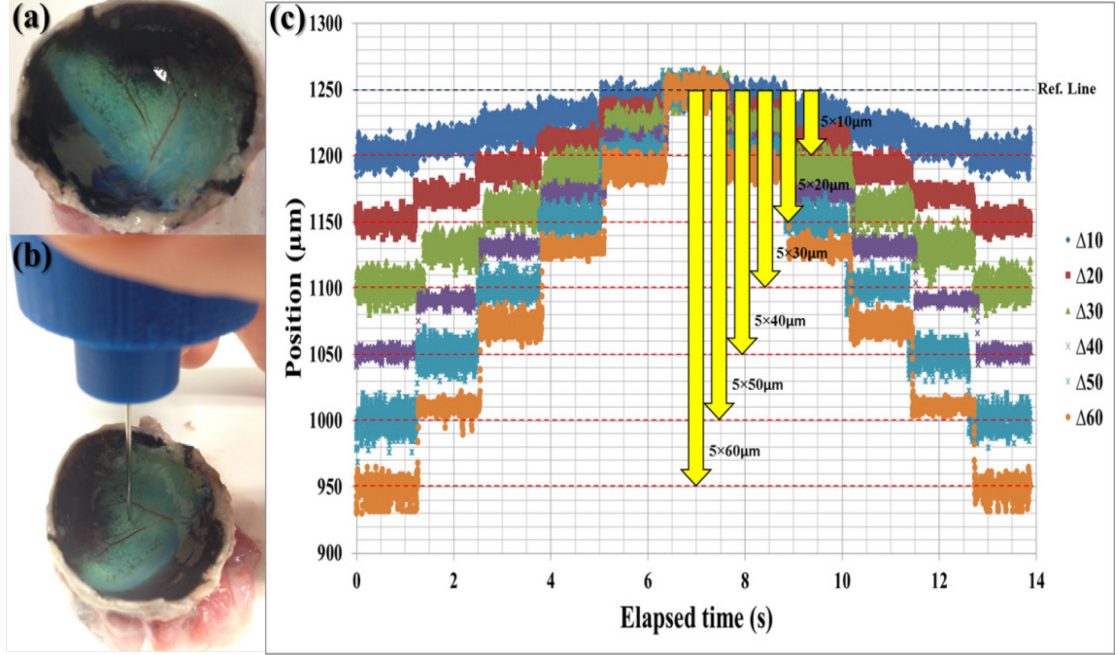


**Figure 3.9. Bovine retina experiment: a) bovine retina after removing cornea, lens, and vitreous humor, b) snapshot of the experiment, c) depth targeting and locking experiment result with six different jumping distance from 10  $\mu\text{m}$  to 60  $\mu\text{m}$**

**Table 1. Optical Constants of Thin Films of Materials [ $\mu\text{m}$ ]**

	$\Delta 10$	$\Delta 20$	$\Delta 30$	$\Delta 40$	$\Delta 50$	$\Delta 60$
1	5.264	4.562	6.750	2.944	8.129	5.939
2	5.080	3.774	6.222	3.108	7.404	3.950
3	6.473	4.297	7.161	3.038	5.447	5.488
4	4.683	3.416	5.494	3.376	5.630	3.141
5	5.233	5.017	6.114	3.891	5.061	4.823
6	6.286	4.007	5.838	3.170	5.761	4.981
7	6.367	4.078	6.427	2.600	5.513	4.344
8	6.830	3.938	6.377	2.887	5.642	3.937
9	5.148	4.187	6.685	3.181	5.275	5.118
10	5.259	3.200	7.342	2.104	6.826	2.941
11	6.063	4.255	6.603	2.982	7.277	5.388

beginning after the first few hours of the post mortem. We designed the experiment to evaluate the performance of the system in terms of dynamic depth targeting and precise depth locking by repeatedly holding and changing the position in a prescribed manner. Specifically, the user carried the tool tip to the surface of retina as shown in Figure 3.9(b)

and the experiment starts when the tool tip reached the predetermined offset distance. The offset distances were predetermined to be six different jumping distances from 10 $\mu$ m to 60 $\mu$ m in order to maintain the same reference line. Moreover, the system was programmed to hold its current position for 1.28s (=1000 data points) to evaluate its depth-locking performance.

As shown in Figure 3.9(c), the system consistently adjusted the needle position in accordance with the predetermined jumping distance. In total, there were 60 depth-targeting and 66 depth-locking trials. Table 1 shows the specific RMSE values of each depth-locking trial in Figure 3.9(c). Figure 3.10 shows the average RMSE and standard deviation error bar with different jumping distance. The total average, maximum, and minimum of RMSE were 4.996  $\mu$ m, 8.129  $\mu$ m and 2.104  $\mu$ m respectively. The average

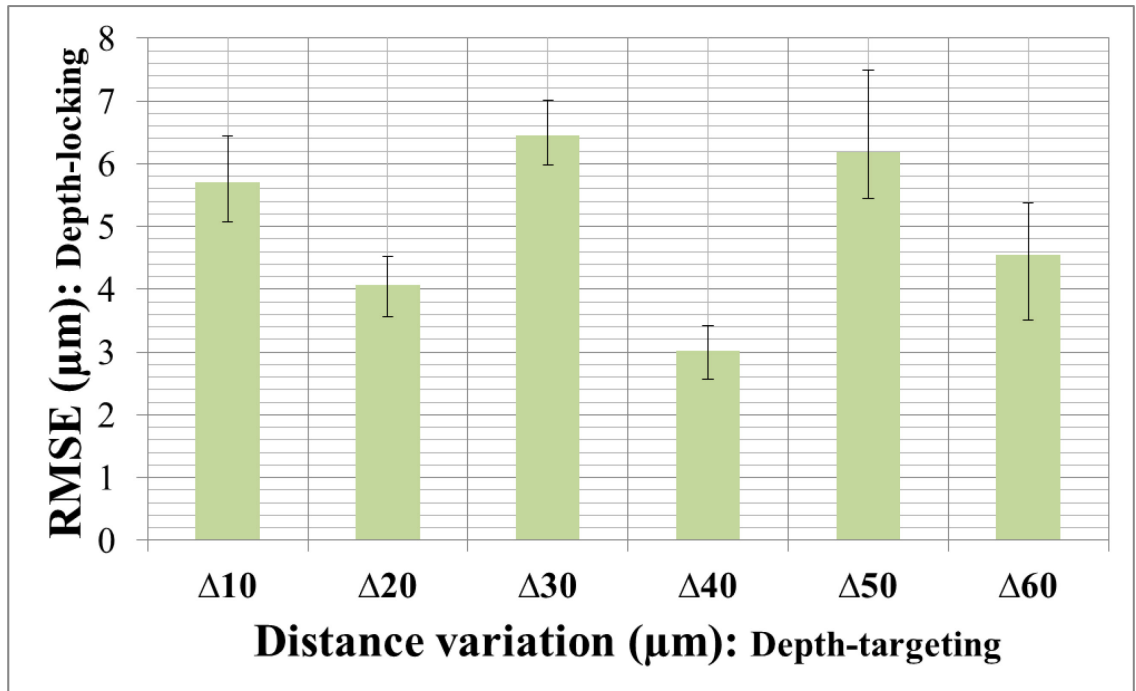


**Figure 3.10.** Averages of RMSE with standard deviation error bar of the bovine retina experiment. The x-axis labels mean jumping distance and the y-axis indicates the means and standard deviations of the measurement specified in Table 1.

depth locking RMSE, 4.996  $\mu\text{m}$ , is smaller than 1/5 thickness of inner nuclear layer (INL),  $27 \pm 8 \mu\text{m}$  (Mean  $\pm$  Standard deviation), which is thinnest layer in human retina[58], [59]. Even worst RMSE, 8.129  $\mu\text{m}$ , is about 1/3 of INL thickness. These figures demonstrate the potential for this microsurgery system to be used for targeting and delivering a therapeutic agent into specific layer of the human retina.

### **3.5 Conclusion**

In conclusion, we have demonstrated a novel motion compensation control method that allows accurate depth targeting and precise depth locking with micron-order RMSE. We have evaluated the technology in a dry phantom and in biological specimens possessing a multi-layered tissue structure. Future work will focus on implementing the potential for precise tool tip actions that this technology enables. The retina is an ideal model in which to assess the ability to e.g. use a derivative technology such as a high precision micro-injector system to accurately place potentially therapeutic agents in previously inaccessible retinal layers and micro-forceps system to precisely peel the epithelial layer of retina.

## **CHAPTER 4 : HANDHELD MOTION-GUIDED MICRO-FORCEPS FOR EPIRETINAL MEMBRANECTOMY BASED ON CP-SSOCT**

### **4.1 Introduction**

In retinal microsurgery, various vitreoretinal procedures routinely require accurate manipulation of the surgical instrument close to the retina surface while trying to avoid severe complications. One such delicate operation is epiretinal membrane peeling (membranectomy), which is among the most commonly performed vitrectomy-based procedures. It is used to delaminate a very thin (micron scale) fibrous membrane adherent to the retinal surface, using either a pick or preferably a micro-forceps tool (Figure 4.1a). Specifically, the internal limiting membrane (ILM), which is a very thin and transparent membrane on the surface of the retina, participates in the pathogenesis of vitreoretinal interface diseases such as macular hole (MH) and macular pucker (MP) as well as other maculopathies[58]–[60]. ILM peeling is a challenging procedure due to its single micron scale thickness and its transparency. Typically, the ILM is stained using dyes such as indocyanine green (ICG) in order to improve the visibility. However, there have been studies reporting toxicity of ICG to the retinal pigment epithelium (RPE) and neurosensory retina[61]. Besides the visibility issue, the procedure is still challenging to master due to involuntary patient movement and the physiological hand tremor of the surgeon, which is typically within the 6-12 Hz frequency range with several hundred microns of amplitude[1]. Considering that the thickness of epiretinal membrane is below 100 microns and the total retina thickness is about 250 microns, both the surgeon's hand tremor and patient motion have significant potential to cause retinal injury.



During membranectomy microsurgery, surgeons need to first insert the surgical tool tip to a desired depth for grasping and lifting the membrane edge without harming the underlying retina. To grasp, the standard disposable micro-forceps from Alcon, Inc. (Fort Worth, TX) (Figure 4.1b) requires squeezing of the tool handle for tip actuation. Because of the large squeezing motion and the associated forces, the tool apex position is less stable during forceps' jaw closure. After grasping the membrane, it is carefully delaminated from the retinal surface by deliberately moving the tool very slowly (typically 0.1-0.5 mm/s) in strategic delaminating directions. During both steps, the surgeon is dependent upon visualization through a stereomicroscope, with depth perception limited by the ability to resolve on the micron scale in the axial axis; and with potential obstruction of the surgical contact site by the tool shaft and functional tip. Optical coherence tomography (OCT), with its highly accurate depth resolved imaging capability, serves to overcome these limitations in this setting[17]–[19], [22], [23], [62]. Our research group has been pursuing an axial motion sensing and guidance approach that utilizes a swept source OCT (SSOCT) as a distal sensor. In our approach, common-path SSOCT (CP-SSOCT) has been strategically adopted because it is simple in design, inexpensive and has the potential to in part, be incorporated in disposable surgical products[30], [63], [64]. In order to develop a real-time OCT intraoperative guidance system, we employed a parallel programming technique that uses a graphic processing unit (GPU) for fast computational speed and incorporated it into the microsurgical tool system[24]. This distal sensing application is distinguished from the typical OCT “B-scan” imaging application in that our distal sensing system measures a distance value by acquiring A-scan data, with its attendant complexity[29], [31]–[35], [51]. The OCT data in our

application is subsequently transformed to distance information rather than morphological information, and is directly utilized for motion control in real-time. In this regard, our depth-guided micro-forceps embedding OCT distal sensor is the extension of the handheld instruments[11], [13], [14], [16], [33]–[35], [51], [65]–[67]; therefore, it is differentiated from the robotic arm based guidance systems[3], [6], [9], [68] including the recent work that utilizes a micro-forceps and OCT B-scan images for guidance[9].

Integrating CP-SSOCT feedback with a micro-forceps via an intuitive control system can effectively bring the tip of the forceps at the desired depth and maintain it at that position until successful grasping, regardless of involuntary user or patient motion. Based on the approach shown in Figure 4.2, our group previously developed a “SMART” micro-forceps and demonstrated the feasibility of this concept in stabilizing tool motion for safer grasping[35]. However, this previous tool posed limitations due to its mechanical design. Preserving the squeezing mechanism on the conventional micro-forceps, the inner wire providing the grasping action in this design interfered with the operation of the motor compensating the involuntary motion. This design approach posed a potential risk of conflict between these two actions. Ideally, the degrees of freedom required for grasping and depth guidance actions need to be independent of each other. Therefore, this study builds on and substantially advances our prior work by strategically separating these two functions via two independent actuators[65]. One of the actuators provides the active motion guidance that is controlled by the OCT guidance system while the other provides the grasping functionality controlled by the user. The standard micro-forceps are actuated by squeezing the tool handle as shown in Figure 4.1b, which may induce significant erroneous motion of the tool tip while grasping. Our present design

replaces this actuation mechanism with a linear motor interfaced with a touch sensor. This new motorized architecture removes the squeezing motion from the tool handle and thus substantially reduces the motion artifact at the tool tip during grasping. Furthermore, the integrated CP-SSOCT feedback is used to actively guide and stabilize the tool tip relative to the tissue by compensating any residual motion due to forceps actuation, involuntary motion of the operator such as physiological hand tremor, and patient movement. In order to evaluate the performance of our tool, we compared the motion at the tool tip during grasping considering 3 cases: (1) using standard manual micro-forceps, (2) using our motorized micro-forceps without active OCT guidance, and (3) using our motorized micro-forceps with active OCT guidance.

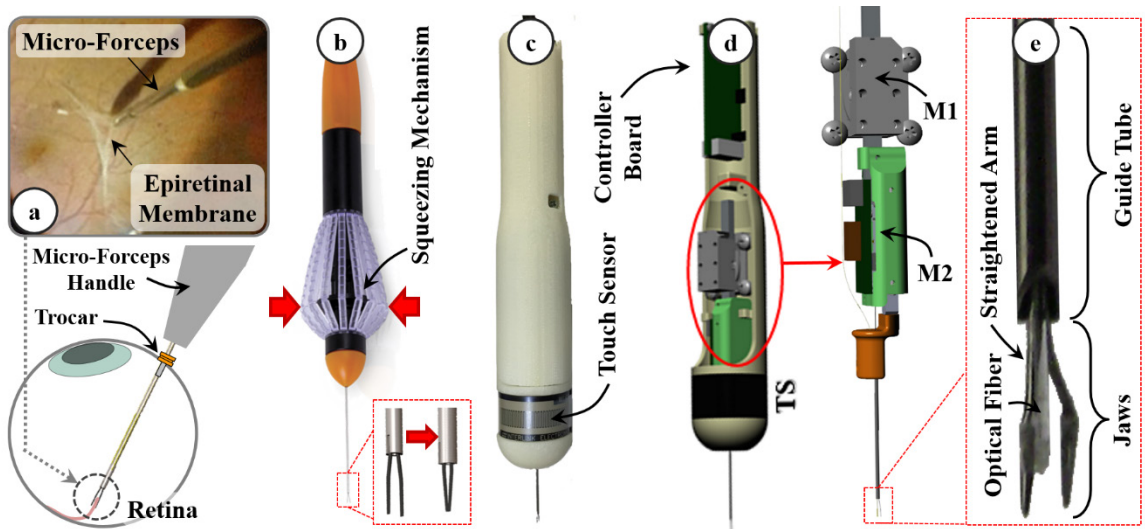


**Figure 4.1. (a) Epiretinal membranectomy: after grasping the membrane edge with a micro-forceps the membrane is pulled away from the retina surface slowly; (b) The standard 23 Gauge disposable micro-forceps (Alcon, USA); Our motorized active motion-guided micro-forceps: (b) fabricated prototype, (c) inner structure with two motors (M1 and M2) and the fiber-optic sensor (SSOCT) attached to the straightened arm of the jaws.**

## 4.2 Materials and Methods

Our motion-guided micro-forceps (MGMF) system consists of three main modules: (1) fiber-optic OCT module (distal sensor), (2) micro-forceps handpiece module (operating hardware), and (3) workstation (computing and control).

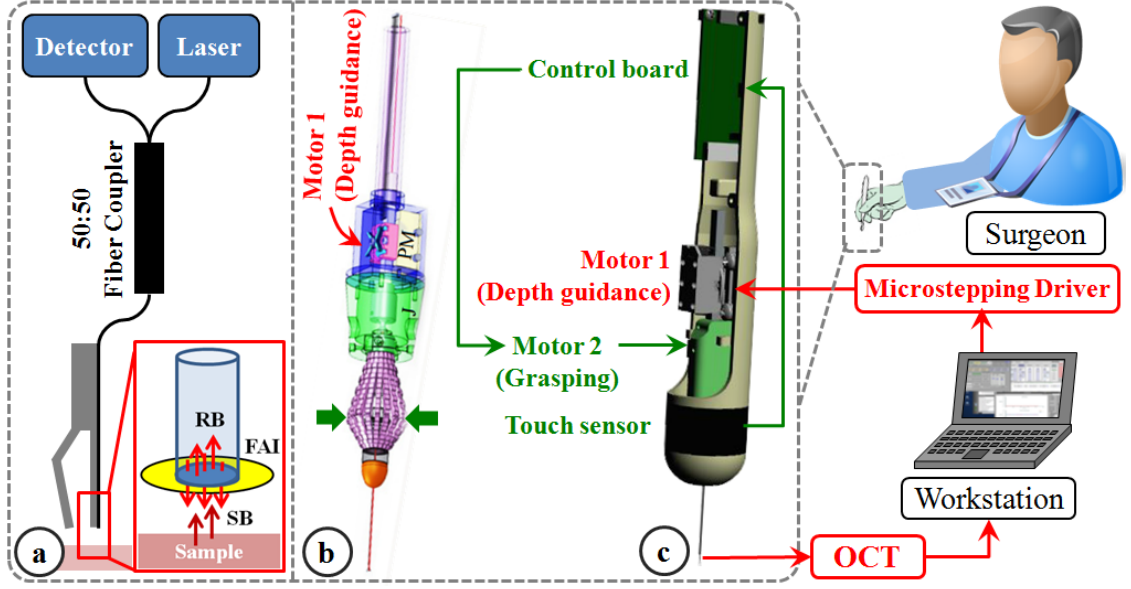


**Figure 4.2.** (a) CP-SSOCT fiber-optic setup: the reflected beam (RB), fiber-air interface (FAI), and the sample reflected beam (SB). Overview of our CP-SSOCT depth-guided micro-forceps system: (b) earlier "SMART: microforceps prototype using one actuator for depth guidance and the squeeze mechanism for grasping [21], (c) current design using a touch sensor and two independently actuated motors for the control of grasping (green) and depth guidance (red) actions.

### 4.2.1 Fiber-Optic OCT Module

The OCT system consists of a swept source OEM engine (AXSUN, central wavelength  $\lambda_0$ : 1060 nm, sweeping rate: 100 kHz, 3 dB axial resolution: 8  $\mu$ m, scan range: 3.7 mm in air), a balanced photo-detector and a digitizer with a sampling rate of up to 500MSPS with 12-bit resolution, a Camera Link DAQ Board, and a Camera Link frame grabber (PCIe-1433, National Instruments). The optical setup is compact due to the use of fiber-

optic based setup. In the case of CP-OCT, the OCT system does not require reference arm because it uses the reflection beam from an interface between fiber (sample arm) and air (medium) as a reference beam as shown in Figure 4.2a. Thus, CP-OCT is naturally immune to dispersion and polarization noises.

#### 4.2.2 Micro-Forceps Module

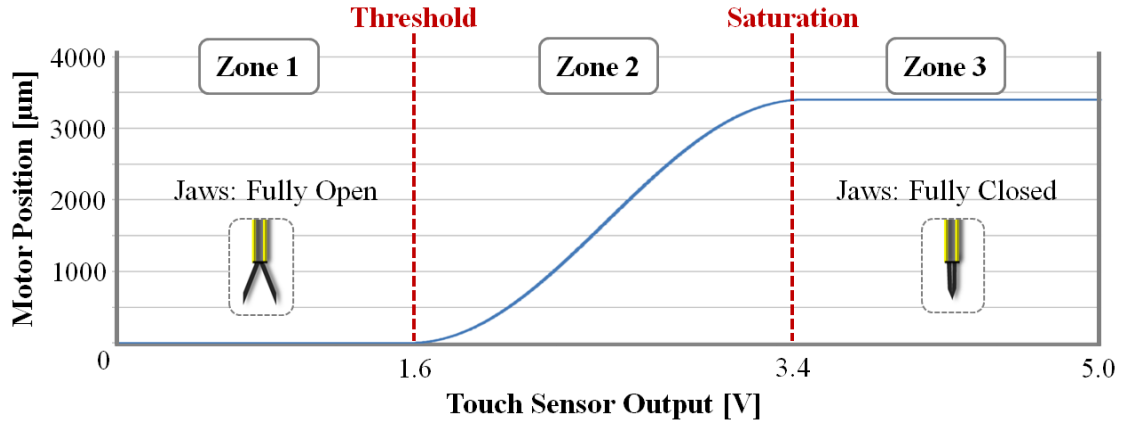


**Figure 4.3. Calibration curve for the touch sensor. The curve is divided into three zones: (1) dead zone where the tool-tip manipulating motor does not react to the touch sensor, (2) active zone that is responsible for motor control, and (3) saturation zone where the motor has reached its maximum position.**

The design of our micro-forceps (Figure 4.1b-e) involves two linear piezoelectric motors, a handpiece, a touch sensor, a fiber-optic sensor, an actuated tool-tip, and a custom-built control board. A prototype, shown in Figure 4.1b, was 3D printed using acrylonitrile butadiene styrene (ABS) thermoplastic. The design provides two actuated degrees of freedom, which are completely independent of each other: (1) involuntary motion compensation and (2) grasping. The first piezoelectric linear motor (LEGS-LT2010A, PiezoMotor), M1 in Figure 4.1c, is for motion compensation and is fixed to the handpiece. The motor has its own driver (PMD101, PiezoMotor), and is used to move the actuated tool tip relative to the handpiece within a maximum stroke of 80 mm. The actuated tool

tip consists of 3 main parts. The first part is a piezoelectric linear motor (M3-L, New Scale Technologies), M2 in Figure 4.1c, which is used for opening and closing the forceps jaws. It embeds the motor driver, encoder, and electrical circuit that communicates with the custom built control board through a SPI communication protocol. Attached to the motor shaft, the orange piece in Figure 4.1c is the second part. This part holds and slides up and down the guide tube for opening and closing the forceps jaws. The forceps jaws are open in default and firmly anchored to the motor body. One arm of the jaws is straightened and flattened providing a proper space for fiber-optic sensor attachment while the other arm is bent open (Figure 4.1d). As the guide tube moves forward, the bent arm of the compliant jaws is squeezed and moves toward the other straight arm providing a firm-grasping platform. When the guide needle moves backward, the bent arm flexes back opening the jaws. During this grasping and releasing action, the straight arm never bends or moves so that there is no adverse effect on the fiber-optic sensor.

The grasping action is controlled by how firmly the user pushes on the touch sensor. The touch sensor (FSR 408, Interlink Electronics®) is an interface to transfer the user signal to activate the grasping. We tested and build a voltage divider circuit to measure its variable resistance that produced desired output response. As a result, we are now able to focus on a certain range of forces by selecting the reference resistor value. In our case, we used a 10 k $\Omega$  resistor matching the force pressure range used by an operating surgeon. Note that both the sensitivity and the dynamic range can now be deliberately tuned. Additionally, we developed a grasping calibration curve table in order to provide control flexibility of the touch sensor and also control of the grasping manipulation motor as

shown in Figure 4.3. The table is divided into three zones: 1) Threshold, 2) Active and 3) Saturation zones. By changing the threshold and saturation value, we can customize the sensitivity of the touch sensor for each user. The curve equation in an active area,

$$pos = A_{\max} \left\{ \cos \left( \frac{\pi (v - V_1 + V_2)}{V_2} \right) + 1 \right\} \quad (1)$$

where pos is the position of motor M2,  $A_{\max}$  is the maximum traveling length,  $V_1$  and  $V_2$  are the voltages for threshold and saturation lines, and  $v$  is the input voltage applied to the touch sensor. To attach the CP-OCT distal sensor probe, we unfolded one of the forceps fingers. Also, a groove was made on the side of the guiding needle to protect the fiber to tool-tip interface as shown in Figure 4.1e.

#### 4.2.3 PCB design

We built a customizing control PCB board based on the ARM Cortex-M4 32b MCU (STM32F405, 168MHz, STMicroelectronics) in order to read touch sensor output and control the forceps-tip controlling motor as shown in Figure 4.4 and 4.5. This control board communicates with the workstation through USB connection; at the same time, power is also supplied by this USB connection. According to the USB specification, the certified USB port and cable can transmit 2A maximum current with 5V. Specifically, HID (Human interface device class) protocol is used for communication and one of the advantages of HID protocol is that most of the recent operating system basically support this HID protocol so that we don't need to develop or install additional device driver for our control board. We used the built-in 12bit analog-to-digital (ADC) converter to reads the force applied to our touch sensor. The resistance is varied by the pressure on the

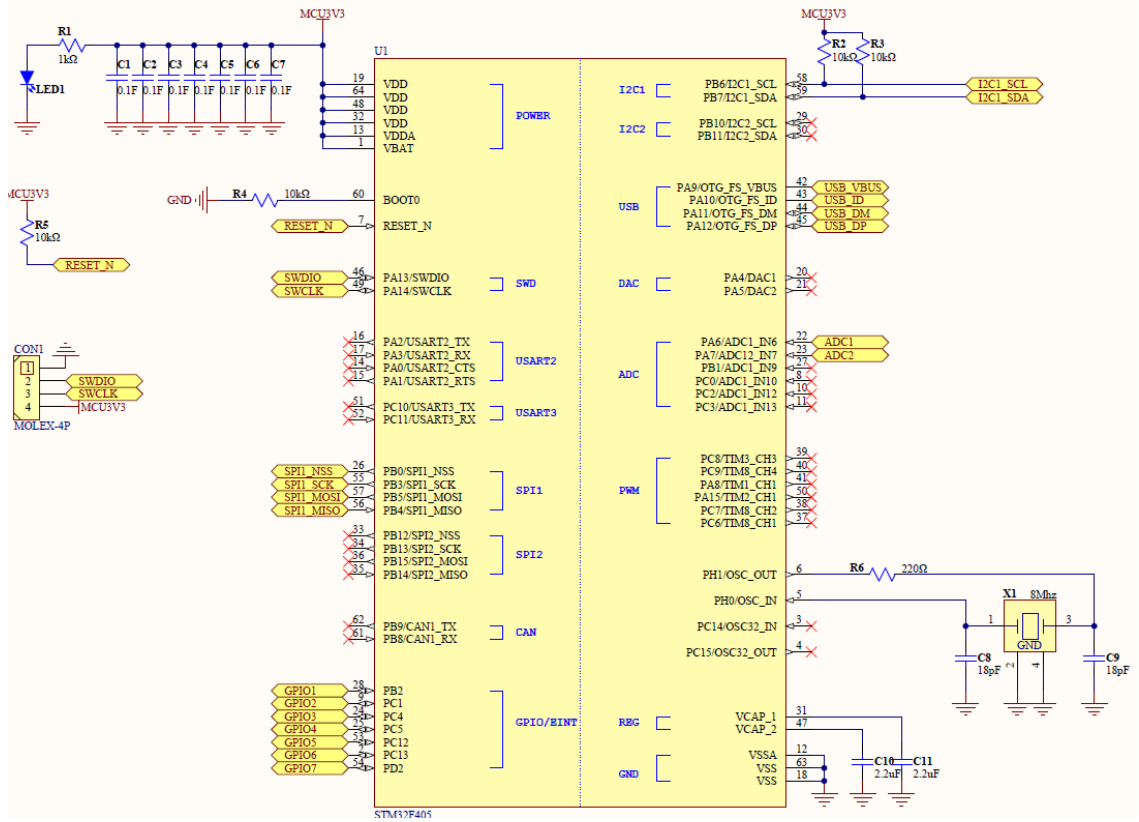


**Figure 4.4. Schematic of the circuit design for MCU (STM32F405) part.**

surface of the touch sensor. Thus, we need to design a voltage follower circuit to convert the resistance value into the readable voltage value. Here, we can adjust the sensitivity of the sensor by changing the value of resistance of R8 in Figure 4.5c. As mentioned in previous section, we used SPI (Serial Peripheral Interface) communication to control the squiggle motor for opening and closing the forceps jaws. Typically, we need four pins for SPI communication. The first pin is to activate the slave device. SPI is designed to communication multiple slave devices and master device select specific slave devices by using this activating or reset pin. Then, the communication is synchronized by the clock signal in second pin. Then, the other two pins are used for data transmission and their names are determined by the direction of the data flow. MOSI means Master Output



**a** USB Connection & Power (5V)

**b** Squiggle motor Connection (SPI)

**c** Touch sensor (ADC)

**d** Power supply (MCU)

**e** Power supply (Motor)

75

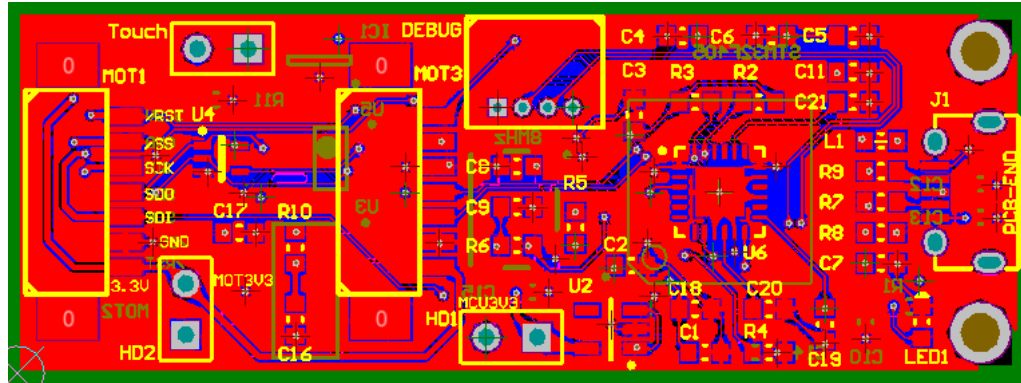


Figure 4.6. Layout of the designed control board circuit.

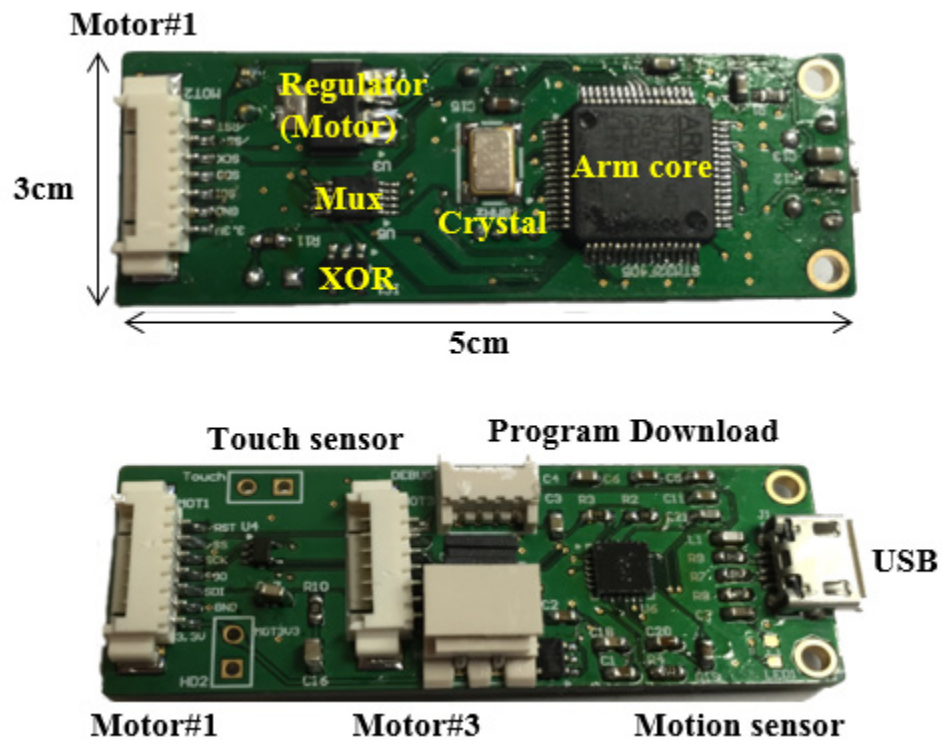
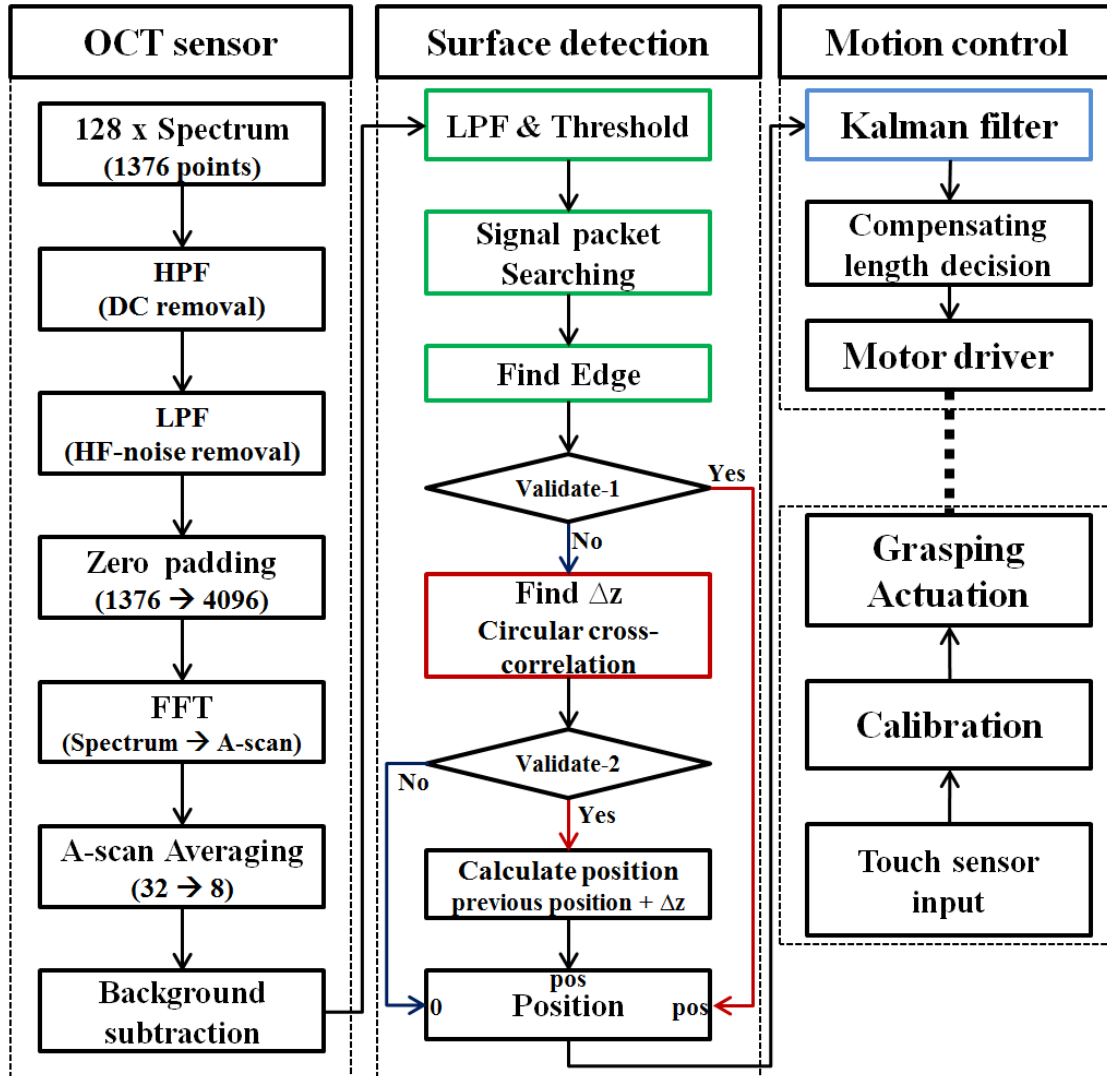


Figure 4.7. Image of the Implemented control board based on the circuit design. All the components are mounted on the PCB. The upper image shows the top layer of the board and the lower image shows the bottom layer of the board.

#### 4.2.4 System Software Module

As shown in Figure 4.8, the CP-OCT spectral data for the distal sensing is sequentially processed in the workstation following three steps[51]. The overall processing procedure consists of three main parts: 1) OCT signal process, 2) surface detection, and 3) motion control. The total processing time is significantly reduced with the help of parallel processing based on GPU programming (CUDA, Nvidia). Specifically, the first step of the processing is to transform the spectral data to A-scan data. 128 consecutive spectra consisting of 1376 data points are transmitted from the frame grabber in every 1.28 ms. A high-pass filter is applied to the spectrum data to remove the high DC component in spectrum data and a Low-pass filter is consecutively applied to remove high-frequency noise components. After FFT, averaging and background subtraction are conducted on the A-scan data. This produces an A-scan with 2048 data points that cover a 3686.4  $\mu\text{m}$  axial distance from the end of the fiber.

The final A-scan is passed to the next process that detects the tissue surface. The A-scan of a retina, which has a multi-layered structure, has a complex shape and the most significant reflection beam does not always come from the sample surface; as a result, simple peak detection is not appropriate for tracking the distance from the sample surface. Instead, we use an edge detection method after low-pass filtering the Fourier transformed A-line OCT signal. Additionally, we need to improve the robustness of the surface detection process by focusing on the features of the A-scan that reflect the retinal anatomical structure. Thus, we applied circular cross-correlation to two consecutive A-scans to find the distance variations. Finally, the calculated position value is transmitted to the third step. Instead of using the position value directly to control the motor, a



**Figure 4.8. Data processing flowchart consisting of 1) OCT signal processing, 2) Surface detection signal processing, and 3) Motion control processing. Each step is implemented in independent software module; especially, the OCT signal processing module uses parallel processing technique based on GPU programming.**

Kalman predictor is applied for more accurate motion compensation. This prediction step is necessary to make up for the computational and communication time delay between the spectrum measurement and the actuator operation. Finally, the compensating value is transmitted to the motor driver.

### 4.3 Experiments

In an epiretinal membrane peeling procedure, prior to membrane delamination, the surgeon first brings the forceps tip above the target area, and then carefully moves it to the surgical depth required to grasp the membrane edge. Due to the limited axial resolution through the surgical microscope and tool manipulation in the axial direction, as well as partial obstruction of the target by the tool tip, tool shaft, shadows and the retina itself when the tool is engaged in tissue, it is not trivial bring the tool tip to the surgical target depth with precision. In actual practice, surgeon routinely move the tool tip very slowly into the membrane and make multiple attempts to grasp until the target is successfully engaged and the membrane edge lifted. Ideally, a surgeon would bring the forceps tip directly to the precise desired target depth for efficient and safe grasping using a single attempt. This hypothetical ideal is not presently possible for most surgeons due in part to physiological hand tremor, patient movement and the inherent motion artifact during forceps actuation. Our CP-SSOCT guided micro-forceps' depth-locking feature is designed to eliminate this problem and bring the tool tip to the desired depth with ease, precision, and safety. In order to demonstrate the performance of our tool, two sets of experiments were performed by an expert vitreoretinal surgeon.

In the first set, the aim was to monitor the motion artifact at the tool tip during grasping in three cases. First, the surgeon was asked to use a standard 23 gauge (Ga) manual micro-forceps (with an OCT fiber probe attached to the jaws' tip) to complete 10 grasping attempts on a thin film target while trying to maintain the forceps tip as close to the target surface as possible without touching the surface. The tool tip position relative to the target surface was acquired from the attached CP-OCT distal sensor (sampling

period = 1.28 ms). In the second and third cases, the same surgeon was asked to repeat the procedure using our micro-forceps without and with the motion guidance feature (target distance from the surface = 500  $\mu\text{m}$ ) respectively.

Our second set of experiments aimed at assessing the efficacy of our tool in terms of the time required to successfully pick up a target from a delicate surface, the total number of grasping attempts, and the maximum depth of unintended penetration (damage) to the underlying surface. In our trials, as the target to be grasped, we used pieces of optical fibers with comparable thickness to an epiretinal layer (125  $\mu\text{m}$  in diameter) on top of a soft polymer as shown Figure 11a. The task of the surgeon was to grasp and pick up the fiber piece without damaging the underlying polymer surface in the shortest possible time. Two cases were investigated using our tool: with and without motion guidance. 20 trials were completed per case by randomly turning on and off the motion guidance feature for blind testing.

Figure 11a is the screenshot of the developed GUI program for this experiment, which displays the synchronized real-time A-scan, video of the operation site, and output of the touch sensor. The recorded video was used to determine the number of attempts and the elapsed time to successfully grasp and pick up the fiber pieces, leading to a resolution of 1 s. In order to assess the maximum depth of damage on the polymer surface, we used another 2D scanning OCT imaging system.

## **4.4 Results and Discussion**

### *4.4.1 Evaluation of Motion Artifact during Grasping*

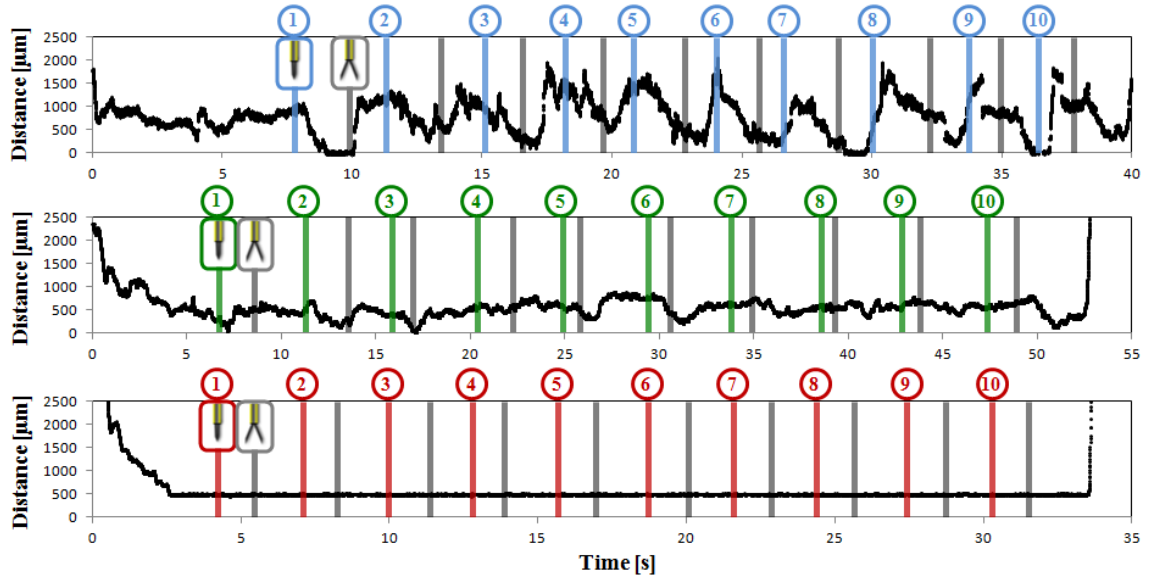


**Figure 4.9.** Measured distance variation as the surgeon opens and closes the forceps while trying to maintain the tool tip fixed above a thin film layer (a) using a conventional 23 gauge micro-forceps, using our micro-forceps (actuated via the touch sensor) (b) without and (c) with the motion guidance feature. 10 grasps were performed for each case. Vertical bars show the opening and closure of the forceps jaws. The motion artifact was significantly reduced by the using the touch sensor based actuation on our tool rather than the squeezing mechanism on the conventional micro-forceps.

The measured tool tip position during the 10 grasps in each case is shown in Figure 4.9. When the standard manual micro-forceps was used (Figure 4.9a), the distance from the target significantly varied, with a large movement each time the jaws were closed and with some high-frequency oscillations due to operator's hand tremor. The tool tip consistently moved forward while grasping and backward while releasing. Surface contact (distance = 0  $\mu\text{m}$ ) was observed in three of the ten grasps, which could lead to unintended force exertion on the retina and thus injury in case of an actual surgery. According to prior work, surgeons receive very little force feedback during retinal microsurgery[69]; therefore, responding in real time to inadvertent retina contact is not yet feasible without assistance.

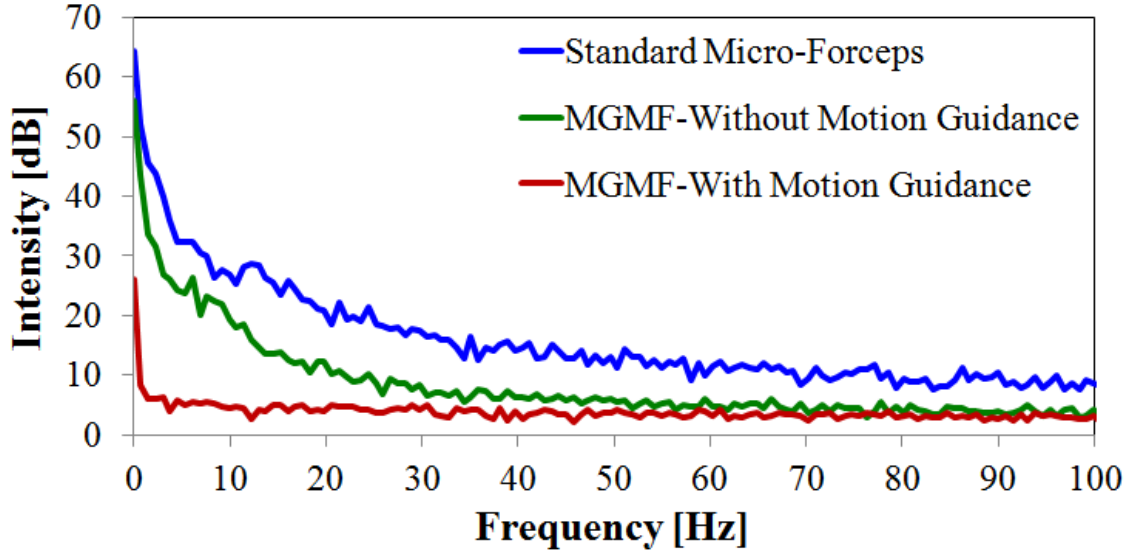


**Figure 4.10. Frequency analysis of the distance variation during the grasping actions: (a) using standard manual micro-forceps, using our motorized micro-forceps (b) without and (c) with the motion guidance feature.**

The second and third case trials were completed using our micro-forceps. As shown in Figure 4.9b, the motion artifact was significantly reduced during tool-tip manipulation even without the active motion guidance. A major contributor to this stabilization is that the user needs to apply a relatively lower force on the tool handle to grasp since the input is sensed by a touch sensor and actuation is achieved by a motor. The motorized architecture also has removed the moving parts on the tool handle as opposed to the squeezing mechanism on the conventional micro-forceps thereby yielding a potential stability advantage. When the motion guidance feature was turned on, the targeting error at each grasp was almost eliminated (Figure 4.9c) and the forceps tip was successfully maintained 500  $\mu\text{m}$  above the sample surface throughout the test. The standard deviations of the distance variation during the grasping action in these three cases were 330.73  $\mu\text{m}$ , 119.81  $\mu\text{m}$ , and 5.11  $\mu\text{m}$  respectively. Figure 4.10 shows the frequency analysis of the



acquired distance data for each case, where the intensity (I) for each case was obtained using the following equation:

$$I_j = \frac{1}{N} \sum_{i=1}^N \left[ 10 \times \log \left( 1 + \text{abs} \left( \text{FFT} \left( \left| \frac{\text{Data}_i - m}{m} \right| \right)_j \right) \right) \right]$$

In equation (2),  $i, j, m$ , and  $N$  are the trial index, frequency component index, target depth, and total trial number, respectively. According to the graph, the usage of touch sensor reduced the intensity of the components over the entire frequency area. On the other hand, the compensating motion by the system effectively suppressed the low-frequency components located in 0 to 40 Hz. These results dramatically demonstrate the effectiveness of this approach in suppressing the grasping induced motion artifact present with manually operated and unassisted forceps. During actual surgical operation, the motion artifact is in part suppressed by the passage through trocars (Figure 4.1a) which dampen mostly the lateral movements; though, the stabilizing effect in the axial direction by trocar use is limited.

#### 4.4.2 Grasp and Pick up Experiments

The results of this experiment are shown in Figure 12. Accordingly, the motion guided trials show significantly better performance in all considered aspects. Without the motion guidance, the surgeon spent 7.9 s to successfully grasp the fibers on the average (min:5.0 s, max:12.2 s). The number of grasping attempts had a mean of 1.6 (min:1, max:3) while the maximum depth of damage averaged 101.8  $\mu\text{m}$  (min: 25.2  $\mu\text{m}$ , max: 219.6  $\mu\text{m}$ ). When the OCT-based motion guidance feature was used, means were drastically reduced, leading to a mean operation time of 6.1 s (min:4.0 s, max:8.1 s), 1.05 attempts before

successful grasping on the average (min:1, max:2), and a mean damage depth of 13.14  $\mu\text{m}$  (min:4.5  $\mu\text{m}$ , max:27.0  $\mu\text{m}$ ).

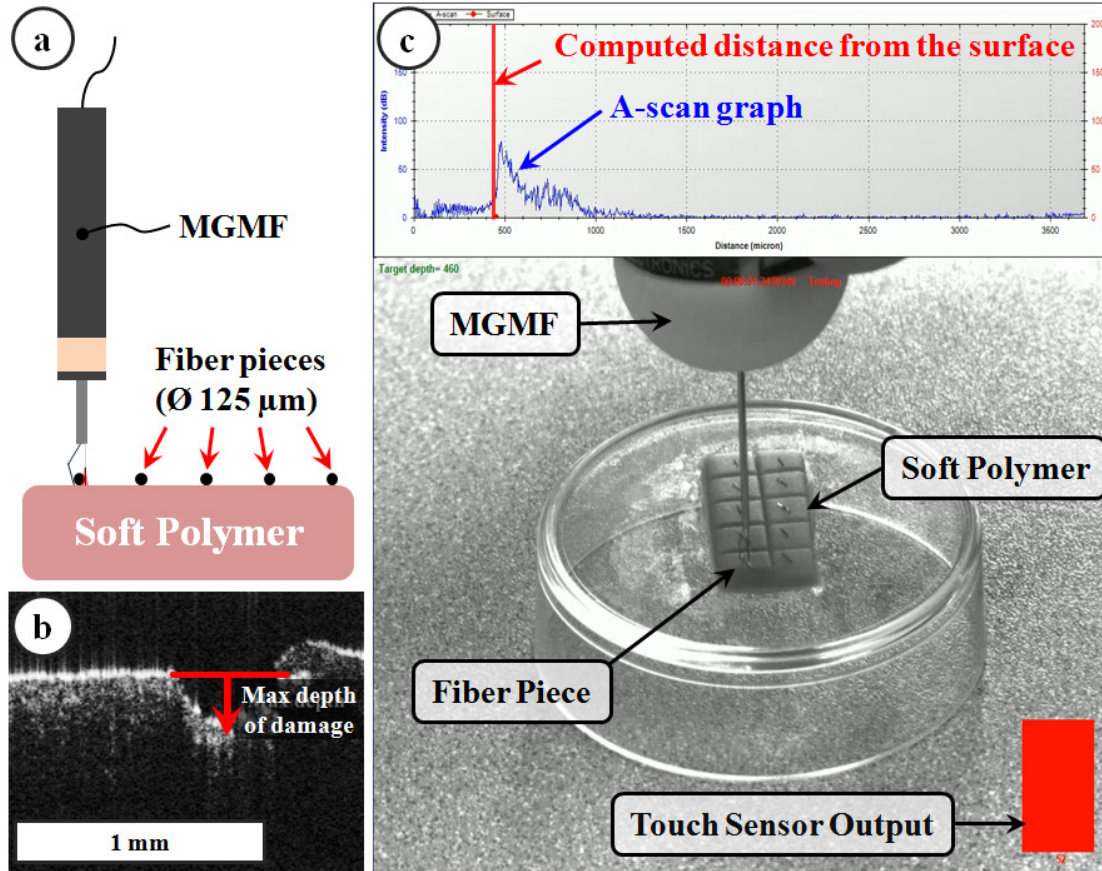


**Figure 4.11. (a) Grasp and pick-up experiments: small fiber pieces ( $\text{Ø } 125 \mu\text{m}$ ) were picked up from a soft polymer surface using MGMT. (b) A 2D scanning OCT imaging system was used to analyze the damage created on the polymer surface after each grasp. (c) A snapshot of the developed software displaying real-time A-scan data, video view of the operation site, and the touch sensor output (red bar graph).**

The efficacy of motion guidance can be better observed when the maximum depth of damage is graphed relative to the elapsed time as shown in Figure 13, where the point distribution of the trials without the motion guidance is significantly wider than that of the motion guided trials. We computed the total distances from the center of each distribution in order to quantify the degree of distribution, and the value of freehand trials

was 6.32 times larger than that of guided trials. The nonparametric Kruskal-Wallis One Way Analysis of Variance (ANOVA) on Ranks ( $p=0.00084$ ) indicated that the mean values for the motion guided and unguided trials were statistically significantly different.

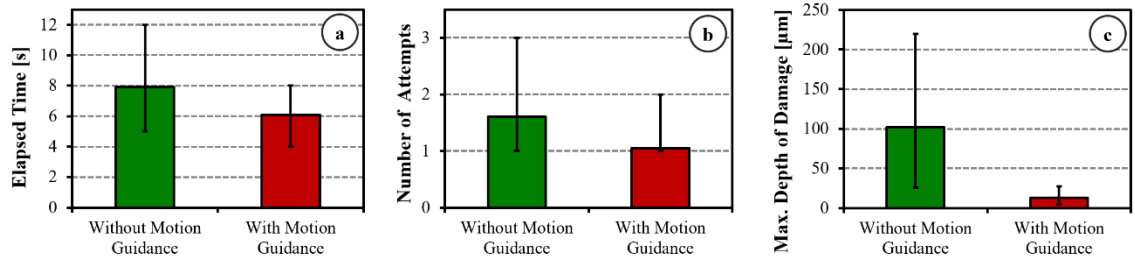


**Figure 4.12. Results of the grasp and pick-up experiment: Statistically significant reduction in (a) elapsed time, (b) number of grasping attempts, and (c) the maximum depth of damage on the substrate with the use of our OCT-based motion guidance feature. The solid bars show the mean, and the error bars represent the maximum and minimum values.**

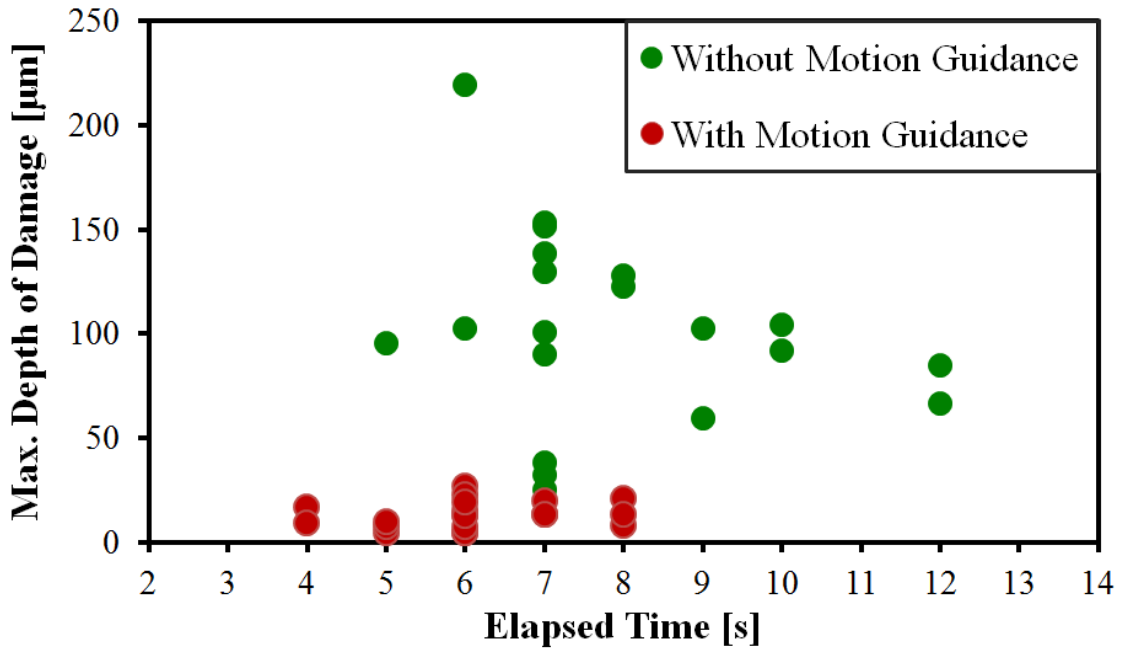


**Figure 4.13. The maximum depth of damage vs. elapsed time during the grasp and pick-up experiments. The trials without the motion guidance have a significantly wider distribution than the guided trials, which have are grouped around much smaller damage and elapsed time levels.**

## 4.5 Conclusion

In conclusion, we have built and demonstrated a novel motion compensated micro-forceps that allows accurate depth targeting and precise depth locking during both grasping and peeling operations. One of the key innovations of this tool is that it separately controls the motion compensation and grasping motion of the forceps. To achieve this, we used two independently actuated motors and controlled the grasping electronically via a touch sensor rather than the mechanical squeezing mechanism on the standard forceps tools. This touch sensor-based actuation enabled the operator to grasp by applying less force on the tool handle and eliminated the squeeze induced motion artifact during grasping. The touch sensor alone represents a substantial improvement in instrument control and precision. Moreover, when both the touch sensor based actuation principle and the CP-SSOCT based motion guidance feature were used together, our preliminary grasping tests with a vitreoretinal surgeon showed significantly reduced operation time, fewer number of attempts and less damage on the underlying surface while grasping and lifting small fibers up from a soft polymer surface. Our current work is focused on further performance evaluation of this technology on biological tissues and investigating its feasibility using *ex-vivo* animal models.

## **CHAPTER 5 : SMART MICRO-INJECTOR BASED ON HANDHELD CP-SSOCT GUIDED MICROSURGICAL TOOL**

### **5.1 Introduction**

Needle devices to inject therapeutic and diagnostic agents to patients are among the most commonly used medical devices. By delivering therapeutic materials directly to target areas, it is expected that maximal efficacy, while minimizing drug dose and side effects will be achieved.

In ocular surgery, the ability to consistently perform intra-retinal microinjection with precision is not yet established although the capability could revolutionize the treatment of degenerative retinal diseases that cause blindness. At present, there are many degenerative retinal diseases that cannot be treated completely and ocular gene therapy has emerged as a promising method to manage such untreatable inherited retinal diseases[70], [71]. Various gene vectors have been developed are delivered to target areas by microinjection. At present, subretinal injection is commonly performed to achieve gene therapy. During subretinal injection, the surgeon is totally dependent on manual manipulation of the tools and visualization through a stereomicroscope. However, these two requirements for success are limited by physiological hand tremor and the limited human ability to visually resolve on the micron scale in the axial axis. Moreover, there is potential obscuration of the injecting site by the tool shaft and needle tip[1].

A variety of microinjection systems have been proposed. In bench cell biology, accurate injection of foreign materials such as DNA, RNAi, protein and drug compounds is fundamental to achieve successful expression of desired properties[72]–[75]. Wang et al. developed a computer vision based microinjection system and successfully performed

zebrafish embryos injection with 99% success rate[72]. However, this type of application was in a stable and predictable environment; a surgical environment requires a more dynamic system. The “Steady-Hand Eye-Robot” system has demonstrated its potential to remove physiological inaccuracy and guide a micro-needle to small veins in the chorioallantoic membranes of chicken embryos[73]. In addition, Riviere et al. have developed a fully handheld micromanipulator, “Micron” and have demonstrated various handheld applications including retinal cannulation[75]. However, the solution does not address the limited visualization of the target through the microscope and the difficulty of estimating relative depth precisely through a surgical microscope, so additional information is required. An example of relevant additional information may be provided by a force sensing method to assist retinal microinjection[76].

Optical coherence tomography (OCT) has a micron level of precision and subsurface imaging capability, as well as fast imaging speeds that can provide solutions to overcome existing limitations[9], [17]–[19], [23]. In particular, we have been developing an array of **S**ensorized **M**icromanipulation **A**ided **R**obotic-surgery **T**ool (SMART) that uses a common-path swept source OCT (CP-SSOCT) distal sensor for an axial motion sensing and guidance[63], [64]. We have also adopted a parallel programming technique using a graphic processing unit (GPU) to reduce the processing time for real-time guidance[24]. This distal sensing approach is distinguished from typical OCT “B-scan” imaging in that the distal sensing system extracts a physical distance between the sensor tip and a specified target layer in the acquired multiple A-scan data[29], [31]–[35], [51]. Specifically, sequential A-scans are processed to detect time varying target position and motion. The system counts the pixel distance in the

image domain and then, converts the number to a physical distance. Finally, the distance is utilized for intraoperative motion guidance. Integrating CP-SSOCT feedback with a SMART injector via an intuitive control system that allows the tip of the injector to lock onto the desired depth, regardless of involuntary user motion has been the goal of this development process. A SMART injector approach is therefore a logical extension for future development of handheld instruments.

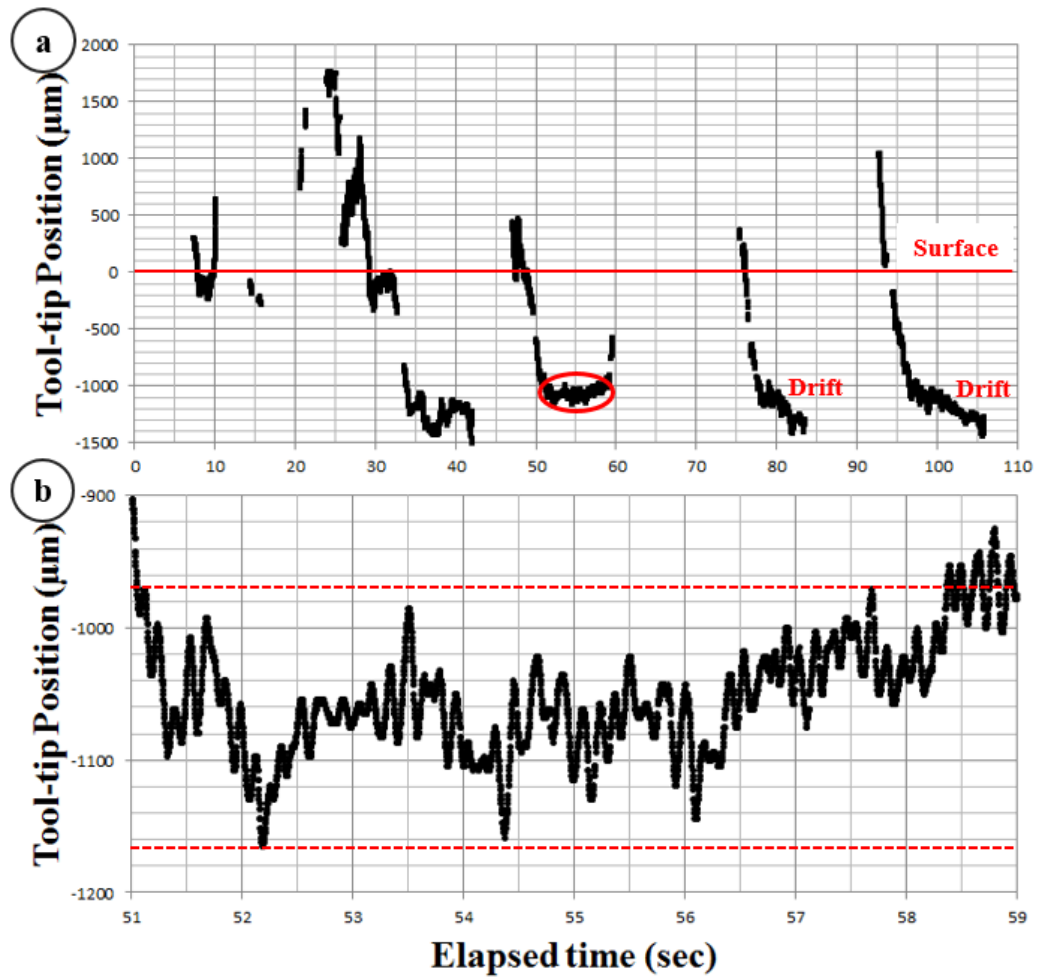


**Figure 5.1. Free hand insertion test performed by retinal surgeon under the microscope: a) needle-tip position tracking data during the insertion trials, b) a partial magnified graph of area in red ellipse in the above graph. The two red dotted lines show the boundary of variation while the surgeon maintained the needle-tip position.**

## 5.2 Materials and Methods

### 5.2.1 *Limitation of Freehand manipulation*

Figure 5.1 shows the position tracking data of a retinal surgeon manipulating the SMART injector under the microscope view. The aim of the study is to insert the SMART injector needle tip into a gelatin phantom and study and compare human control vs the SMART system's ability to target designated depth and to maintain its position during the injection. Considering that the average thickness of human retina is about 250  $\mu\text{m}$ , the manual results shown in figure 1 are quite unsatisfactory and demonstrate the difficulty of freehand microsurgery in the absence of the normal visual cues that are used effectively by surgeons on patients with a high level of success. As figure 1b shows, a surgeon cannot maintain the target position during the injection due to physiological hand tremor and motion in the absence of orienting visual cues. Hand tremor translates into vibrational motion (5-15 Hz) of the needle-tip and prevents the surgeon from maintaining a needle stably in a fixed position. Absence of awareness of the absolute position of the needle-tip in this model induces gradual drift of the position as shown in Figure 5.1a. Thus, accurate depth-targeting and robust depth-locking are technical objectives needed to be achieved for successful micro-injection.

### 5.2.2 *Micro-injector system configuration*

The SMART injection system consists of three main modules: (1) fiber-optic OCT for distal sensing, (2) micro-injector and pump for fluid delivery, and (3) workstation for computing and control. The details of the OCT module were described in our previous work[51]. As an extension of the previous work, we maintain the common-path fiber-



optic OCT setup for a compact design and natural immune to dispersion and polarization due to the alternative reference beam from the fiber tip and shared beam path[63], [64].

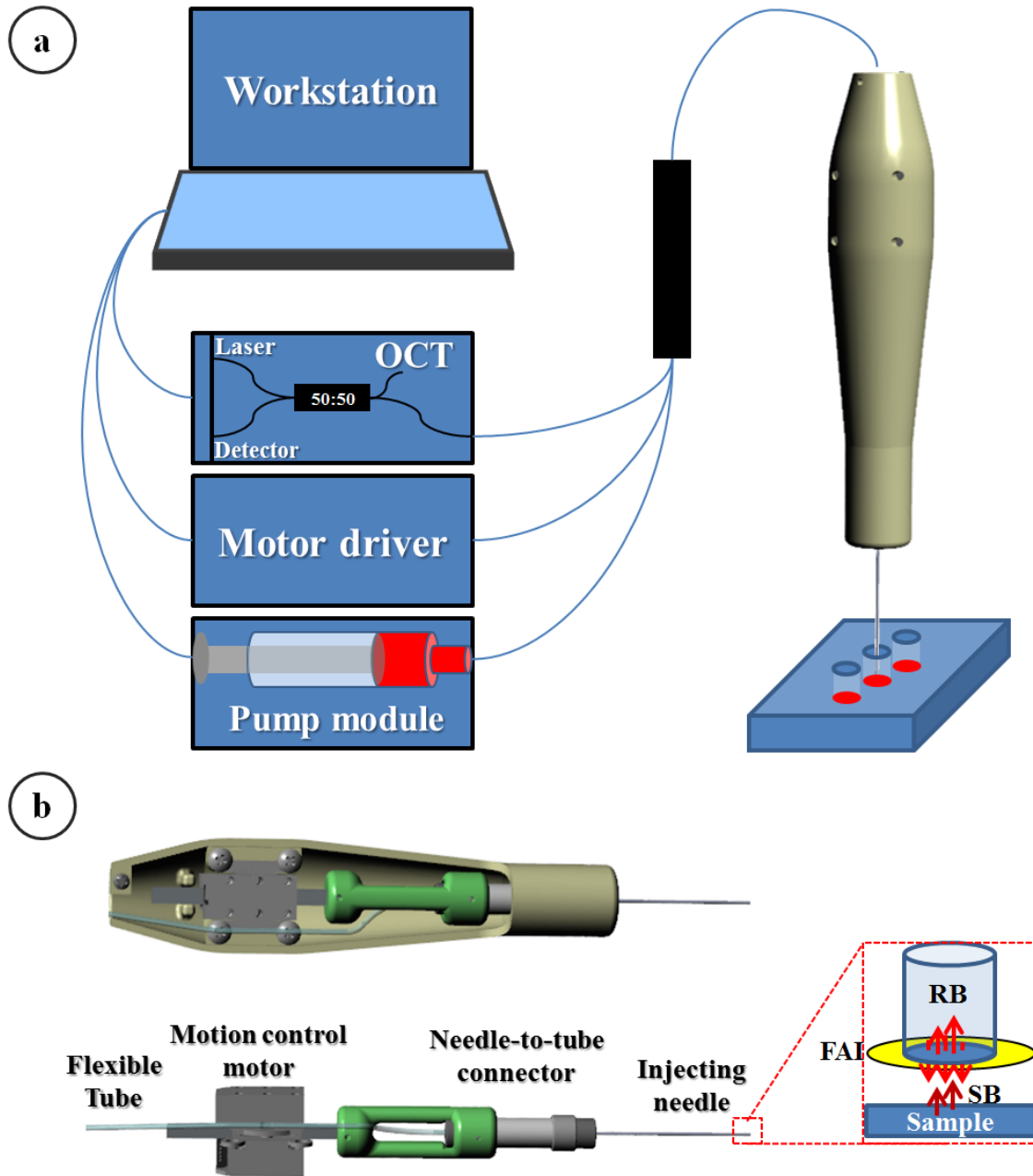


**Figure 5.2. (a) System overview of the CP-SSOCT depth-guided micro-injector and (b) internal structure of the micro-injector and CP-SSOCT fiber-optic sensor: RB (Reflected beam), FAI (Fiber-Air Interface), SB (Sample reflected beam)**

The schematic of our micro-injector is shown in Figure 5.2. For the injection, it involves a 34G needle (Hamilton, OD: 0.1842 mm, ID: 0.0826 mm) inside a 26G guide-needle (Hamilton, OD: 0.4636 mm, ID: 0.260mm), a needle-to-tube connector (RN Coupler-p/n 55752-01, Hamilton) as shown in Figure 5.3. For distal sensing and motion compensation, it also has a linear piezoelectric motors (LEGS-LL1011A, PiezoMotor), a fiber-optic probe, and a handpiece of the injector. A prototype was 3D printed using acrylonitrile butadiene styrene (ABS) thermoplastic. The pump module is composed of a 100  $\mu$ L capacity syringe (Hamilton) with 1.46mm inner barrel diameter and 0.60 mm forward push, which corresponds to 1 $\mu$ L-volume injection. A 1  $\mu$ m-precision linear actuator (850G Actuator, Newport) was used to accurately drive the syringe. To connect the injection needle remotely from the syringe, we used a 1 m length of 1/16-inch PEEK tube (Tub PEEK Blu, IDEX).

The sampled OCT spectral data for the distal sensing is sequentially processed in the workstation following the main three steps as shown in Figure 5.4. Most of the OCT signal processing methods utilized in this platform is based on our previous work[51], and they are summarized next for completeness. The first step of the processing is to transform the spectral data to A-scan data. As the sweep rate is 100 kHz, the OCT engine returns 128-buffered spectral data every 1.28ms. These oversampled data are useful to increase the signal-to-noise ratio because the temporally and spatially averaged data within a restricted window based on target size and speed effectively remove speckle noise, which is the one of the main noise factors in A-scan[77]. However, the increased processing time due to the oversampled data has serious adverse effects on intraoperative guidance capabilities. Parallel processing using a GPU significantly reduces the

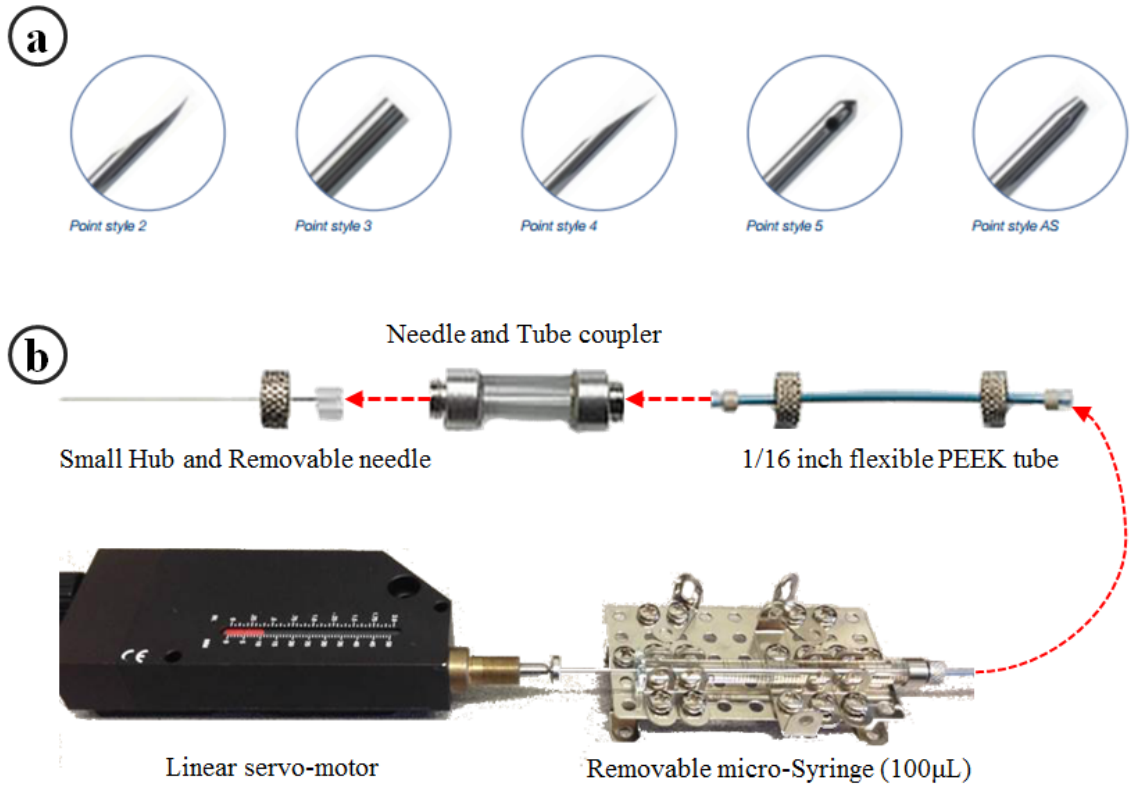


**Figure 5.3. a) Diverse types of needle-tip (Hamilton®), b) custom-built pump module consisting needle, needle and tube coupler, flexible tube, micro-syringe, and linear servo-motor.**

processing time. High-pass and Low-pass filters are sequentially applied to remove the high DC component and high frequency noise components. Next, zero padding and FFT and averaging and background subtraction are conducted on the A-scan data. This produces an A-scan with 2048 data points that covers a 3686.4  $\mu\text{m}$  axial distance from the end of the fiber probe. The processed A-scan is passed to the next step for distal sensing. As mentioned in earlier work, the A-scan of the tissue that has a multi-layered structure has a complex signature. Thus, we use not only edge detection to determine the absolute position of the surface but also used a shifted cross-correlation method to determine distance variation (relative position) between temporally adjacent data. Of

significance, the method based on cross-correlation is advantageous in that it uses the features of the A-scan that reflect deep tissue anatomical structure, and detect distance variance robustly, where each A-scan point is vulnerable to noise. Finally, the calculated position value is transmitted to the third motion control step. A Kalman predictor is used to make up for the computational and communication time delay. The axial motion guidance is controlled based on the distance between the needle-tip and the sample surface as shown in Figure 5.4 (Motor control part) and Figure 5.6a. Two virtual lines first section the spatial domain: 1) “Active-Line” and 2) “Safety Barrier-Line”. After injection, a user withdraws the needle-tip and the system discontinues the compensatory motion. A stop signal is generated when the summation of the compensating length exceeds the preset threshold value.

### 5.2.3 Gelatin phantom injection test

As shown in Figure 5, we first conducted a fluorescein dye injection test to assess SMART injector characteristics. We used 10% gelatin as a phantom. Five injections were conducted serially and the system stably maintained the desired position of the needle-tip during the injections. The system was held in position for 1 sec to ensure the stability of the needle-tip prior to injection and then, it automatically injected 50 nL of fluorescein dye at the desired depth, into the transparent gelatin. The system provided auditory feedback to signal injection completion. We measured the root mean square error (RMSE) during the lock-in state in order to evaluate our system and the equation of the RMSE:

$$RMSE = \sqrt{\frac{1}{N} \sum_{i=1}^N (x_i - y)^2} \quad (1)$$

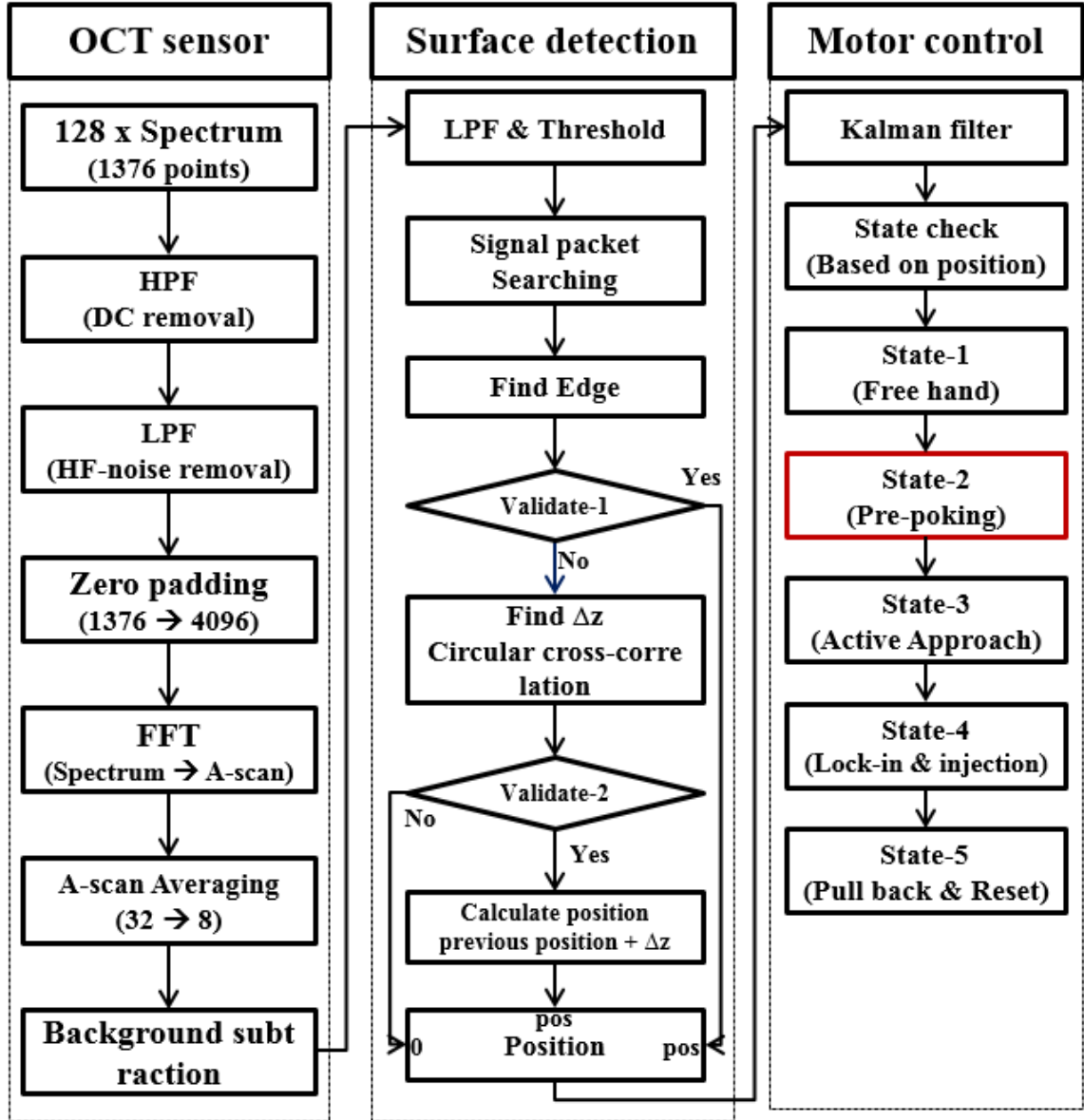


**Figure 5.4. Flow chart of OCT data processing for distal sensing and motion control.** The processing consists of three main parts: 1) OCT data transformation from measured spectral data, 2) distal information extraction from the OCT data, and 3) motion control based on the distal information.

where  $N$ ,  $x_i$ , and  $y$  are the total number of data,  $i$ -th position data, and the desired depth, respectively. The RMSE values for the five trials are denoted in the Figure 5.5a and the total average is  $4.84 \mu\text{m}$ . This value is smaller than the value in our previous work[51].

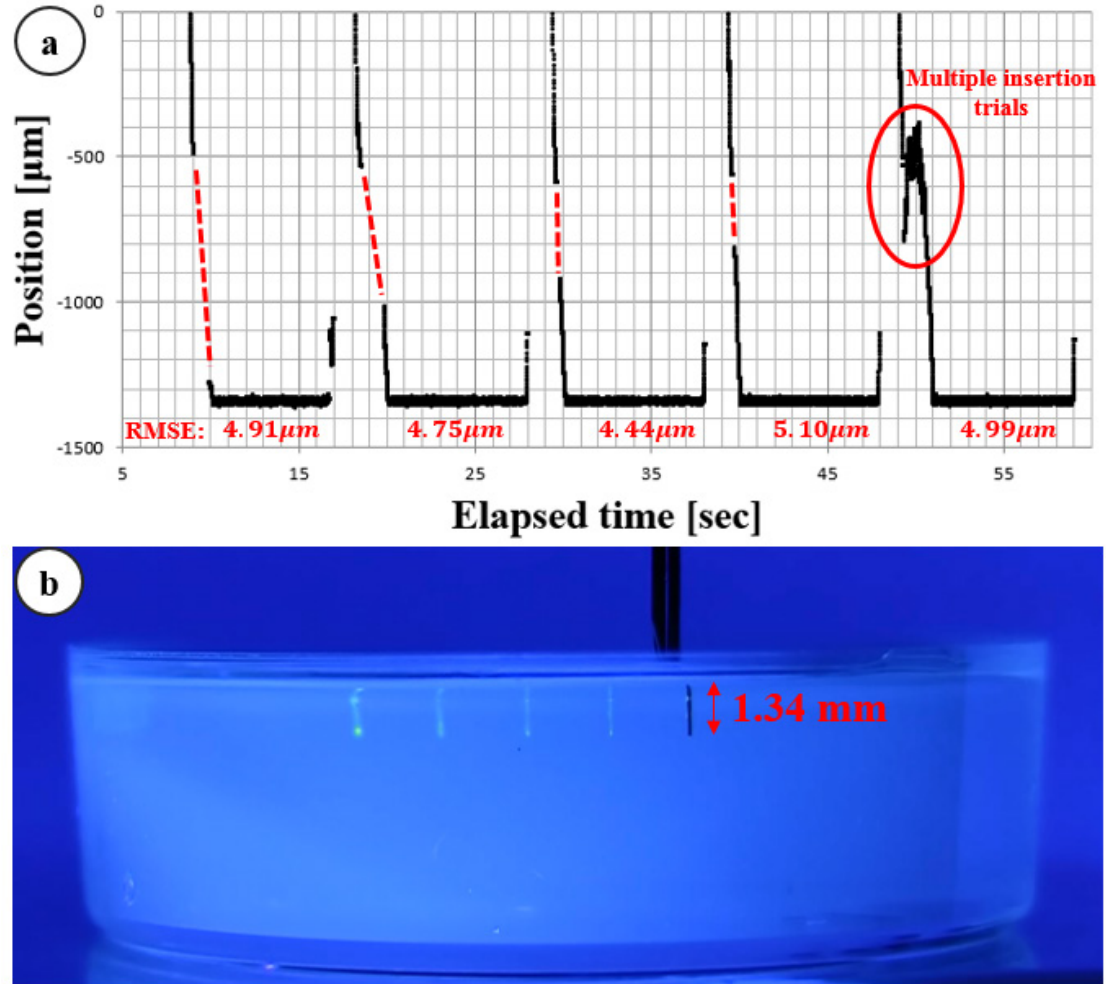


**Figure 5.5. Preliminary 10% gelatin phantom injection test: a) distance tracking data which has blind area caused by surface deformation, b) five consecutive injection trials on a gelatin sample. The preset penetration depth was 1.34 mm.**

The main reason is that the friction between the gelatin phantom and inserted needle tip decrease the vibrational motion (stabilizes). However, there was an undesirable phenomenon during the inserting process. As shown by the red dotted lines in Figure 5.5a, there was an OCT blind zone during the needle insertion. The etiology of the signal void is surface deformation at moment of needle contact in Figure 5.6a. In particular, the gelatin sample was homogeneous and had specular reflection; as a result, the OCT signal

was susceptible to any tilted angle of the surface. Depending on the sample properties, the above signal loss issue is not critical especially in that biological tissue typically gives a predominantly diffuse reflection. However, surface deformation is still problematic in that precise needle tip positioning in thin tissues such as retinal will need to account for both surface deformation as well as port position in the various needles and sizes available.

#### *5.2.4 Mechanics of dynamic needle insertion*

Needle insertion or injection is a common technique for accessing a point that would be otherwise difficult or impossible. Needle insertion into soft materials frequently results in sudden rupture or uncontrollable crack extensions. Several factors inducing the rupture includes inhomogeneity and changes in structure that affect the flow of energy into the cracks[78], [79]. Once the degree of surface deformation is increased more than a certain level, a rupture event occurs. Specifically, strain energy is propagating to the cracks inside the tissue and causing them to more extend during the rupture. In our application, this rupture event is the point that the needle-tip really penetrates into the tissue surface. Before the rupture event or actual penetration, the increasing surface deformation can result in critical issues in two points. First, OCT signal can be decreased rapidly when the sample

has mirror-like surface such as cornea. Second, it is difficult to access to the position where locates near the surface. Additionally, penetration with excessive strain energy can produce dangerous damage to sensitive tissue regions. Rupture events can also increase the position error of our distal sensor temporally. All of these issues show up in our initial needle insertion tests as shown in Figure 5.5.

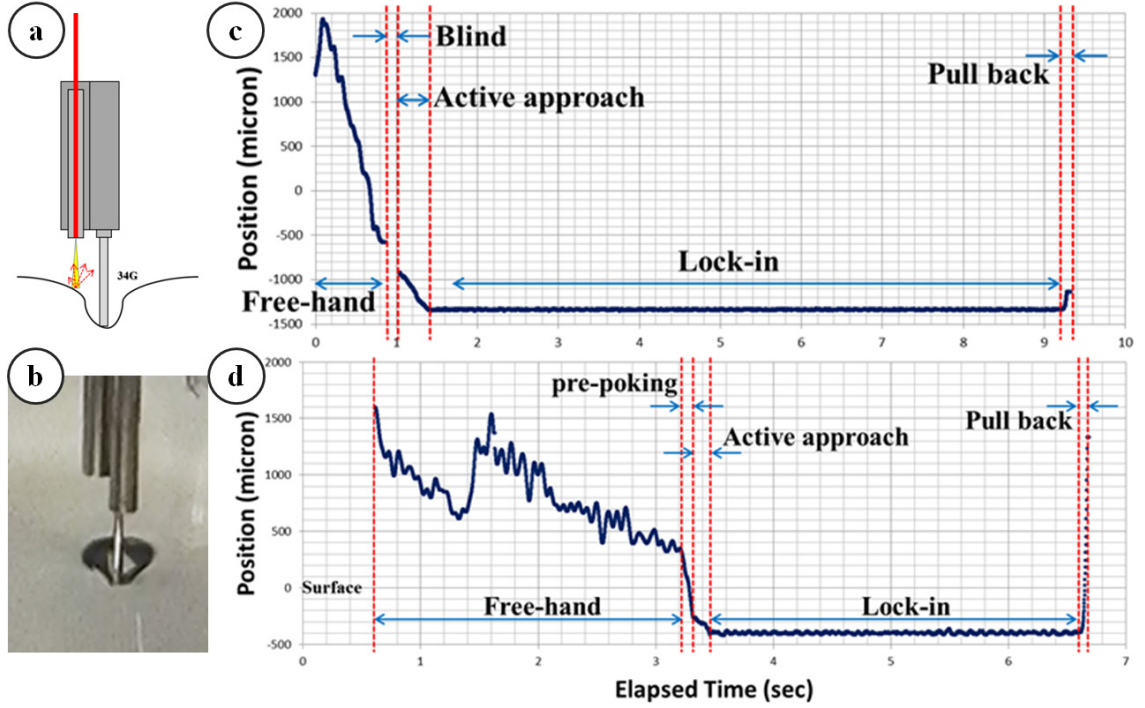


**Figure 5.6. Needle-tip position tracking graph to demonstrate how the system intervenes and guide the needle-tip: a) the tracking data without pre-poking stage and there is blind area due to surface deformation of the sample, b) the tracking data with pre-poking stage and the system achieves maximum speed during this stage to reduce the surface deformation.**

It is commonly known that faster motions of a sharp tool or needle cause less surface deformation during penetration of a biological tissue. This effect should be partly due to the viscoelastic properties of the material. It is likely that both robotic-guided and manual needle insertions can also benefit through control of velocity to produce less deformation, uncontrolled crack extension, and tissue damage. Here, we analyze rupture events that can occur during needle insertion into biological tissue based on the reference works[78], [79]. In particular, we will focus on the insertion force to contact area and insertion speed to analyze the rupture event. The fracture model explains why the rupture force decreases with increasing insertion speed for soft tissue structures. We then develop



a contact model to predict the effect of needle speed on the deformation, and work of rupture. To figure out the surface deformation theoretically, the standard Kelvin model, which is a linear spring-damper model, can be used to predict the surface deformation of biological tissue[80]. The model can be depicted as shown in Figure 5.7.

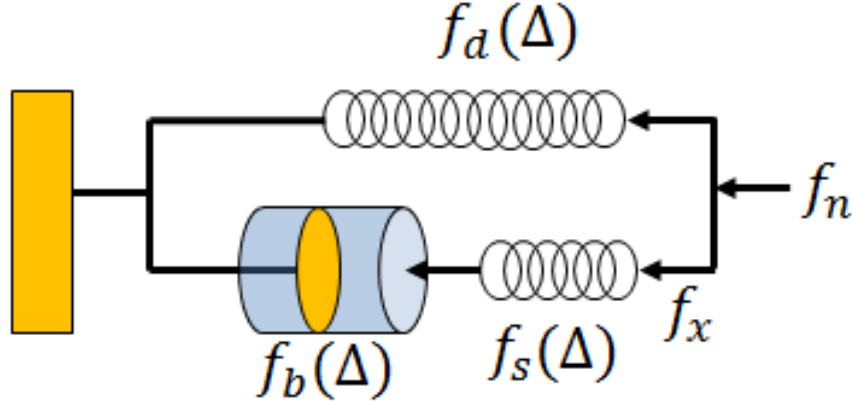


**Figure 5.7. A Kelvin model for the needle inserting into a soft tissue.**

Here,  $f_d(\Delta)$  is a nonlinear force-deflection function, which calculates the static needle force. The  $f_s(\Delta)$  is a series connection of a nonlinear spring and  $f_b(\Delta)$  is nonlinear damper, which relates the dynamic component of the needle force. Here,  $f_s$  and  $f_b$  is a function of  $\Delta$  and the relaxation time of the model  $\tau$  can be described as

$$\tau_d = \frac{f_b(\Delta)}{f_s(\Delta)} \quad (2)$$

This relaxation time is independent of the needle shape and can be replaced by the strain relaxation time of the tissue. The contact force  $f_n$  is given by

$$f_n = f_d(\Delta) + f_x(\Delta, t) \quad (3)$$

where  $f_x(\Delta, t)$  is a dynamic force defined as a function of time  $t$  and deflection  $\Delta$ . The dynamic force is further described by  $f_s$  and  $f_b$ .

$$f_x = f_s(\Delta) \Delta_s \quad (4)$$

$$f_x = f_b(\Delta) \dot{\Delta}_b \quad (5)$$

$$\Delta = \Delta_s + \Delta_b \quad (6)$$

where  $\Delta_s$  and  $\Delta_b$  are the displacements of the spring and damper, respectively. Combining equations (4), (5) and (2) yields

$$\Delta_s = \frac{f_x(\Delta, t)}{f_s(\Delta)} = \frac{f_b(\Delta) \dot{\Delta}_b}{f_s(\Delta)} = \tau_d \dot{\Delta}_b \quad (7)$$

Then, we can use equation (6) and (7) to get the time derivative of the total displacement.

$$\dot{\Delta} = \dot{\Delta}_s + \frac{\Delta_s}{\tau} \quad (8)$$

The general solution of the equation (8) can be obtained by solving a linear differential equation:

$$\Delta_s = \int_0^t \dot{\Delta}(\tau) e^{-\frac{t-\tau}{\tau_d}} d\tau \quad (9)$$

The dynamic force  $f_x$  is then obtained by plugging equation (9) into (4),

$$f_x = f_s(\Delta) \int_0^t \dot{\Delta}(\tau) e^{-\frac{t-\tau}{\tau_d}} d\tau \quad (10)$$

If we assume the insertion speed is constant,  $v$ :

$$f_x = f_s(\Delta) v \tau_d (1 - e^{-\frac{t}{\tau_d}}) \quad (11)$$

Substituting equation (11) into (3) gives the force-deflection response of the model for insertion velocity  $v$  and relaxation constant  $\tau_d$

$$f_n = f_d(\Delta) + f_s(\Delta) v \tau_d (1 - e^{-\frac{\Delta}{v \tau_d}}) \quad (12)$$

Equation (12) shows that we can increase the needle force by increasing insertion speed for a given deflection. This means we can decrease the surface deformation by increasing insertion speed.

Subsequently, we assume that the interaction between needle and tissue as the pressure over the contact area  $A_c$ .

$$p = \frac{f_n}{A_c} \quad (13)$$

In fracture model[81], the tissue penetration after maximum surface deformation is described as a crack extension into the material body, which is also explained as a energy release of crack extension by integrating the change of the energy field,  $J$  integral. Following the  $J$  integral method of[82], we can compute the energy term  $\Pi$  as the difference of the strain energy of the body  $U$  and the external work applied by the needle  $W_e$  as

$$\Pi = U - W_e \quad (14)$$

The nonlinear energy release rate  $J$  for the needle insertion is defined as

$$J = -\frac{d\Pi}{dA} = -\frac{dU}{dA} \quad (15)$$

where  $J$  is the stored energy that the needle can release per unit area of crack extension. Additionally, we assume that there is not displacement during the crack extension, the external work by the needle is zero,  $dW_e=0$ . Defining the crack energy-intensification factor as  $K_c$ , the energy release rate  $J$  can be related to contact pressure by

$$J \propto K_c p^m \quad (16)$$

where  $m$  depends on the nonlinearity of the tissue. Now, if we plug in the equation (13) into (16), then, we can obtain

$$J \propto K_c \left( \frac{f_n}{A_c} \right)^m \quad (17)$$

According to equation (17), we also know that we can increase the crack energy release rate or decrease the surface deformation by not only increasing insertion speed but also increasing the sharpness of the insertion needle.

#### 5.2.5 *Modified Needle guidance method*

As mentioned in previous section, there are several parameters that reduce the surface deformation and we focused on the sharpness of the needle and insertion speed in this work as they were easily modified. As shown in equation (12) and (17), the force for rupture is decreased by faster insertion speed and a smaller contact area (more sharp). For these reasons, we first changed the 34G needle from a blunt-tip to a 45-degree bevel-tip. However, the shaper needle-tip causes a less accurate injection depth, largely due to port position. Therefore, for the purposes of this experimental work, we programmed one more step, “pre-poking” into the motor control stage of insertion. The main purpose is to increase insertion speed as shown in Figure 5.6b and the additional process is shown in Figure 5.4 (red box). Pre-poking with regard to the gelatin matrix refers to controlling the motor to move at its maximum velocity to the prescribed depth relative to the surface. The location of the active line is proportionally determined by the depth of the safety barrier. As shown in Figure 5.6b, the result is that the motor can achieve a much faster insertion speed with greater accuracy and also diminish the “blind zone”.

### 5.3 Results and Discussion

Based on the modified motion guidance algorithm, we conducted three types of experiments to evaluate our micro-injector system: 1) dynamic insertion, 2) multiple gelatin-injections, and 3) ex-vivo bovine eye injection tests.

#### 5.3.1 *Dynamic insertion test*

Similar to the prior work[51], we tested the dynamic targeting ability of our micro-injector system as shown Figure 5.8a. In the prior work, we evaluated the depth-targeting and depth-locking abilities of the system. In this test, however, we intended to evaluate the system performance under the condition that has interaction between tool-tip (34G, 45-degree bevel-tip needle) and the sample material (10% gelatin); specifically, the friction and deformation of the gelatin surface caused by the needle motion and friction. With the modified motion guidance method, there is no blind area and we can see a steep slope for the pre-poking step followed by a gentle slope for the active approach. The axial depth profile shown in magnified red graph of Figure 5.8a was programmed in advance; specifically, the test was started at -200  $\mu\text{m}$  (under the gelatin surface) and conducted five insertions with 50  $\mu\text{m}$  interval after 1.28 ms depth-locking. Once the needle-tip reached -450  $\mu\text{m}$ , the needle was withdrawn. Depicted are 12 injections and 13 depth-locking events. The RMSE of each trial is shown in the magnified graph in Figure 5.8a. The total average of the RMSE is 3.85  $\mu\text{m}$  and this value is much smaller than the result of the prior test that conducted with floating needle. Thus, the friction between the needle and gelatin decreased the micron-level vibration and was helpful to stabilize the needle tip position. Additionally, the incorporation of fast motion diminishes surface deformation;

as a result, stability was no longer an issue when the needle-tip moved to the next depth-locking position.

### 5.3.2 Multiple injection, Gelatin test

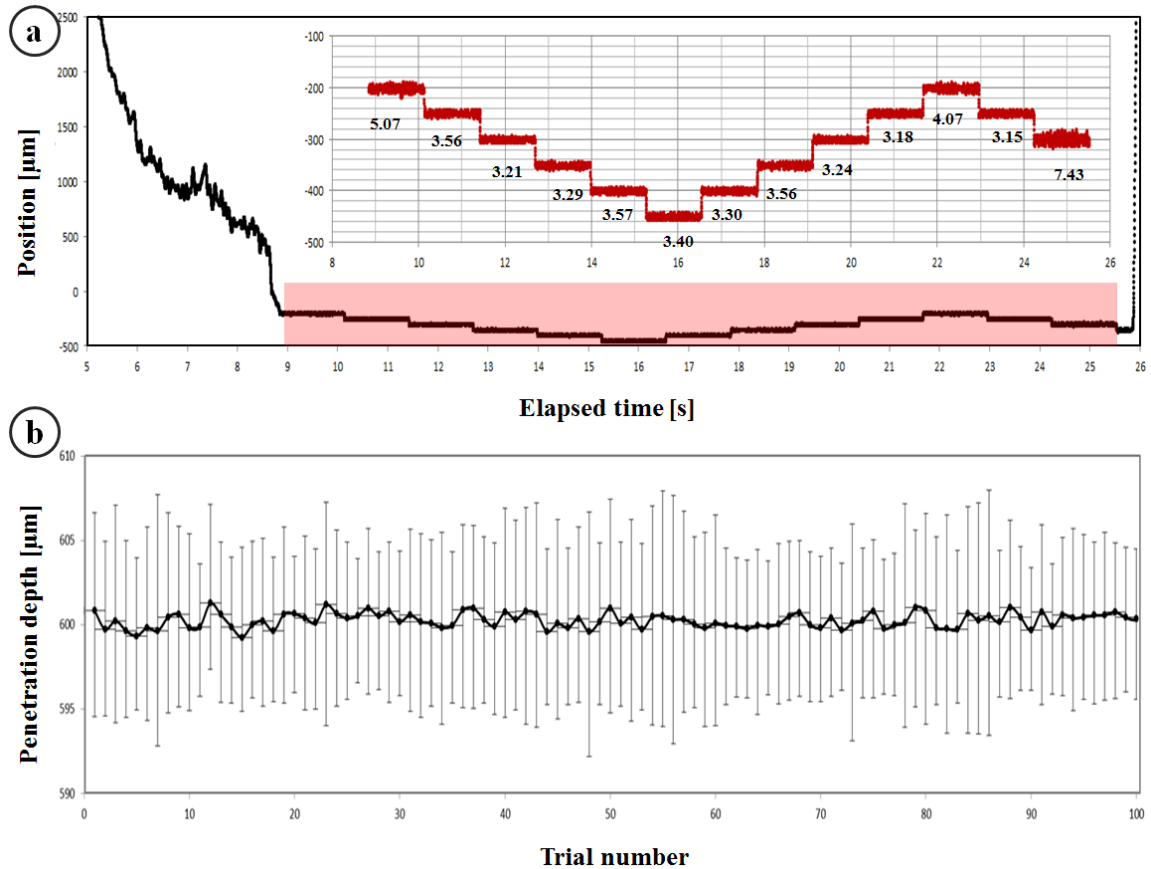


**Figure 5.8. a) Dynamic insertion test under the condition that has interaction between needle-tip and sample material. The upper inserted graph is a partial magnified graph of area in red square in lower entire graph, b) the average deviation error of 100 injections with error bar consisting a positive and negative RMSE.**

Next, we performed a test of multiple injections into gelatin. The experiment was designed to perform multiple injections continuously in order to simulate a potential clinical application in which multiple adjacent injections into a tissue might be

therapeutic. We also test the motion guidance components of our system, which is necessary to recognize the injecting manipulation steps including the approach, locking-in during injection, and withdrawal or reset motions based on the distal information, in addition to the accuracy of the injecting depth. Specifically, one set of tests consisted of 10 consecutive injection trials. In total, we present 10 sets (=100 injections) of trials. The predetermined target injection depth was 600  $\mu\text{m}$ . Like the prior gelatin injection test, the system was programmed to wait for 1 s in order to assure needle tip stability after it attains the target depth. Then, an auditory stimulus informed the user of completion of the injection. Based on the distal information during this depth-locking stage, we can calculate the RMSE to evaluate the accuracy and stability of the system. The result is shown in Figure 5.8b. The measured total mean injecting depth is 600.26  $\mu\text{m}$ . The error bars in the graph are the positive and negative RMSE values. The total average of the RMSE is 5.31  $\mu\text{m}$  and the maximum RMSE is 7.48  $\mu\text{m}$ . This result shows that our SMART injector system can consistently guide the injecting needle.

### 5.3.3 *Ex-vivo bovine eye injection test*

Finally, we performed an *ex-vivo* bovine retina injection test in order to evaluate the effectiveness of the SMART injector system in a biological sample, as shown in Figure 5.9. To preserve the structure of the bovine retina, the experiment was conducted on the same day as death. In this test, we removed cornea, lens and vitreous humor and the needle tip had direct access to the bovine retina. This experimental setup is different from the actual surgical environment that a surgeon performs vitrectomy in so much as it occurs in air and the surgeon operates in fluid. In application, the needle passes through a trocar. The trocar provides both access to the interior of the eye and provides a stabilizing

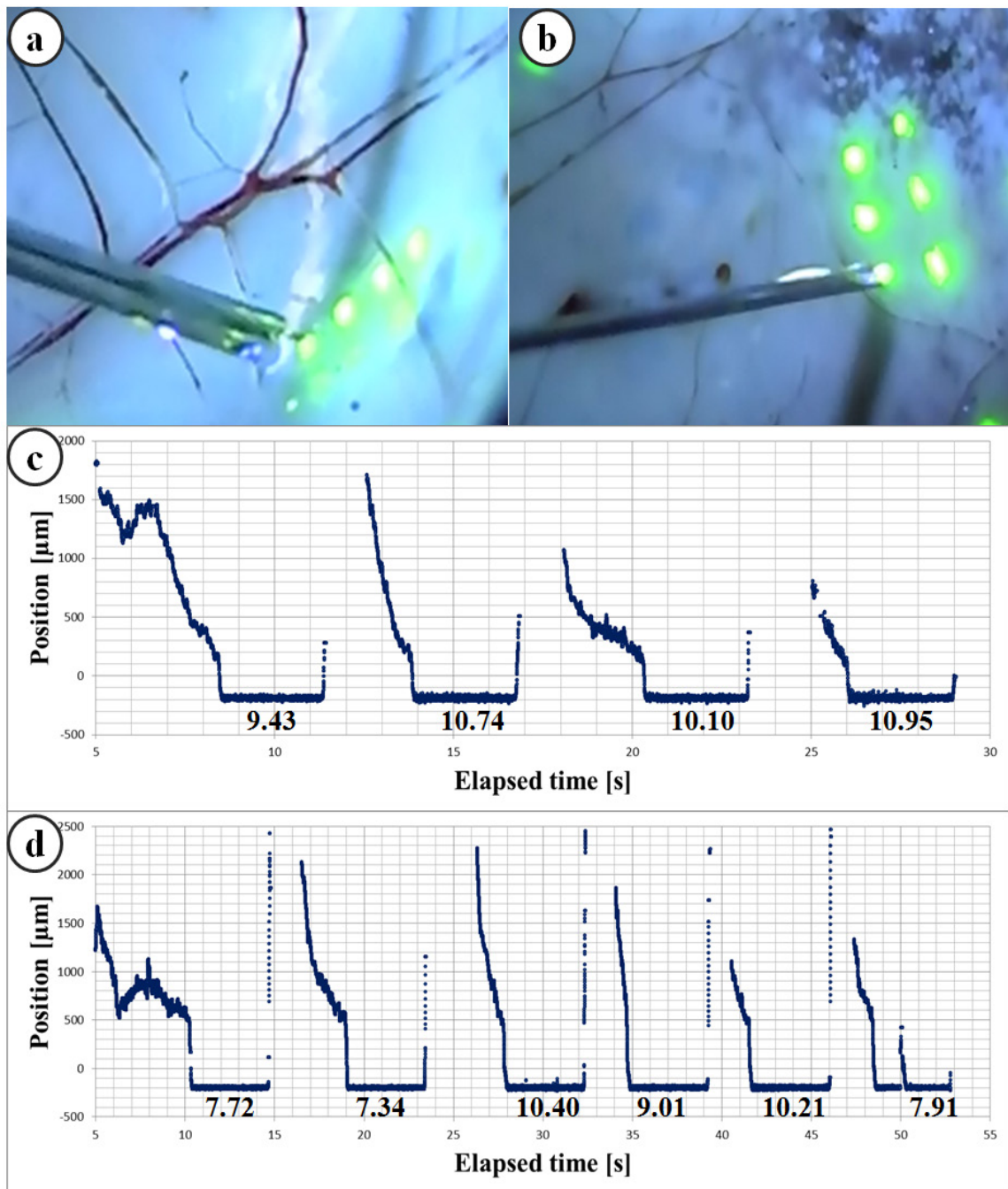


**Figure 5.9.** The ex-vivo bovine eye injection experiment: a) and c) are snap shots displaying the multiple fluorescein injections. Fluorescein was excited by blue light for fluorescence emission, b) tracking data of the needle-tip. Each graph has RMSE below it during the depth-locking.



influence to the tool shaft. Despite these differences the interaction of the SMART with biological tissue provides useful information with regard to tool development and performance. During this test we injected small volumes of fluorescein into bovine retina and illuminated it with a blue light to excite the fluorescein and thereby increase its visibility; as a result, the injected volume is clearly shown in Figure 5.9a and 5.9b. We predetermined the injecting target depth to be 200  $\mu\text{m}$ , as this would constitute an intra-retinal injection in bovine tissue[83]. The intended injecting volume was 50 nL but it was not tightly controlled due to capillary effect. Figure 5.9 shows ten representative injection trials and corresponding distance tracing data. The RMSEs during the depth-locking are shown in the graph. The units of each value are microns. The total average of the RMSE is 9.38  $\mu\text{m}$  and the maximum RMSE is 10.95  $\mu\text{m}$ . Prior knowledge regarding the typical thickness of the human retina and also the spacing between the various well-described layers[58], [59], demonstrates the theoretical potential of SMART injector system to target individual retinal layers.

## 5.4 Conclusion

We have built and demonstrated a handheld OCT guided Sensorized Micromanipulation Aided Robotic-surgery Tool (SMART) that enables accurate depth targeting and precise depth locking during injection. These extended injector functions have the potential to overcome fundamental limitations in current surgical systems. Notable are the solutions to limited depth information through the surgical microscope and limitations in ultra-precise tool control. A simple and intuitive control algorithm for providing multiple injections was devised based on distance information. Additionally, a pre-poking motion

was added to the control system to resolve problems resulting from tissue deformation at the point of needle tissue first contact. To evaluate the performance of the developed system, three types of experiments including dynamic depth targeting, multiple injection, and bovine eye injections were performed. The results of the experiments show that our system accurately guided the needle tip to the target depth and significantly suppressed motion artifacts, while injecting small volumes of fluorescein dye. This hybrid approach to augmenting the surgeon's control and precision represents a significant advance in the development of sensorized surgical tools with augmented haptic functions.

## **CHAPTER 6 : Random transverse motion-induced spatial compounding for fiber bundle imaging**

### **6.1 Introduction**

Imaging systems using fiber optic bundles have been widely used as endoscopes for clinical and scientific applications ranging from imaging of the gastrointestinal tract to imaging brain activity in freely behaving mice[84], [85]. Fiber optic bundles' small diameters, flexibility, and long probe lengths allow easy access to a wide range of body cavities while providing high resolution imaging. Nevertheless, fiber bundle imagers have several inherent limitations due to their physical nature. Fiber optic bundles consist of a large number of cores surrounded by a shared cladding layer as shown in Figure 6.1a. The limitations that degrade image quality include cross talk between adjacent cores and the pixelation effect caused by a lack of images in the cladding layers[86], [87]. In particular, the absence of images in the cladding layers and the resulting pixelation introduce periodic noise that is distributed over the entire image domain and prevents precise image analysis of the object. Many studies have examined ways to eliminate the pixelation noise; most of the early studies were based primarily on low-pass filtering. Because the structural noise is located in the relatively high-frequency region, a low-pass filter such as a Gaussian filter can effectively remove the structural noise[88]–[90]; however, low-pass filtering removes not only the structural noise but also fine structure of the sample; as a result, it causes blurring effect. Instead, several recent studies introduced a method that combines laterally shifted sample images to remove pixelation artifacts and enhance the resolution effectively[91]–[94]. Alternatively, the turbid lens

imaging method has presented a different approach that uses a multimode fiber to avoid pixelation artifacts in endoscopic imaging[95].

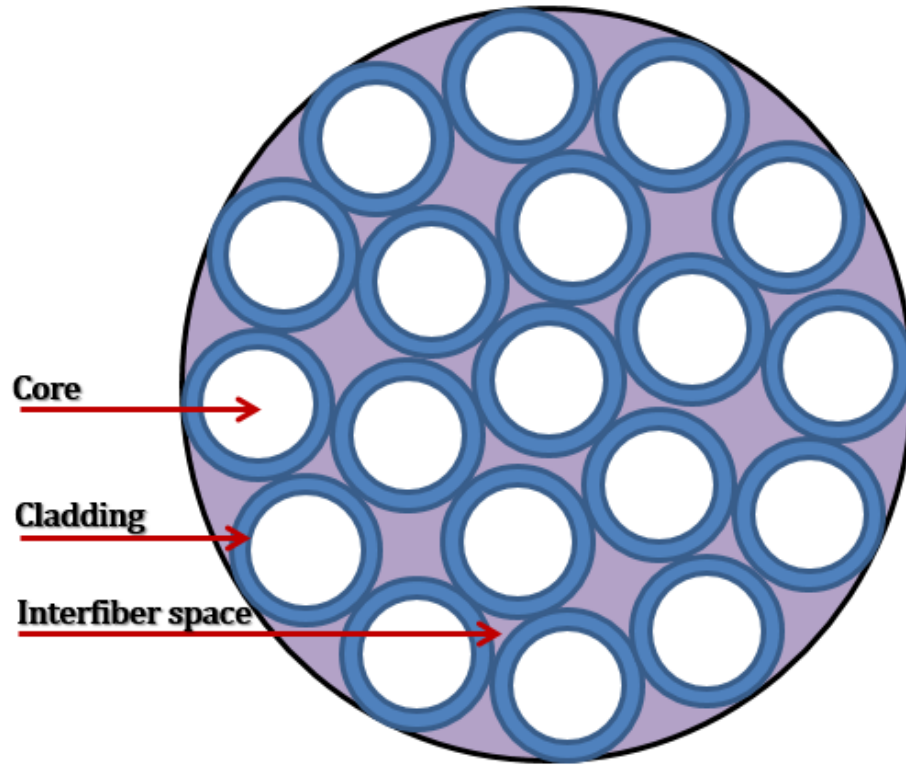


**Figure 6.1. a) Fiber bundle inner structure.**

In this letter, we propose and demonstrate an image registration-based compounding method of eliminating pixelation artifacts to improve the image quality. Compared to previous mechanical[91], [92] or spectral[93] shifting methods, the proposed method, which uses random transverse (or  $XY$ ) motion does not require prefixed sampling points or bulky optics to obtain spatially off-set images. Instead, the proposed method, like the mosaicking method[94], needs to register images from random  $XY$  positions. The mosaicking method, however, requires a long process time for image

registration and is not suitable for real-time imaging. Thus, an efficient registration algorithm is required for real-time image processing to minimize the temporal and spatial variations between sampling intervals. Additionally, pixelation artifacts in fiber bundle images make image registration more difficult because the registration algorithm uses common features existing in the sample images and the structural noise is a very solid common feature of sample images. Thus, cross correlation-based image registration cannot be directly applied to fiber bundle images. In this work, we propose a fast image registration algorithm that uses accurate core area identification and partial image registration based on image entropy[96]. This algorithm is evaluated using a United State Air Force (1951 USAF, Thorlabs, Inc.) target and a mouse brain tissue sample image.

## **6.2 Materials and Methods**

### *6.2.1 System configuration*

As illustrated in Figure 6.2a, the fiber bundle is configured as an epi-fluorescence endoscope that uses a 488-nm excitation light (OBIS488LS, Coherent Inc.). The incident light is reflected by a dichroic mirror (MD499, Thorlabs, Inc.) and coupled into a fiber bundle by a microscope objective (Plan 10X/0.25, Olympus Inc.). The distal end of the fiber consists of two aspheric lens pairs (352140-A, Thorlabs, Inc.) that form a miniaturized objective and enables one-to-one imaging. Returning light from the sample is filtered by a dichroic mirror (FF525-Di01, Semrock, Inc.) and an emission filter (525/39, Thorlabs, Inc.). Spectrally filtered 1280x960 images are acquired by a CCD (GS2-FW-14S5M, Point Grey Research). OpenCV is used for the image processing and a robotic system is used to generate random transverse motion[97].

### 6.2.2 Basic concept of the compounding method

The basic idea of the random transverse compounding is depicted in Figure 2b. Typically, we can acquire successive image stream through CCD or CMOS camera. Adjacent images in the stream shares of most of the part of the images and there is small size of variation spatially. This small size of random inconsistency is useful to make up for the imaging space which is located under the inter-fiber space and cannot be imaged. Additionally, we need to consider the imperfection of the one-to-one matching between fiber core and the sample. In the sampled image, the pixels are related to the fiber core do not show delta function but Gaussian distribution. Moreover, the cross-talk between the cores and defects of the fiber bundle generate additional noise. For these reasons, it is required to discriminate the effective area from the fiber bundle image. This process is also helpful to increase image resolution by removing noise factors. During the

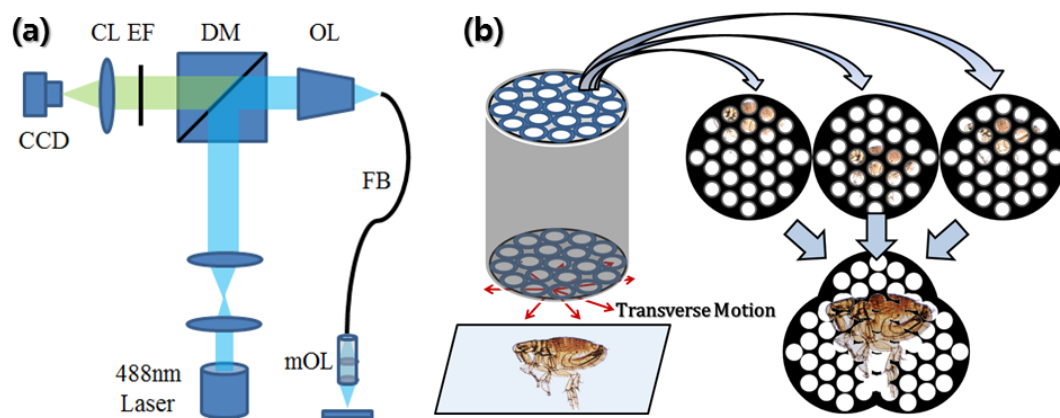


**Figure 6.2. Fiber bundle fluorescence imaging system: (a) system schematic (CL: Condenser lens, EF: Emission filter, DM: Dichroic mirror, OL: Objective lens, FB: Fiber bundle, mOL: miniature-objective lens) and (b) compounding process: transverse-motion-induced images are arranged and compounded to eliminate blank region (pixelation artifact).**

compounding process, we can also acquire multiple pixel data to the same point. The oversampled data is also helpful to increase contrast-to-noise ratio (CNR) by averaging.

### 6.2.3 *Compounding process*

The first step in the proposed method is to distinguish informative pixels from a pixelation artifact in a background image taken without a sample. As mentioned previously, the pixels under the cladding and inter-fiber area impede the image registration. Thus, it is necessary to extract the pixels from the artifact regions to perform registration. Low intensity due to low transmission in the background image indicates that the pixels are located in a defective area or outside of the cores. A threshold is applied to the extraction to determine the boundary between the signal and noise areas because the intensity distribution from a single core is Gaussian in shape[98]. As a result, this process determines the cause of low pixel intensity in the subsequent sample images, whether it results from sample absorption (informative) or low transmission (uninformative). Figure 6.3a–c shows a series of processes for extracting the informative pixels (cores) in the sample image. The coordinates of the black pixels in Figure 6.3a are used to filter uninformative pixels out of the sample image as shown in Figure 6.3b. Figure 6.3c shows the resulting image in the extraction process. White is used to display the artifact regions in Figure 6.3c to show the extraction result but the actual pixel values in the program are zero (black).

Next, the first image obtained from sample imaging is set as a reference image after the imaging probe is located at the region of interest (ROI), and subsequent images are aligned and compounded on the basis of this reference image. For fast and automated image registration, the subsection of the reference image including the most identifiable

feature is selected as a template using the entropy calculation[96] and compared with subsequent sample images instead of using the entire image. In information theory, entropy is the measure of the amount of information and we can find the most characteristic sub-image using entropy. However, we still restrict the ROI area within a predetermined boundary from the center position of the image because we basically assume that a user moves the fiber bundle imager to locate the sample in the middle of image. The equation to calculate the entropy is

$$H(X) = -\sum_{i=1}^N P(x_i) \log_b P(x_i) \quad (1)$$

where  $i$  and  $x_i$  are the pixel index and value in effective area. In our case,  $P$  is probability mass function because the pixel value is discrete and we calculated it by calculating a ratio of the pixel intensity in the total histogram. The parameter,  $b$ , is the base of the logarithm and we used two, which is commonly referred to as bits. A larger template is preferable for accurate registration, but at the cost of an exponential increase in the processing time. Therefore, in our test, a  $256 \times 256$  pixel template was used.

The relative locations of the two images are identified both by calculating the cross-correlation and finding the specific coordinates that yield the maximum cross-correlation value; the normalized cross-correlation is defined as

$$f * g = \frac{1}{N} \sum_{(i,j) \in ROI} \frac{(f(i,j) - m_f)(g(i,j) - m_g)}{\sigma_f \sigma_g} \quad (2)$$

where  $f(x,y)$  and  $g(x,y)$  are the gray scale functions for the  $x$  and  $y$  coordinates in reference and sample images, respectively. Further,  $m$  is the mean value and  $\sigma$  is the standard deviation value of the image intensity in the ROI. Here, the ROI consists of effective pixels, which is selected using background image without a sample.



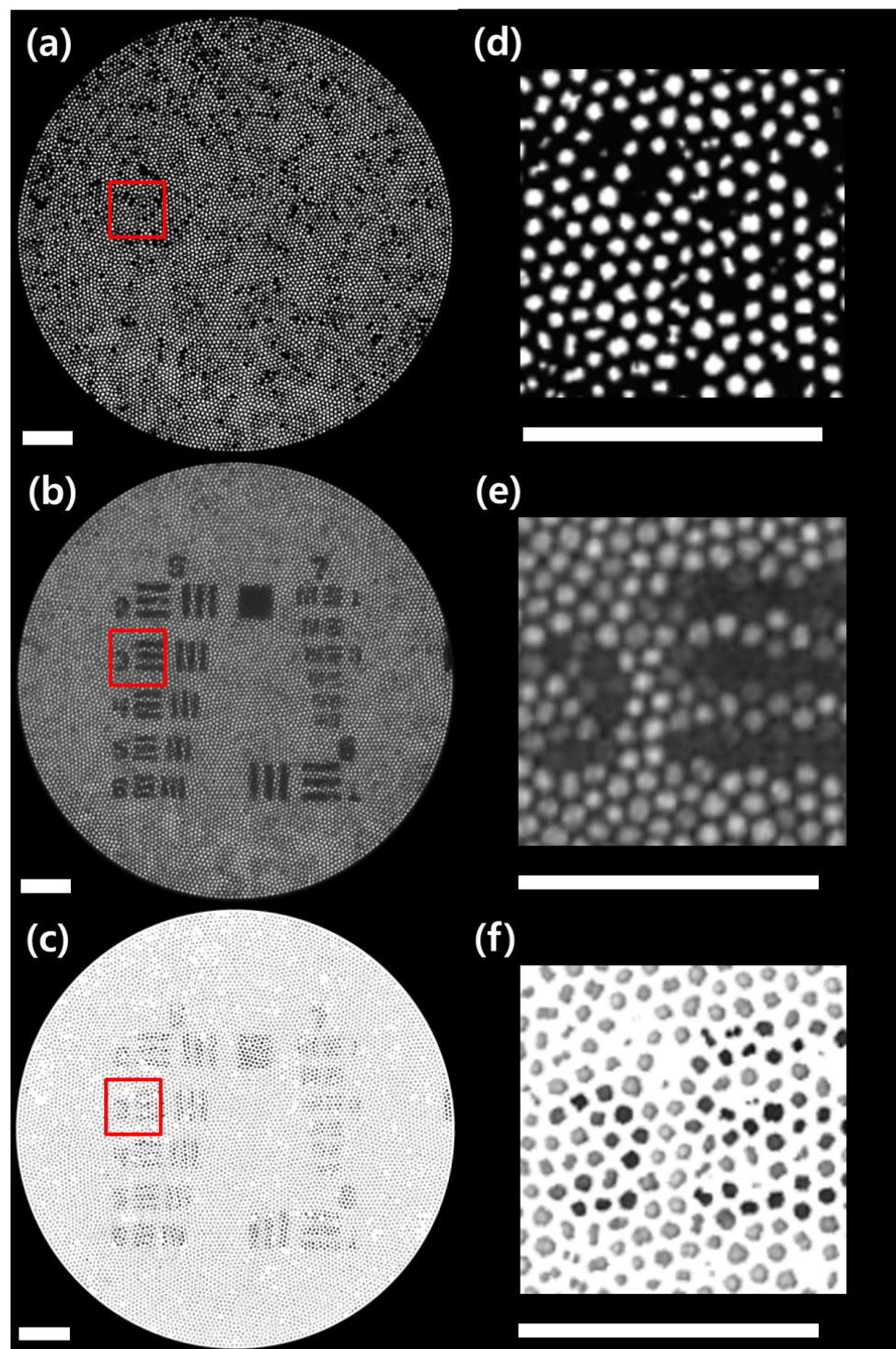


**Figure 6.3.** Process for extracting available pixels: (a) background image after thresholding, (b) original fiber bundle image, (c) available pixels extracted by applying (a) to (b), and (d)–(f) magnified images of the square area in (a)–(c). Scale bar represents 50 $\mu$ m.

The calculation of the cross-correlation between images generally requires a long computation time. Using equation (2) directly in a program script decreases the efficiency because it requires three iterations to calculate the mean, standard, deviation, and cross-correlation sequentially. To improve the performance, the equation can be modified as [52]

$$f * g = \frac{S_{fg} - \frac{2S_f S_g}{N} + \frac{S_f S_g}{N^2}}{\sqrt{\left(S_f^2 - \frac{S_f^2}{N}\right)\left(S_g^2 - \frac{S_g^2}{N}\right)}} \quad (3)$$

$$S_x = \sum_{(i,j) \in ROI} x(i,j)$$

The modified equation (3) requires only a single iteration to calculate the cross-correlation. Consequently, the average program execution time can be reduced up to 40% by using equation (3).

In addition to the improvement in the cross-correlation calculation, an improvement in the overall processing efficiency—and thus a significant time saving—can also be achieved by using an efficient image cross-correlation peak search method to identify the template area. Because the positional difference between two subsequent images is small, we can reduce the search range to the region surround the selected template center according to the scanning speed, camera speed, and processing time. Further, there is no need to calculate all the cross-correlation values by shifting an image pixel by pixel to locate the position with the maximum cross-correlation value. Because the cross-correlation value changes gradually around the peak, we can divide the search area into several subsections and calculate the cross-correlation value of the center position in each subsection. Once the subsection having the highest cross-correlation

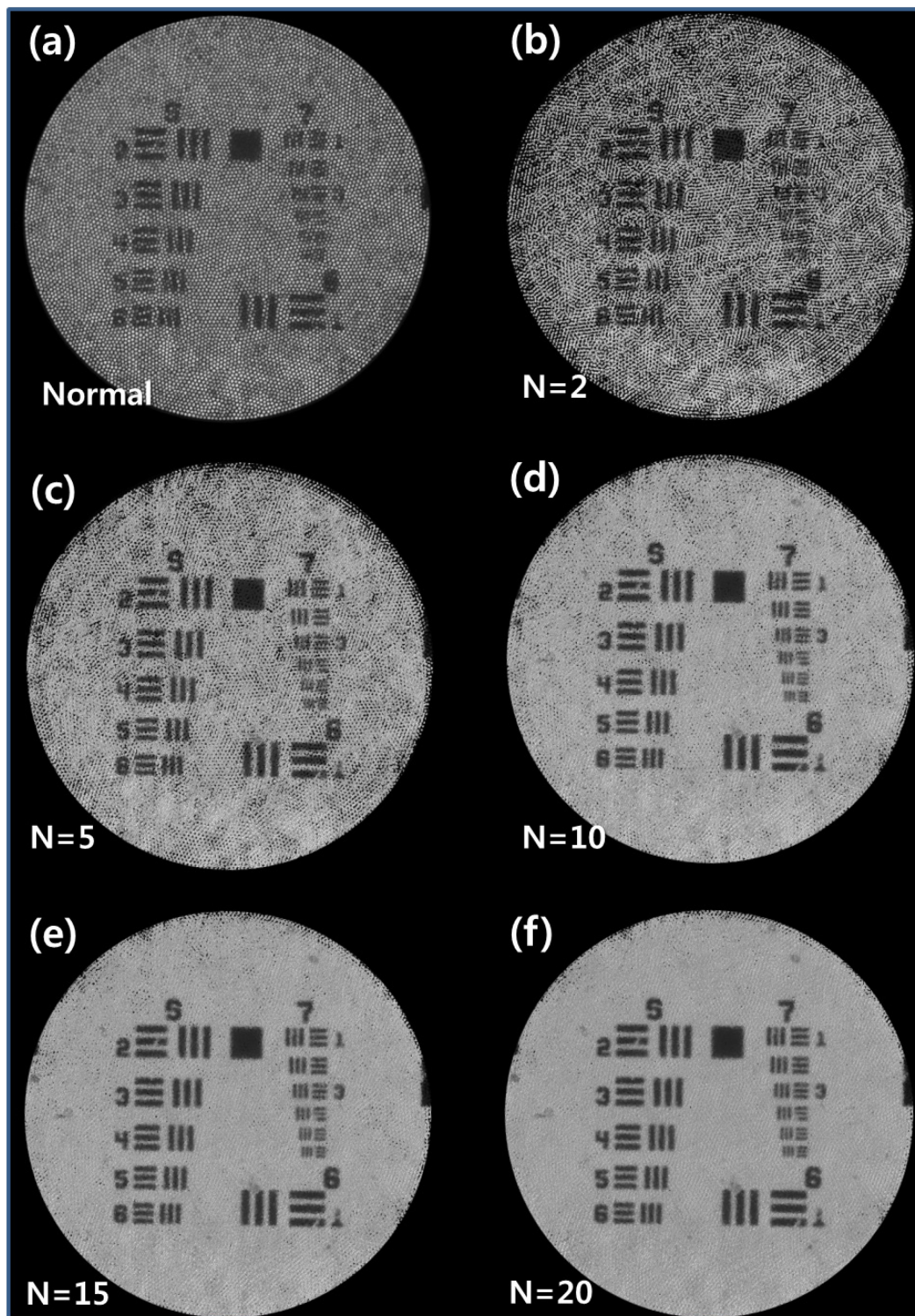


Figure 6.4. Obtained USAF target images: (a) original image, (b)–(f) compounded images using different numbers of sample images.

coefficient has been identified, a subsequent search requires image shifts within the selected section. In the actual implementation, the search zone size was  $128 \times 128$  pixels. This would normally require 16,384 cross-correlation operations to find the peak position. Instead, we divided the search area into 256 subsections each  $16 \times 16$  pixels in size and conducted an additional 256 operations after finding the subsection with the maximum value. Thus, only 512 cross-correlation operations were needed in total to find the peak. Finally, we used a multi-thread technique to maximize the computer performance. All 256 threads were created and processed simultaneously.

The final step of the proposed method involves merging two images. There are two possible cases in the merge process: the presence of a new image in the empty pixels of the cladding area, and the continuing presence of the same information. In the former case, the pixels can contribute to improving the resolution of the compounded image. The latter case is oversampling; we averaged the oversampled images, which can be beneficial in improving the signal-to-noise ratio (SNR) and CNR level. The improved contrast level clarifies the boundary of an object and contributes to the resolution enhancement as well.

## 6.3 Results and Discussion

### 6.3.1 USAF target test

Figure 6.4 shows the result of the proposed compounding technique using a USAF target. The fiber bundle (FIGH-10-500N, Fujikura) used in the test consists of 10,000 fibers with a  $4.6 \mu\text{m}$  spacing for each  $2.9\text{-}\mu\text{m}$ -diameter core. The ROI in the USAF target was groups 6 and 7. The line period of the ROI ranged from  $7.81 \mu\text{m}$  for element 1 in group 6 to  $2.19$

$\mu\text{m}$  for element 6 in group 7. Figure 6.4a is the original fiber bundle image, and Figure 6.4b-f show compounded images using different numbers of images. It took 6.84 ms on average to compound one image using an Intel® Core™ i7-3770K CPU. Up to 20 images were used to compound of a single frame. The image quality was compared with that of a conventional Gaussian filtered image and evaluated in terms of the contrast-to-noise ratio (CNR), global SNR, equivalent number of looks (ENL),  $\beta$ -parameter (which indicates how much the sharpness has degraded due to denoising), and image resolution[99], [100].

$$CNR = 10 \log \left[ \frac{\mu - \mu_b}{\sqrt{\sigma^2 + \sigma_b^2}} \right] \quad (4)$$

$$SNR_g = 10 \log_{10} \left[ \frac{\max(X_{lin})^2}{\sigma_{lin}^2} \right] \quad (5)$$

$$ENL = \frac{\mu_m^2}{\sigma_m^2} \quad (6)$$

$$\beta = \frac{\sum (x_i - m_x)(y_i - m_y)}{\sqrt{\sum (x_i - m_x)^2 \sum (y_i - m_y)^2}} \quad (7)$$

where  $\mu$ ,  $\sigma$ ,  $\mu_b$ ,  $\sigma_b$  in equation (4) are the mean of the pixel values and standard deviation in the ROI of sample and background images, respectively. In equation (5),  $X_{lin}$  is the two-dimensional matrix of pixel values in sample image on a linear intensity scale and  $\sigma_{lin}$  is the noise standard variation on a linear intensity scale.  $\mu_m$ ,  $\sigma_m$  in equation (6) are the mean of the pixel values and standard deviation in the ROI of sample image. In equation (7),  $x_i$ ,  $y_i$ ,  $m_x$ ,  $m_y$  are the  $i$ th pixel values and mean values of sample and reference image.



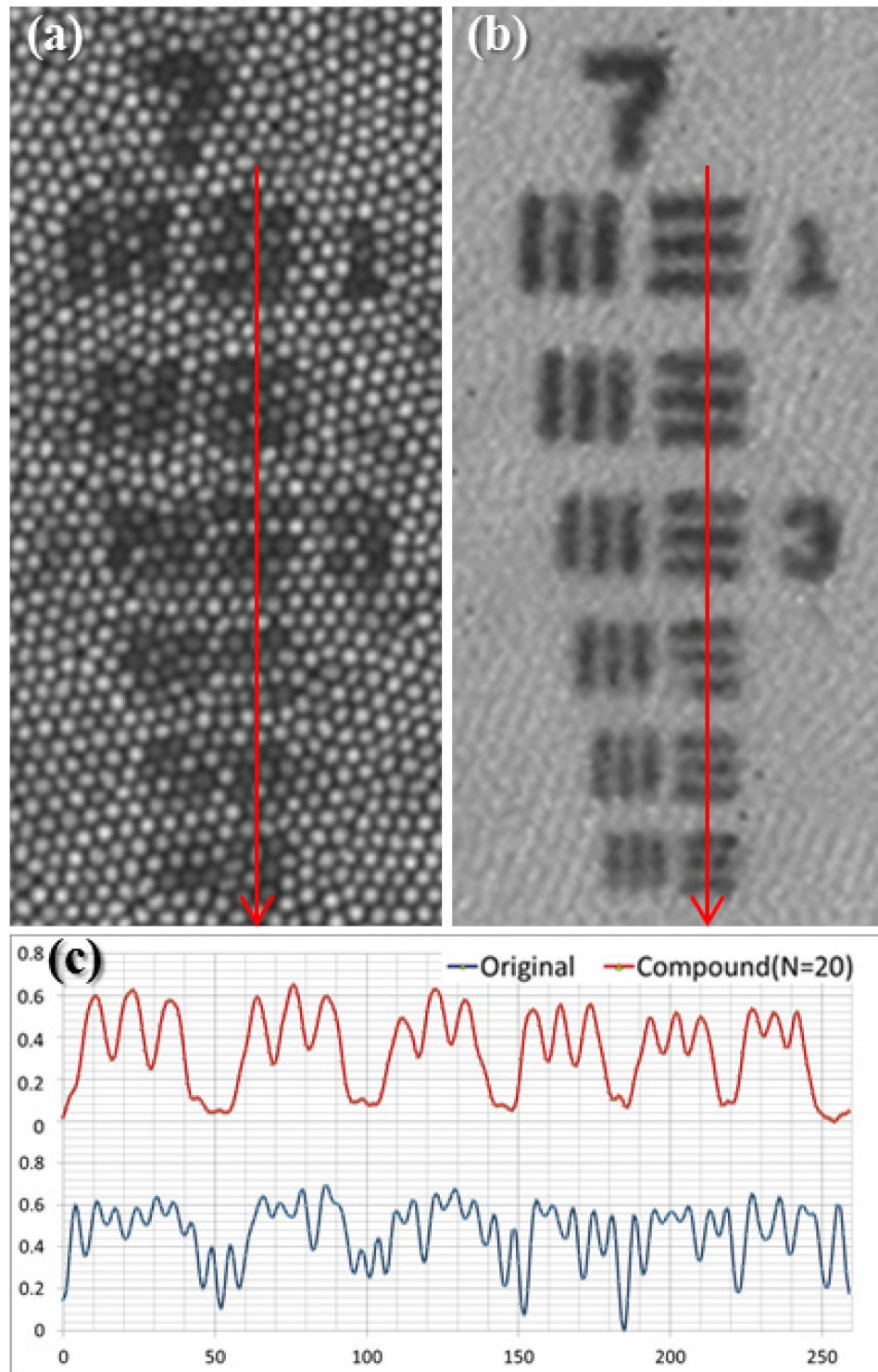


**Figure 6.5. Resolution test: (a) group 7, original image, (b) group 7, compounded image ( $N=20$ ), and (c) intensity variation graphs of pixels along the arrows.**

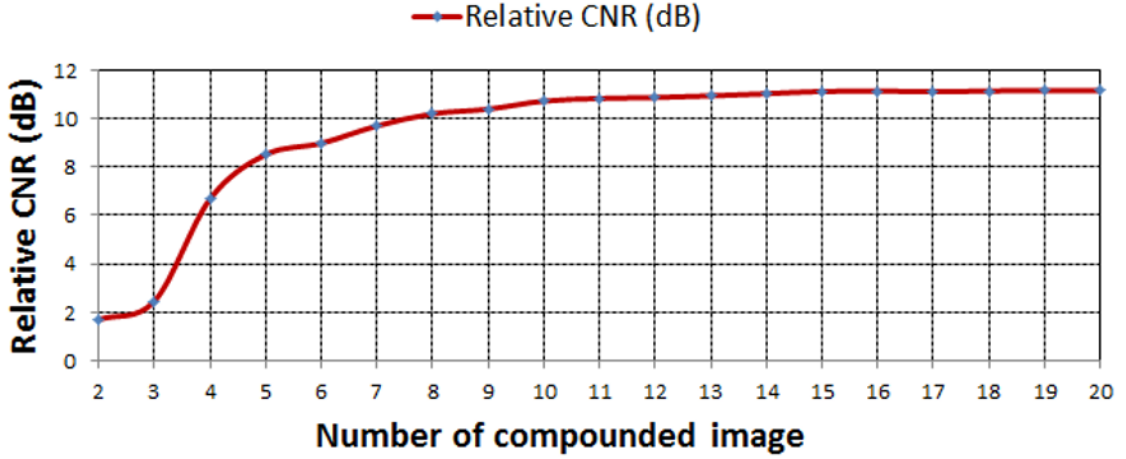


**Figure 6.6. Relative CNR improvement graph by increasing the number of compounding. The first image only consisting of effective pixels (not compounded) was used for reference image to calculate the relative CNR.**

The resolution enhancement is illustrated in Figure 6.5, and the image quality parameters are summarized in Table. 1. The CNR and global SNR of the initial compounded image were lower than those of the original image, as shown in Table 1. This is because our method used only a portion of pixels, as shown in Figure 6.4(b); however, the image quality increased as the compounding iteration increased and surpassed that of the Gaussian-filtered image. The ENL and  $\beta$ -parameter, which describe the homogeneity of the image and noise reduction and the sharpness of the image, respectively, were also improved (a smaller value indicates a sharper image) by image compounding. Because all the elements in group 6 were clearly resolved in the original image, we selected group 7 for the resolution test; a compounded image using 20 sample images was selected for comparison. Figure 6.5a and 6.5b show the target images without and with spatial compounding, respectively. We plotted a line scan to show the intensity profile across the red arrows in each image. For the plotting, the two images were first normalized, and the values were inverted to depict the intensity variations. Figure 6.5c

shows that all three lines in all the elements of group 7 were clearly distinguishable when spatial compounding was applied. In contrast, the line in the uncompounded original image could be resolved only up to the sixth element in group 6, which corresponds to a resolution of 4.39  $\mu\text{m}$ . Because the lines in the sixth element in group 7 can be resolved easily, the resolution is better than 2.19  $\mu\text{m}$ . We were able to overcome the physical fiber pixel size considering that the core size of a single fiber is 2.9  $\mu\text{m}$ .

The iteration number in compounding process determines the improvement of the image quality. Larger number of iteration is likely to make better quality of image; at the same time, however, it requires more sampling time and causes low frame rate. As a result, there is a tradeoff between image quality and sampling rate. Sampling rate is critical factor when it comes to moving sample. Thus, we measured the relative CNR of the compounded images as shown in Figure 6.6. It shows that there is huge improvement of CNR in the 4<sup>th</sup> compounding process and it is saturated around 7<sup>th</sup> compounding. In practical case, we can adjust the compounding number selectively depending on the requirement of the application.

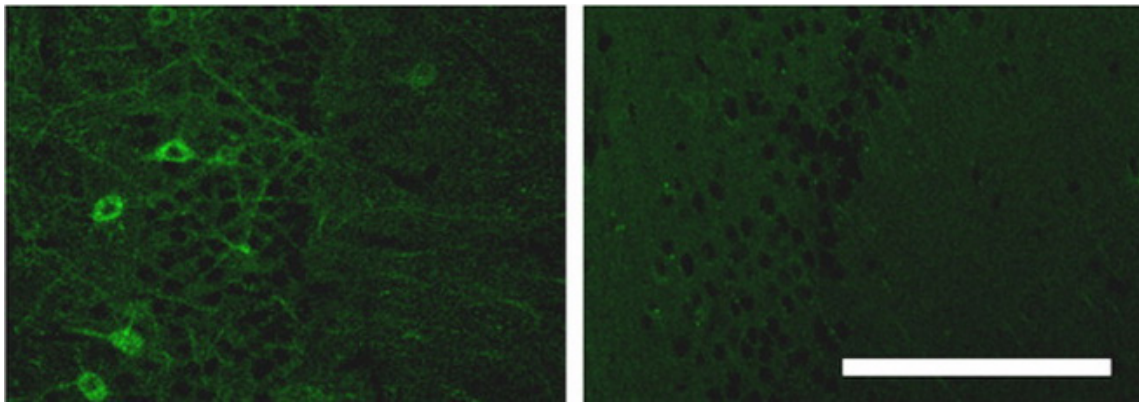


**Figure 6.7. Microscope images of pyramidal cell. Scale bar represent 50  $\mu\text{m}$ .**



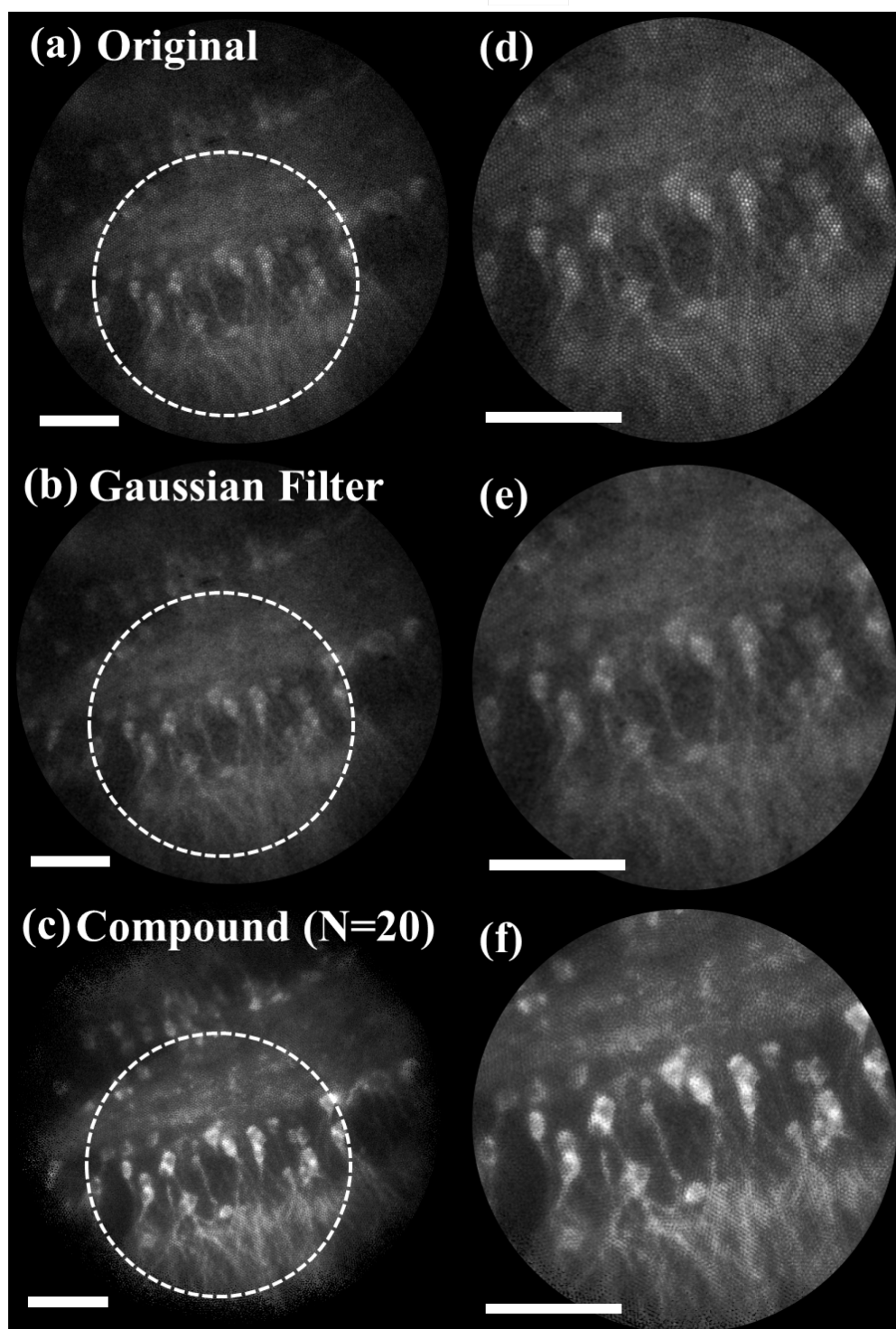


**Figure 6.8.** Pyramidal cell imaging results: (a) original fiber bundle image, (b) Gaussian-filtered image, (c) compounded image using 20 sample images, (d)–(f) magnified image of area in dotted white circle in (a)–(c). Scale bar represents 50  $\mu\text{m}$ .

### 6.3.2 Biological sample imaging (Pyramidal cell)

We also evaluated the proposed algorithm using a biological sample, pyramidal cell as shown in Figure 6.7. The processing time for this case was 6.27 ms per frame on average. Figure 6.8 shows fluorescence images of hippocampal pyramidal neurons from a mouse brain. The cells are fixed and immunostained by a green fluorescent calcium indicator. Figure 6.8a is the unprocessed image taken using the system described in Figure 6.2a. As more subsequent images were compounded, the background noise was suppressed; the improvements in the image quality can be clearly observed [compare Figure 6.8d–f and see Table 1]. As a result, individual neurons and their axons are clearly distinguished and visible in the final compounded image. This demonstrates that the proposed compounding method can be effective and useful for a wide range of biomedical imaging.

**Table 1. Image quality parameters**

<b>USAF target</b>				
Image	CNR (dB)	gSNR (dB)	ENL	$\beta$
Original	3.962	15.767	4.839	1
Gaussian	7.730	21.728	8.783	0.786
Com, #01	-6.150	-1.761	8.838	0.460
Com, #05	4.566	14.588	4.301	0.383
Com, #10	8.207	21.650	8.715	0.490
Com, #15	8.902	23.215	10.19	0.563
Com, #20	8.949	23.223	10.20	0.606
<b>Pyramidal cell</b>				
Image	CNR (dB)	gSNR (dB)	ENL	$\beta$
Original	0.212	19.025	6.703	1
Gaussian	3.011	25.280	12.53	0.866
Com, #01	0.657	11.324	3.103	0.755
Com, #05	6.394	20.430	7.714	0.735
Com, #10	8.058	22.940	9.914	0.692
Com, #15	9.014	24.250	11.30	0.690
Com, #20	9.791	25.259	12.50	0.653

## 6.4 Conclusion

In summary, we proposed and demonstrated an image compounding method to overcome the inherent limitations of fiber-bundle-based imaging. To achieve real-time imaging even when a structural artifact exists, we proposed and optimized an image registration process and achieved a 6.27 ms processing time for 1-frame compounding or 7.97 frames per second for 20-frame compounding in biological sample imaging. The number of images compounded and total frame rate are adjustable depending on the experimental requirements. With the USAF target test, we verified that the method is highly effective in removing the pixelation artifact and improving the image resolution; this resulted in improvements in CNR, global SNR, ENL,  $\beta$ -parameter and resolution in the compounded image. For handheld endoscopic imaging with a live animal, the physiological motion of the animal and the hand would provide the transverse motion required for this method; alternatively, the imaging probe can be dithered using a mechanical motor.

## CHAPTER 7 : CONCLUSIONS

In this Chapter, the technical achievements and contribution of this dissertation are summarized along with some discussion of future research directions.

### 7.1 Summary of Contributions

In this dissertation, a real-time micron-order precision distal sensor based on CP-SSOCT was implemented and applied to two representative microsurgical tools, micro-forceps and micro-injector, for studying depth guided microsurgery. We have evaluated the distal sensor in a dry phantom and in biological specimens possessing a multi-layered tissue structure. The performance was first evaluated using an established dry phantom consisting of stacked cellophane tape. This was followed by evaluation in an *ex-vivo* bovine retina model to assess system accuracy and precision. The results demonstrated highly accurate depth targeting with less than 5  $\mu\text{m}$  RMSE depth locking.

Then, we developed two ocular microsurgical tools based on the OCT distal sensor for retina surgery. The retina is an ideal model in which to assess the ability to use a derivative technology such as a micro-forceps system to precisely peel the epithelial layer of retina and a high precision micro-injector system to accurately place potentially therapeutic agents in previously inaccessible retinal layers. In micro-forceps application, one of the key innovations of this tool is that it separates and independently controls the motion compensation and grasping motion of the forceps. To achieve this, we used two independently actuated motors and controlled the grasping electronically via a touch sensor rather than the mechanical squeezing mechanism on the standard forceps tools. This touch sensor-based actuation enabled the operator to grasp motion by applying less force on the tool handle and eliminated the squeeze induced motion artifact during the

grasping. The touch sensor alone represents a substantial improvement in instrument control and precision. The results show that our touch-sensor-based and motor-actuated grasping mechanism can significantly attenuate the mean motion artifact. Upon activating the CP-SSOCT based depth locking feature, the mean erroneous tool-tip motion was  $5.11\mu\text{m}$ . We conducted a grasping test with 125 $\mu\text{m}$ -diameter-fiber pieces in order to evaluate the device performance by comparing the elapsed time to grasp, the number of tries, and maximum damaged depth to the substrate during the grasping attempts with and without the Motion Guided Micro-Forceps (MGMF) function. The result indicates that all metrics were improved when using MGMT; of note, the average elapsed time, the number of tries, and the maximum depth of damage were improved by 1.32, 1.45, 3.98 times, respectively.

In micro-injector application, we have built and demonstrated a handheld OCT guided **S**ensorized **M**icromanipulation **A**ided **R**obotic-surgery **T**ool (SMART) that enables accurate depth targeting and precise depth locking during injection. These extended injector functions have the potential to overcome fundamental limitations in current surgical systems. Notable are the solutions to limited depth information through the surgical microscope and limitations in ultra-precise tool control. A smart motion control algorithm was developed to achieve real-time, high precision, and intuitive freehand control that allows micron-order-precision injection. Additionally, a pre-poking motion was added to the control system to resolve problems resulting from tissue deformation at the point of needle tissue first contact. To evaluate the performance of the developed system, three types of experiments including dynamic depth targeting, multiple injection, and bovine eye injections were performed. SMART micro-injector

performance was evaluated via dynamic depth targeting, and assessment of multiple consecutive injections with fluorescein dye in the *ex-vivo* bovine eye. The results validated the SMART injector's ability to precisely guide and lock-in the needle-tip to the target depth, during injection. The *ex-vivo* evaluation tests demonstrate that SMART injector can consistently guide the injecting needle to the desired depth and is able to maintain the position with 9.38  $\mu\text{m}$  average RMSE, during injection of 50 nL of fluorescein dye. The results of the experiments show that our system accurately guided the needle tip to the target depth and significantly suppressed motion artifacts, while injecting small volumes of fluorescein dye. This hybrid approach to augmenting the surgeon's control and precision represents a significant advance in the development of sensorized surgical tools with augmented haptic functions.

## **7.2 Future Work**

In the next step, it is required to evaluate the developed technology in more realistic condition such as live animal experiment. So far, we developed and verified the depth guidance technology; however, we need more study about how the proposed new technology can seamlessly interact with actual surgeons since the final customer of the new technology is none other than the surgeons.

## BIBLIOGRAPHY

- [1] S. P. N. Singh and C. N. Riviere, "Physiological tremor amplitude during retinal microsurgery," in *Proceedings of the IEEE 28th Annual Northeast Bioengineering Conference*, 2002, pp. 171–172.
- [2] M. Patkin, "Ergonomics applied to the practice of microsurgery," *Aust. N. Z. J. Surg.*, vol. 47, no. 3, pp. 320–329, 1977.
- [3] R. H. Taylor, P. Jensen, L. Whitcomb, A. Barnes, R. Kumar, D. Stoianovici, P. Gupta, Z. Wang, E. DeJuan, and L. Kavoussi, "A Steady-Hand Robotic System for Microsurgical Augmentation," *Int. J. Rob. Res.*, vol. 18, no. 12, pp. 1201–1210, 1999.
- [4] R. H. Taylor and D. Stoianovici, "Medical Robotics in Computer-Integrated Surgery," *IEEE Trans. Robot. Autom.*, vol. 19, no. 5, pp. 765–781, 2003.
- [5] C. N. Riviere, J. Gangloff, and M. De Mathelin, "Robotic compensation of biological motion to enhance surgical accuracy," in *Proceedings of the IEEE*, 2006, vol. 94, no. 9, pp. 1705–1715.
- [6] T. Ueta, Y. Yamaguchi, Y. Shirakawa, T. Nakano, R. Ideta, Y. Noda, A. Morita, R. Mochizuki, N. Sugita, M. Mitsuishi, and Y. Tamaki, "Robot-Assisted Vitreoretinal Surgery. Development of a Prototype and Feasibility Studies in an Animal Model," *Ophthalmology*, vol. 116, no. 8, p. 1538–1543.e2, 2009.
- [7] I. Kuru, B. Gonenc, M. Balicki, J. T. Handa, P. L. Gehlbach, R. H. Taylor, and I. I. Iordachita, "Force sensing micro-forceps for robot assisted retinal surgery," in *Proceedings of the 34th Annual International Conference of the IEEE Engineering*

- in Medicine and Biology Society, EMBS*, 2012, pp. 1401–1404.
- [8] B. Gonenc, J. T. Handa, P. L. Gehlbach, R. H. Taylor, and I. I. Iordachita, “Design of 3-DOF force sensing micro-forceps for robot assisted vitreoretinal surgery,” in *Proceedings of the 35th Annual International Conference of the IEEE Engineering in Medicine and Biology Society, EMBS*, 2013, pp. 5686–5689.
  - [9] H. Yu, J.-H. Shen, R. J. Shah, N. Simaan, and K. M. Joos, “Evaluation of microsurgical tasks with OCT-guided and/or robot-assisted ophthalmic forceps,” *Biomed. Opt. Express*, vol. 6, no. 2, pp. 457–472, 2015.
  - [10] C. N. Riviere and N. V. Thakor, “Modeling and canceling tremor in human-machine interfaces,” *IEEE Eng. Med. Biol. Mag.*, vol. 15, no. 3, pp. 29–36, 1996.
  - [11] C. N. Riviere, W. T. Ang, and P. K. Khosla, “Toward Active Tremor Canceling in Handheld Microsurgical Instruments,” *IEEE Trans. Robot. Autom.*, vol. 19, no. 5, pp. 793–800, 2003.
  - [12] W. T. Ang, P. K. Pradeep, and C. N. Riviere, “Active tremor compensation in microsurgery,” in *Proceedings of the 26th Annual International conference of IEEE Engineering in Medicine and Biology Society, EMBS*, 2004, vol. 1, pp. 2738–2741.
  - [13] R. A. MacLachlan, B. C. Becker, J. C. Tabarés, G. W. Podnar, L. A. Lobes, and C. N. Riviere, “Micron: An actively stabilized handheld tool for microsurgery,” *IEEE Trans. Robot.*, vol. 28, no. 1, pp. 195–212, 2012.
  - [14] S. Yang, M. Balicki, R. a. MacLachlan, X. Liu, J. U. Kang, R. H. Taylor, and C. N. Riviere, “Optical coherence tomography scanning with a handheld vitreoretinal micromanipulator,” in *Proceedings of the 34th Annual International Conference of*



- the IEEE Engineering in Medicine and Biology Society, EMBS*, 2012, pp. 948–951.
- [15] S. Yang, M. Balicki, T. S. Wells, R. A. MacLachlan, X. Liu, J. U. Kang, J. T. Handa, R. H. Taylor, and C. N. Riviere, “Improvement of Optical Coherence Tomography using Active Handheld Micromanipulator in Vitreoretinal Surgery,” in *Proceedings of the 35th Annual International Conference of the IEEE Engineering in Medicine and Biology Society, EMBS*, 2013, pp. 5674–5677.
  - [16] C. J. Payne, H. J. Marcus, and G.-Z. Yang, “A Smart Haptic Hand-Held Device for Neurosurgical Microdissection,” *Ann. Biomed. Eng.*, 2015.
  - [17] J. P. Ehlers, Y. K. Tao, S. Farsiu, R. Maldonado, J. A. Izatt, and C. A. Toth, “Integration of a spectral domain optical coherence tomography system into a surgical microscope for intraoperative imaging,” *Investig. Ophthalmol. Vis. Sci.*, vol. 52, no. 6, pp. 3153–3159, 2011.
  - [18] P. Hahn, J. Migacz, R. O’Connell, J. a. Izatt, and C. a. Toth, “Unprocessed real-time imaging of vitreoretinal surgical maneuvers using a microscope-integrated spectral-domain optical coherence tomography system,” *Graefe’s Arch. Clin. Exp. Ophthalmol.*, vol. 251, no. 1, pp. 213–220, 2013.
  - [19] P. Hahn, J. Migacz, R. O’Connell, S. Day, A. Lee, P. Lin, R. Vann, A. Kuo, S. Fekrat, P. Mruthyunjaya, E. A. Postel, J. A. Izatt, and C. A. Toth, “Preclinical evaluation and intraoperative human retinal imaging with a high-resolution microscope-integrated spectral domain optical coherence tomography device,” *Retina*, vol. 33, no. 7, pp. 1328–1337, 2013.
  - [20] Y. K. Tao, S. K. Srivastava, and J. P. Ehlers, “Microscope-integrated

- intraoperative OCT with electrically tunable focus and heads-up display for imaging of ophthalmic surgical maneuvers,” *Biomed. Opt. Express*, vol. 5, no. 6, pp. 1877–1885, 2014.
- [21] J. P. Ehlers, S. K. Srivastava, D. Feiler, A. I. Noonan, A. M. Rollins, and Y. K. Tao, “Integrative Advances for OCT-Guided Ophthalmic Surgery and Intraoperative OCT: Microscope Integration, Surgical Instrumentation, and Heads-Up Display Surgeon Feedback,” *PLoS One*, vol. 9, no. 8, 2014.
- [22] J. P. Ehlers, T. Tam, P. K. Kaiser, D. F. Martin, G. M. Smith, and S. K. Srivastava, “Utility of intraoperative optical coherence tomography during vitrectomy surgery for vitreomacular traction syndrome,” *Retina*, vol. 34, no. 7, pp. 1341–1346, 2014.
- [23] K. M. Joos and J.-H. Shen, “Miniature real-time intraoperative forward-imaging optical coherence tomography probe,” *Biomed. Opt. Express*, vol. 4, no. 8, pp. 1342–1350, 2013.
- [24] K. Zhang and J. U. Kang, “Graphics processing unit accelerated non-uniform fast Fourier transform for ultrahigh-speed, real-time Fourier-domain OCT.,” *Opt. Express*, vol. 18, no. 22, pp. 23472–23487, 2010.
- [25] K. Zhang and J. U. Kang, “Real-time intraoperative 4D full-range FD-OCT based on the dual graphics processing units architecture for microsurgery guidance.,” *Biomed. Opt. Express*, vol. 2, no. 4, pp. 764–770, 2011.
- [26] X. Liu, I. I. Iordachita, X. He, R. H. Taylor, and J. U. Kang, “Miniature fiber-optic force sensor based on low-coherence Fabry-Pérot interferometry for vitreoretinal microsurgery,” *Biomed. Opt. Express*, vol. 3, no. 5, pp. 1062–1076, 2012.
- [27] X. Liu, M. Balicki, R. H. Taylor, and J. U. Kang, “Towards automatic calibration

- of Fourier-Domain OCT for robot-assisted vitreoretinal surgery,” *Opt. Express*, vol. 18, no. 23, pp. 24331–24343, 2010.
- [28] J. U. Kang, Y. Huang, K. Zhang, Z. Ibrahim, J. Cha, A. W. P. Lee, G. Brandacher, and P. L. Gehlbach, “Real-time three-dimensional Fourier-domain optical coherence tomography video image guided microsurgeries,” *J. Biomed. Opt.*, vol. 17, no. 8, pp. 81403-1–6, 2012.
- [29] K. Zhang, W. Wang, J. H. Han, and J. U. Kang, “A surface topology and motion compensation system for microsurgery guidance and intervention based on common-path optical coherence tomography,” *IEEE Trans. Biomed. Eng.*, vol. 56, no. 9, pp. 2318–2321, 2009.
- [30] J. U. Kang, J. H. Han, X. Liu, and K. Zhang, “Common-path optical coherence tomography for biomedical imaging and sensing,” *J. Opt. Soc. Korea*, vol. 14, no. 1, pp. 1–13, 2010.
- [31] K. Zhang and J. U. Kang, “Common-path low-coherence interferometry fiber-optic sensor guided microincision,” *J. Biomed. Opt.*, vol. 16, no. 9, p. 95003, 2011.
- [32] Y. Huang, K. Zhang, C. Lin, and J. U. Kang, “Motion compensated fiber-optic confocal microscope based on a common-path optical coherence tomography distance sensor,” *Opt. Eng.*, vol. 50, no. 8, p. 83201, 2011.
- [33] Y. Huang, X. Liu, C. Song, and J. U. Kang, “Motion-compensated hand-held common-path Fourier-domain optical coherence tomography probe for image-guided intervention,” *Biomed. Opt. Express*, vol. 3, no. 12, pp. 3105–3118, 2012.
- [34] C. Song, P. L. Gehlbach, and J. U. Kang, “Active tremor cancellation by a ‘Smart’ handheld vitreoretinal microsurgical tool using swept source optical coherence

- tomography,” *Opt. Express*, vol. 20, no. 21, pp. 23414–23421, 2012.
- [35] C. Song, D. Y. Park, P. L. Gehlbach, S. J. Park, and J. U. Kang, “Fiber-optic OCT sensor guided ‘SMART’ micro-forceps for microsurgery,” *Biomed. Opt. Express*, vol. 4, no. 7, pp. 1045–1050, 2013.
- [36] B. E. A. Saleh and M. C. Teich, *Fundamentals of Photonics, 2nd Edition*. WILEY, 2007.
- [37] S. Van der Jeught, A. Bradu, and A. G. Podoleanu, “Real-time resampling in Fourier domain optical coherence tomography using a graphics processing unit.,” *J. Biomed. Opt.*, vol. 15, no. 3, p. 30511, 2015.
- [38] M. A. Choma, M. V. Sarunic, C. Yang, and J. Izatt, “Sensitivity advantage of swept source and Fourier domain optical coherence tomography,” *Opt. Express*, vol. 11, no. 18, pp. 2183–2189, 2003.
- [39] W.-C. Kuo, C.-M. Lai, Y.-S. Huang, C.-Y. Chang, and Y.-M. Kuo, “Balanced detection for spectral domain optical coherence tomography,” *Opt. Express*, vol. 21, no. 16, p. 19280, 2013.
- [40] A. Bradu and A. G. Podoleanu, “Fourier domain optical coherence tomography system with balance detection,” *Opt. Express*, vol. 20, no. 16, p. 17522, 2012.
- [41] S. Y. Ryu, H. Y. Choi, J. Na, W. J. Choi, and B. H. Lee, “Lensed fiber probes designed as an alternative to bulk probes in optical coherence tomography,” *Appl. Opt.*, vol. 47, no. 10, pp. 1510–1516, 2008.
- [42] K. M. Tan, M. Mazilu, T. H. Chow, W. M. Lee, K. Taguchi, B. K. Ng, W. Sibbett, C. S. Herrington, C. T. Brown, and K. Dholakia, “In-fiber common-path optical coherence tomography using a conical-tip fiber,” *Opt. Express*, vol. 17, no. 4, pp.

2375–2384, 2009.

- [43] J. Kim, J. Han, J. Jeong, and S. Member, “Common-Path Optical Coherence Tomography Using a Conical-Frustum-Tip Fiber Probe,” vol. 20, no. 2, 2014.
- [44] M. Zhao, Y. Huang, and J. U. Kang, “Sapphire ball lens-based fiber probe for common-path optical coherence tomography and its applications in corneal and retinal imaging,” *Opt. Lett.*, vol. 37, no. 23, pp. 4835–4837, 2012.
- [45] R. K. Wang and Z. Ma, “A practical approach to eliminate autocorrelation artefacts for volume-rate spectral domain optical coherence tomography,” *Phys. Med. Biol.*, vol. 51, no. 12, pp. 3231–3239, 2006.
- [46] S. Moon, S.-W. Lee, and Z. Chen, “Reference spectrum extraction and fixed-pattern noise removal in optical coherence tomography,” *Opt. Express*, vol. 18, no. 24, pp. 24395–24404, 2010.
- [47] K.-S. Kim, H.-J. Park, and H. S. Kang, “Enhanced optical coherence tomography imaging using a histogram-based denoising algorithm,” *Opt. Eng.*, vol. 51, no. 11, p. 113110, 2015.
- [48] J. Zhang, J. S. Nelson, and Z. Chen, “Removal of a mirror image and enhancement of the signal-to-noise ratio in Fourier-domain optical coherence tomography using an electro-optic phase modulator,” *Opt. Lett.*, vol. 30, no. 2, pp. 147–149, 2005.
- [49] S. Vergnole, G. Lamouche, and M. L. Dufour, “Artifact removal in Fourier-domain optical coherence tomography with a piezoelectric fiber stretcher,” *Opt. Lett.*, vol. 33, no. 7, pp. 732–734, 2008.
- [50] D. G. Childers, N. W. Perry, and R. S. Varga, “Composite Signal Decomposition,” *IEEE Trans. Audio Electroacoust.*, vol. 18, no. 4, pp. 471–477, 1970.

- [51] G. W. Cheon, Y. Huang, J. Cha, P. L. Gehlbach, and J. U. Kang, "Accurate real-time depth control for CP-SSOCT distal sensor based handheld microsurgery tools," *Biomed. Opt. Express*, vol. 6, no. 5, pp. 1942–1953, 2015.
- [52] K. Briechele and U. D. Hanebeck, "Template matching using fast normalized cross correlation," in *Proceedings of SPIE*, 2001, vol. 4387, pp. 95–102.
- [53] R. E. Kalman, "A New Approach to Linear Filtering and Prediction Problems," *Trans. ASME-Journal Basic Eng.*, vol. 82, no. Series D, pp. 35–45, 1960.
- [54] S.-K. Weng, C.-M. Kuo, and S.-K. Tu, "Video object tracking using adaptive Kalman filter," *J. Vis. Commun. Image Represent.*, vol. 17, pp. 1190–1208, 2006.
- [55] Y. Zheng, S. Chen, W. Tan, R. Kinnick, and J. F. Greenleaf, "Detection of tissue harmonic motion induced by ultrasonic radiation force using pulse-echo ultrasound and Kalman filter," *IEEE Trans. Ultrason. Ferroelectr. Freq. Control*, vol. 54, no. 2, pp. 290–299, 2007.
- [56] S. H. P. Won, F. Golnaraghi, and W. W. Melek, "A fastening tool tracking system using an IMU and a position sensor with Kalman filters and a fuzzy expert system," *IEEE Trans. Ind. Electron.*, vol. 56, no. 5, pp. 1782–1792, 2009.
- [57] R. K. Mudi and N. R. Pal, "A robust self-tuning scheme for PI- and PD-type fuzzy controllers," *IEEE Trans. Fuzzy Syst.*, vol. 7, no. 1, pp. 2–16, 1999.
- [58] A. M. Bagci, M. Shahidi, R. Ansari, M. Blair, N. Paul, and R. Zelkha, "Thickness Profiles of Retinal Layers by Optical Coherence Tomography Image Segmentation," *Am. J. Ophthalmol.*, vol. 146, no. 5, pp. 679–687, 2008.
- [59] D. C. Fernández, H. M. Salinas, and C. a Puliafito, "Automated detection of retinal layer structures on optical coherence tomography images," *Opt. Express*, vol. 13,

- no. 25, pp. 10200–10216, 2005.
- [60] K. T. Kang, K. S. Kim, and Y. C. Kim, “Surgical results of idiopathic and secondary epiretinal membrane,” *Int. Ophthalmol.*, vol. 34, no. 6, pp. 1227–1232, 2014.
  - [61] A. Gandorfer, C. Haritoglou, and A. Kampik, “Toxicity of indocyanine green in vitreoretinal surgery,” *Dev. Ophthalmol.*, vol. 42, pp. 69–81, 2008.
  - [62] J. P. Ehlers, D. Xu, P. K. Kaiser, R. P. Singh, and S. K. Srivastava, “Intrasurgical dynamics of macular hole surgery: an assessment of surgery-induced ultrastructural alterations with intraoperative optical coherence tomography,” *Retina*, vol. 34, no. 2, pp. 213–221, 2014.
  - [63] A. B. Vakhtin, D. J. Kane, W. R. Wood, and K. A. Peterson, “Common-path interferometer for frequency-domain optical coherence tomography,” *Appl. Opt.*, vol. 42, no. 34, pp. 6953–6958, 2003.
  - [64] U. Sharma, N. M. Fried, and J. U. Kang, “All-Fiber Common-Path Optical Coherence Tomography: Sensitivity Optimization and System Analysis,” *IEEE J. Sel. Top. quantum Electron.*, vol. 11, no. 4, pp. 799–805, 2005.
  - [65] G. W. Cheon, P. Lee, B. Gonenc, P. L. Gehlbach, and J. U. Kang, “Active depth-guiding handheld micro-forceps for membranectomy based on CP-SSOCT,” in *Proceedings of SPIE*, 2016, vol. 9702.
  - [66] S. Yang, R. A. Maclachlan, and C. N. Riviere, “Manipulator Design and Operation of a Microsurgical Instrument,” *Trans. MECHATRONICS*, vol. 20, no. 2, pp. 761–772, 2015.
  - [67] Z. Li, J. H. Shen, J. A. Kozub, R. Prasad, P. Lu, and K. M. Joos, “A Miniature

- Forward-imaging B-scan Optical Coherence Tomography Probe to Guide Real-time Laser Ablation,” *Lasers Surg. Med.*, vol. 46, no. 3, pp. 193–202, 2014.
- [68] M. Balicki, J. Han, I. Iordachita, P. Gehlbach, J. Handa, R. Taylor, and J. Kang, “Single Fiber Optical Coherence Tomography Microsurgical Instruments for Computer and Robot- Assisted Retinal Surgery,” *Med Image Compu Assist Interv*, vol. 12, no. 1, pp. 108–115, 2009.
- [69] P. K. Gupta, P. S. Jensen, and E. de Juan Jr, “Surgical forces and tactile perception during retinal microsurgery,” *Lecture Notes in Computer Science*, vol. 1679. pp. 1218–1225, 1999.
- [70] S. E. Boye, S. L. Boye, A. S. Lewin, and W. W. Hauswirth, “A comprehensive review of retinal gene therapy.,” *Mol. Ther.*, vol. 21, no. 3, pp. 509–519, 2013.
- [71] A. V Cideciyan, S. G. Jacobson, W. A. Beltran, A. Sumaroka, M. Swider, S. Iwabe, A. J. Roman, M. B. Olivares, S. B. Schwartz, A. M. Komáromy, W. W. Hauswirth, and G. D. Aguirre, “Human retinal gene therapy for Leber congenital amaurosis shows advancing retinal degeneration despite enduring visual improvement.,” *Proc. Natl. Acad. Sci. U. S. A.*, vol. 110, no. 6, pp. 517–525, 2013.
- [72] W. Wang, X. Liu, D. Gelinas, B. Ciruna, and Y. Sun, “A fully automated robotic system for microinjection of zebrafish embryos,” *PLoS One*, vol. 2, no. 9, p. e862, 2007.
- [73] I. Fleming, M. Balicki, J. Koo, I. Iordachita, B. Mitchell, J. Handa, G. Hager, and R. Taylor, “Cooperative robot assistant for retinal microsurgery,” in *Proceedings of Medical Image Computing and Computer-Assisted Intervention*, 2008, vol. 5242, pp. 543–550.



- [74] T. Ota, N. A. Patronik, D. Schwartzman, C. N. Riviere, and M. A. Zenati, "Minimally Invasive Epicardial Injections using a Novel Semiautonomous Robotic Device," *Circulation*, vol. 118, no. 14, pp. 115–120, 2008.
- [75] B. C. Becker, S. Yang, R. A. MacLachlan, and C. N. Riviere, "Towards vision-based control of a handheld micromanipulator for retinal cannulation in an eyeball phantom," in *Proceedings of the IEEE RAS and EMBS International Conference on Biomedical Robotics and Biomechatronics*, 2012, pp. 44–49.
- [76] B. Gonenc, R. H. Taylor, I. Iordachita, P. Gehlbach, and J. Handa, "Force-sensing microneedle for assisted retinal vein cannulation," *Proc. IEEE Sensors*, pp. 698–701, 2014.
- [77] J. M. Schmitt, S. H. Xiang, and K. M. Yung, "Speckle in Optical Coherence Tomography," *J. Biomed. Opt.*, vol. 4, no. 1, pp. 95–105, 1999.
- [78] M. Mahvash and P. E. Dupont, "Fast Needle Insertion to Minimize Tissue Deformation and Damage," in *IEEE International Conference on Robotics and Automation*, 2009, pp. 3097–3102.
- [79] M. Mahvash and P. E. Dupont, "Mechanics of Dynamic Needle Insertion into a Biological Material," *IEEE Trans. Biomed. Eng.*, vol. 57, no. 4, pp. 934–943, 2010.
- [80] A. G. Atkins, *Elastic and plastic fracture: metals, polymers, ceramics, composites, biological materials*, 1st edition. John Wiley & Sons Inc, 1988.
- [81] T. L. Anderson, *Fracture Mechanics: Fundamentals and Applications*, 3rd Edition. CRC Press, 2005.
- [82] J. R. Rice and G. F. Rosengren, "Plane strain deformation near a crack tip in a

- power-law hardening material,” *J. Mech. Phys. Solids*, vol. 16, no. 1, pp. 1–12, 1968.
- [83] D. S. Chauhan and J. Marshall, “The interpretation of optical coherence tomography images of the retina,” *Invest. Ophthalmol. Vis. Sci.*, vol. 40, no. 10, pp. 2332–2342, 1999.
- [84] A. F. Gmitro and A. R. Rouse, “Optical Biopsy with Confocal Microendoscopy,” *Opt. Photonics News*, vol. 20, no. 11, pp. 28–33, 2009.
- [85] B. A. Flusberg, A. Nimmerjahn, E. D. Cocker, E. A. Mukamel, R. P. J. Barretto, T. H. Ko, L. D. Burns, J. C. Jung, and M. J. Schnitzer, “High-speed, miniaturized fluorescence microscopy in freely moving mice,” *Nat. Methods*, vol. 5, no. 11, pp. 935–938, 2008.
- [86] K. L. Reichenbach and C. Xu, “Numerical analysis of light propagation in image fibers or coherent fiber bundles,” *Opt. Express*, vol. 15, no. 5, pp. 2151–2165, 2007.
- [87] J. Han and J. U. Kang, “Effect of multimodal coupling in imaging micro-endoscopic fiber bundle on optical coherence tomography,” *Appl. Phys. B*, vol. 106, no. 3, pp. 635–643, 2012.
- [88] B. L. Luck, K. D. Carlson, A. C. Bovik, and R. R. Richards-Kortum, “An image model and segmentation algorithm for reflectance confocal images of in vivo cervical tissue,” *IEEE Trans. Image Process.*, vol. 14, no. 9, pp. 1265–1276, 2005.
- [89] S. Rupp, C. Winter, and M. Elter, “Evaluation of spatial interpolation strategies for the removal of comb-structure in ber-optic images,” in *Proceedings of the 31st Annual International Conference of the IEEE Engineering in Medicine and*

*Biology Society*, 2009, pp. 3677–3680.

- [90] J.-H. Han, J. Lee, and J. U. Kang, “Pixelation effect removal from fiber bundle probe based optical coherence tomography imaging,” *Opt. Express*, vol. 18, no. 7, pp. 7427–7439, 2010.
- [91] C.-Y. Lee and J.-H. Han, “Elimination of honeycomb patterns in fiber bundle imaging by a superimposition method,” *Opt. Lett.*, vol. 38, no. 12, pp. 2023–2025, 2013.
- [92] M. Kyriash, R. Kester, R. R. Richards-Kortum, and T. S. Tkaczyk, “Improving spatial resolution of a fiber bundle optical biopsy system,” in *Proceedings of SPIE*, 2010, p. 755807.
- [93] N. Bedard and T. S. Tkaczyk, “Snapshot spectrally encoded fluorescence imaging through a fiber bundle,” *J. Biomed. Opt.*, vol. 17, no. 8, pp. 80508–1, 2012.
- [94] T. Vercauteren, A. Perchant, G. Malandain, X. Pennec, and N. Ayache, “Robust mosaicing with correction of motion distortions and tissue deformations for in vivo fibered microscopy,” *Med. Image Anal.*, vol. 10, no. 5, pp. 673–692, 2006.
- [95] Y. Choi, C. Yoon, M. Kim, W. Choi, and W. Choi, “Optical imaging with the use of a scattering lens,” *IEEE J. Sel. Top. Quantum Electron.*, vol. 20, no. 2, pp. 61–73, 2014.
- [96] W. Wang and F. Chang, “A multi-focus image fusion method based on Laplacian pyramid,” *J. Comput.*, vol. 6, no. 12, pp. 2559–2566, 2011.
- [97] S. S. Gurbani, P. Wilkening, M. Zhao, B. Gonenc, G. W. Cheon, I. I. Iordachita, W. Chien, R. H. Taylor, J. K. Niparko, and J. U. Kang, “Robot-assisted three-dimensional registration for cochlear implant surgery using a common-path swept-

- source optical coherence tomography probe,” *J. Biomed. Opt.*, vol. 19, no. 5, p. 57004, 2014.
- [98] X. Liu, Y. Huang, and J. U. Kang, “Dark-field illuminated reflectance fiber bundle endoscopic microscope,” *J. Biomed. Opt.*, vol. 16, no. 4, p. 46003, 2011.
- [99] D. C. Adler, T. H. Ko, and J. G. Fujimoto, “Speckle reduction in optical coherence tomography images by use of a spatially adaptive wavelet filter,” *Opt. Lett.*, vol. 29, no. 24, pp. 2878–2880, 2004.
- [100] F. Sattar, L. Floreby, G. Salomonsson, and B. Lovstrom, “Image enhancement based on a nonlinear multiscale method,” *IEEE Trans. image Process.*, vol. 6, no. 6, pp. 888–895, 1997.

## **CURRICULUM VITAE**

Gyeong Woo Cheon was born in Republic of Korea (South), March 15, 1982. He received his B.S. and M.S. degrees in Electrical and Computer Engineering and Biomedical Engineering from Seoul National University in 2008 and 2010, respectively. He enrolled in the Ph.D. program at the Johns Hopkins University, Baltimore, Maryland, in 2012. Since then, he worked under the guidance of Professor Dr. Jin U. Kang, in the Photonics and Optoelectronics group. His current research interests include depth guided handheld microsurgical tools based on common-path optical coherence tomography. He is a Korea Government-sponsored scholarship student and student member of SPIE, OSA, and IEEE.